

Kim Robert Gustavsen

Enhanced Electrochemical CO₂ Reduction through Nanostructuring and Light Element Modification

**Dissertation for the
degree of Ph.D**
Applied Micro- and
Nanosystems

Faculty of Technology, Natural
Sciences and Maritime
Sciences

Kim Robert Gustavsen

Enhanced Electrochemical CO₂ Reduction through Nanostructuring and Light Element Modification

A PhD dissertation in
Applied Micro- and Nanosystems

© Kim Robert Gustavsen, 2024

Faculty of Technology, Natural Sciences and Maritime Sciences
University of South-Eastern Norway
Horten

Doctoral dissertations at the University of South-Eastern Norway no. 184

ISSN: 2535-5244 (print)

ISSN: 2535-5252 (online)

ISBN: 978-82-7206-834-8 (print)

ISBN: 978-82-7206-835-5 (online)



This publication is licensed with a Creative Commons license. You may copy and redistribute the material in any medium or format. You must give appropriate credit, provide a link to the license, and indicate if changes were made. Complete license terms at <https://creativecommons.org/licenses/by-nc-sa/4.0/deed.en>

Print: University of South-Eastern Norway

Preface

This doctoral thesis is submitted in partial fulfilment of the requirements for the degree of Philosophiae Doctor (Ph.D.) at the Faculty of Technology, Natural Sciences and Maritime Sciences, University of South-Eastern Norway (USN), Norway.

The work was carried out between August 2018 and October 2023 at the Department of Microsystems under the supervision of Professor Kaiying Wang and Professor Erik Andrew Johannessen.

The work is financially supported by the project “Bioelectrochemistry - as an energy and environmental measure” (Bioelektrokjemi – som energi- og miljøtiltak) as part of the strategic research plan of University of South-Eastern Norway and by the Research Council of Norway through the Norwegian Micro- and Nano-Fabrication Facility (NorFab, No. 295864).

Acknowledgements

I would like to express my genuine appreciation to my supervisors Professor Kaiying Wang and Professor Erik Andrew Johannessen. Their guidance, insight and encouragement have played an important role in shaping my journey through doctoral research. I would also like to thank Ole Henrik Gusland, Zekija Ramic, Thomas Martinsen, Dr. Muhammad Tayyib, and Dr. Thai Anh Tuan Nguyen for making the experiments possible.

Equally important, I owe a debt of gratitude to my peers within the Department of Microsystems at USN. I must also reserve a special acknowledgment for Stephane Kuziora, Per Kristian Bolstad, Vegard Tollefsen, Dr. Chaoqun Cheng, Dr. Kang Du, Dr. Zengxing Zhang, and Dr. Hao Huang.

Special thanks to my family and friends, and my deepest appreciation to my better half, Hexin, for her strong support and encouragement throughout my Ph.D. journey.

Abstract

The rising levels of carbon dioxide (CO₂) in the atmosphere present a significant challenge to modern society due to its profound impact on the climate. It is therefore crucial to develop and employ carbon-neutral renewable energy technologies to diminish our reliance on fossil fuels. One of these technologies is the electrochemical reduction of CO₂. This approach can effectively address CO₂ emissions while serving as a potent energy storage method, especially when integrated with intermittent renewable energy sources, such as wind and solar power. One key aspect of this technique is the requirement of robust catalysts that provide high selectivity for a specific reaction product without compromising favorable reaction rates, and low overpotentials. This has remained a challenge due to the slow kinetics of the CO₂ reduction reaction under standard conditions and the concurrent hydrogen evolution reaction (HER), which competes with it.

There are two candidate materials, copper (Cu) and silver (Ag) that stand out as potential transition metal catalysts for electrochemical CO₂ reduction. Cu, in its pristine form, is distinctive in its ability to form hydrocarbons, while Ag exhibits impressive selectivity for carbon monoxide (CO) formation. Yet, Cu faces challenges with selectivity and stability, and Ag, despite its selectivity, demands high overpotentials and exhibits lower reaction rates in comparison to other CO forming catalysts, like gold (Au). Thus, the work presented in this thesis focus on design strategies that addresses these challenges through the development of processes that enables nanostructuring and incorporation of light elements into these two transition metals.

The first design was a two-step anodization process for Cu foils, which was developed for synthesis of homogenous copper hydroxide (Cu(OH)₂) nanoneedles over large areas (63 cm²) by utilizing a sodium persulfate pre-treatment step. The Cu(OH)₂ films displayed significant improvement in film uniformity with the inclusion of the pre-treatment step. For the electrochemical reduction of CO₂, the Cu(OH)₂ exhibited enhanced selectivity for ethylene (C₂H₄), with a near total suppression of methane (CH₄) formation. Furthermore, the Cu(OH)₂ catalyst displayed stable formation of C₂H₄ over 6

hours, whereas the Cu reference foil displayed a rapid decline in both C₂H₄ selectivity and current density.

A second design was the Ag-C composite thin films, that were synthesized via a co-deposition process involving both a carbon (C) and Ag sputtering target. The incorporation of C into the Ag films disrupted the growth kinetics, which led to a reduction in particle size and a significant enhancement in the films inherent surface area. As a catalyst, the Ag-C films exhibited superior current densities compared to pure Ag, due to the presence of a porous surface with an abundance of active sites and a heightened proficiency for HER as the C concentration increased. Moreover, by adjusting the C concentration, the H₂/CO ratio could be fine-tuned, making this catalyst design a promising prospect for syngas applications.

Finally, boron (B) was examined as a potential modifier for Ag catalysts in a study that combined both simulations and experiments. The results suggested that B enhanced the formation of CO by decreasing the activation barrier of *COOH formation while facilitating the rapid desorption of *CO from the Ag surface. A unique methodology was developed for the synthesis of the Ag-B catalysts, which showed that integrating B into Ag through a magnetron co-sputtering process led to the creation of highly textured Ag (111) films. These films exhibited a ~98% Faradaic efficiency (FE) for the electrochemical reduction of CO₂ to CO. The distinctive co-sputtering process enabled accurate control of the B content within the Ag films. Structural analysis revealed that the introduction of B into the crystal lattice of Ag initiated twin boundary growth and led to the formation of unique nano-tentacle structures. This significant improvement in catalytic activity was attributed to a combined contribution from the Ag (111) twin boundaries and the inclusion of B, which assisted in reducing the activation barrier for *COOH formation.

Keywords: Ag catalysts, CO₂RR, Cu catalysts, electrochemical CO₂ reduction, nanostructures, syngas

List of publications

Article 1

Gustavsen, K.R, and Wang, K. (2021). Recent Advances on Enhancing the Multicarbon Selectivity of Nanostructured Cu-based Catalysts. *Physical Chemistry Chemical Physics*, 38(4), 407-416. doi: 10.1080/02602938.2011.638738

Article 2

Gustavsen, K.R, Johannessen E.A, and Wang, K. (2022). Sodium Persulfate Pre-treatment of Copper Foils Enabling Homogenous Growth of Cu(OH)₂ Films for Electrochemical CO₂ Reduction. *ChemistryOpen*, 11(10), e202200133. doi: 10.1002/open.202200133

Article 3

Gustavsen, K.R, Johannessen E.A, and Wang, K. (2023). Carbon Modified Thin-film Catalysts for Electrochemical Reduction of CO₂ with Tunable H₂/CO Ratio. *Electrochemistry Communications*, 155, 107582. doi: 10.1016/j.elecom.2023.107582.

Article 4

Gustavsen, K.R, Hao, H, Johannessen E.A, and Wang, K. (2023). Boron-induced growth of highly textured Ag (111) films with nano-tentacle structures for the electrochemical reduction of CO₂ to CO. *Electrochemistry Communications*, 156, 107600. doi: 10.1016/j.elecom.2023.107600.

Patent 1

Gustavsen, K.R, Wang, K. (2022). Process for producing single crystal films. Norwegian Industrial Property Office, Pat. No. 347559.

Patent 2

Gustavsen, K.R, Wang, K. (2022). Process for producing single crystal films. The Patent Cooperation Treaty (PCT) [Submitted 16.06.23]

Papers not enclosed in the thesis

Article 5

Zhang, Z. Wang, Y. Stensby Hansen, P. A. Du, K. Gustavsen, K. R. Liu, G. Karlsen, F. Nilsen, O. Xue, C. and Wang, K. (2019). Black silicon with order-disordered structures for enhanced light trapping and photothermal conversion. *Nano Energy* 65, 103992, doi: 10.1016/j.nanoen.2019.103992.

Article 6

Cheng, C. Gustavsen, K. R. and Wang, K. (2021) Plasmon-induced visible light absorption arising from edge-interfaces of titanium-oxides nanocomposites. *Optical Materials*, 113, 110847, doi: 10.1016/j.optmat.2021.110847.

Article 7

Gustavsen, K. R. Feng, T. Huang, H. Li, G. Narkiewicz, U. and Wang, K. (2023) DFT calculation of carbon doped TiO₂ nanocomposites. *Materials*, 16, 6117. doi: 10.3390/ma16186117

List of figures

Figure 1-1 Working principle of electrochemical CO ₂ reduction.	3
Figure 1-2 Possible reaction pathways for C1-products with colors representing the reaction pathways suggesting by different research groups.....	7
Figure 1-3 Possible reaction pathways for the formation of C ₂ H ₄ and C ₂ H ₅ OH	9
Figure 1-4 Mechanisms for the transfer of CO from Ag to Cu sites.....	11
Figure 1-5 Oppositely charged *CO at oxidized Cu and metallic Cu sites	12
Figure 1-6 Different Ag nanostructures, a) nanowires, b) nanocorals, c) dendrites, and d) triangular nanoplates	14
Figure 1-7 Intermediate binding energy as a function of the d-band center using a) d-block dopants and b) p-block dopants in Ag.....	16
Figure 1-8 a) single-element and b) composite catalyst design for adjustable H ₂ /CO ratio from CO ₂ RR.....	18
Figure 2-1 The H-cell used for the electrochemical reduction experiments.	22
Figure 2-2 Schematic showing the reactor setup used for the electrochemical CO ₂ reduction and gas quantification.	22
Figure 2-3 A typical GC spectrum obtained with the optimized GC program.	25
Figure 2-4 GC Calibration curve for H ₂ with concentration in parts per million as a function of peak area.	27
Figure 3-1 Process flow showing the development of the Cu(OH) ₂ nanoneedle films ..	30
Figure 3-2 SEM images of the a) pristine Cu foil, b)-c) pinhole and patch with reduced growth found on the anodized Cu foil. SEM images of the d) Cu foil after pre-treatment with sodium persulfate, e)-f) the surface morphology of the pre-treated Cu foil after anodization.....	31
Figure 3-3 Electrochemical characterization: a) selectivity of the Cu foil catalyst, b) selectivity of the Cu(OH) ₂ catalyst, c) stability test, and d) C ₂ H ₄ to CH ₄ ratio and C ₂ H ₄ partial current density obtained for the Cu(OH) ₂ catalyst during the stability test.	33
Figure 3-4 SEM image of the a) Ag, b) Ag-C-1, and c) Ag-C-2 films. d) XRD patterns of the Ag and Ag-C films with the EDX spectrum obtained for the Ag-C-2 film inset	36

Figure 3-5 Electrochemical characterization of the Ag-C catalysts. a) LSV of the Ag and Ag-C catalysts, b) their product selectivity as a function of potential, c) the ratio of H₂/CO for the Ag-C catalysts, the Tafel slope for d) CO and e) HER 37

Figure 3-6 Schematic showing the co-sputtering arrangement used for growing the Ag-B films..... 40

Figure 3-7 Band structure of the a) Ag-B (111) and b) Ag (111) slabs. c) comparison of the d-bands of the two slabs, showing the change in d-band center. d) free energy diagram for CO₂ reduction over the two surfaces..... 41

Figure 3-8 a) XRD spectra of the Ag and Ag-B films and b) zoomed in plot showing the Ag (111) peak 42

Figure 3-9 TEM images of the Ag-B-2 film. a) STEM, b) HRTEM with SAED (inset), c)-e) HRTEM of the coherent twin boundaries 43

Figure 3-10 SEM images of the a) Ag, b) Ag-B-1, c) and Ag-B-2..... 44

Figure 3-11 XPS measurements showing the B 1s peak for the a) Ag-B-1 and b) Ag-B-2 films..... 45

Figure 3-12 a) Faradaic efficiencies obtained for the catalysts as a function of applied potential and b) the partial current density of CO 46

Figure 3-13 Stability test conducted for the Ag-B-2 catalyst, showing the current density and FE(CO) as a function of time 47

Figure 3-14 a) the twin boundary structure used in the simulations, b) the free energy diagram, and c) reaction geometries..... 48

Abbreviations

AES	Auger electron spectroscopy
AFM	Atomic force microscope
BID	Barrier-ionization detector
CO ₂ RR	CO ₂ reduction reaction
CAER	Covalency-aided electrochemical reaction
DC	Direct current
DFT	Density functional theory
ECSA	Electrochemical active surface area
EDX	Energy dispersive x-ray spectroscopy
FE	Faradaic efficiency
FE-SEM	Field-emission scanning electron microscope
FTIR	Fourier-transform infrared spectroscopy
GC	Gas chromatography
GDE	Gas diffusion electrode
GDL	Gas diffusion layer
HER	Hydrogen evolution reaction
HRTEM	High-resolution transmission electron microscope
LSV	Linear scan voltammetry
OD-Cu	Oxygen-derived Copper
PEM	Proton-exchange membrane
RDS	Rate determining step
RF	Radio frequency
RHE	Reversible hydrogen electrode
SAED	Selected area electron diffraction
SCCM	standard cubic centimetre per minute
SDI	Selectivity-determining intermediate
SEM	Scanning electron microscope
SFE	Stacking fault energy
SHE	Standard hydrogen electrode

STEM	Scanning transmission electron microscope
TEM	transmission electron microscope
XPS	X-ray photoelectron spectroscopy
XRD	X-ray diffraction

Table of contents

Preface	I
Acknowledgements	III
Abstract	V
List of publications	VII
List of figures	IX
Abbreviations	XI
1 Introduction	1
1.1 Background and motivation.....	1
1.2 Electrochemical CO ₂ Reduction	2
1.2.1 Working principle.....	2
1.2.2 Reaction products	3
1.2.3 Transition metal catalysts	4
1.3 Reaction mechanisms and pathways.....	5
1.4 Cu-based catalysts.....	10
1.4.1 Strategies for enhancing the selectivity of Cu	10
1.5 Ag-based catalysts.....	13
1.5.1 Strategies for enhancing the formation of CO.....	13
1.5.2 Promoting syngas formation.....	17
1.6 Research focus and objectives.....	19
2 Experimental Setup	21
2.1 Reactor configuration	21
2.2 Electrochemical test conditions.....	22
2.3 Quantification of gaseous reaction products	23
2.3.1 GC calibration and measurement parameters	23
2.3.2 Calculating the Faradaic efficiency	27
3 Summary of Main Research	29
3.1 Copper hydroxide nanoneedles (Article 2).....	29
3.2 C-modified Ag Catalysts (Article 3)	34
3.3 Ag-B Catalysts (Article 4).....	39

4 Conclusions and Outlook.....	49
References.....	55
Article 1	61
Article 2	81
Article 3	89
Article 4	97
Patent.....	107

1 Introduction

1.1 Background and motivation

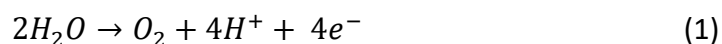
The climate change brought on by the ever-increasing CO₂ concentrations in the atmosphere persists as one of the biggest threats to modern society, and an urgent response is needed to address both the CO₂ emissions and the increasing demands for energy. Thus, transition from fossil fuel-based energy to renewable energy sources is therefore necessary to ensure a sustainable future. This is not without challenges though since traditional renewable energy sources based on wind and solar suffer from fluctuating power outputs dependent on the weather and climate conditions. On top of that, both wind and solar energy generation is problematic due to the severe mismatch between the instant energy supply and demand. Energy storage acting as a buffer is therefore necessary to fully utilize these types of renewable energy sources. While solid state batteries have come a long way, they are severely limited in terms of energy storage capacity (power density) required for these types of processes. Thus, new energy storage technologies that allow for efficient transportation and use are required. One such technology is the electrochemical reduction of CO₂ into hydrocarbon fuels or other commodity chemicals. The reduction of CO₂ into fuels is attractive since it can directly tackle CO₂ emissions while simultaneously providing a way to store and transport energy generated by renewable energy sources. While the CO₂ reduction reaction (CO₂RR) has been extensively studied, it is still considered as being in its infancy in terms of industrial applications. One of the major reasons are the drawbacks of the catalyst material used, which suffers from stability issues and poor selectivity for the desired reaction product due to the competitive hydrogen evolution reaction (HER). Therefore, the development of catalysts that are selective and able to operate over prolonged periods of time is of utmost importance. Since the CO₂RR is versatile in terms of the reaction product being generated, the strategies employed for engineering the catalyst depend on both the catalyst material and the reaction product being targeted. This chapter will give an overview of the CO₂RR, the possible reaction products obtained by different transition metals, and a summary of the available strategies for enhancing

the catalytic properties of Cu and Ag, which are the transition metals used for CO₂RR in the work described in this thesis.

1.2 Electrochemical CO₂ Reduction

1.2.1 Working principle

The CO₂ molecule constitute the fully oxidized form of C and is therefore highly stable. Any attempts in reducing it is therefore a highly unfavorable process, with the one electron reduction taking place at a thermodynamic potential of -1.9 V vs. the standard hydrogen electrode (SHE) [1]. A catalyst is therefore needed to facilitate the reaction by lowering the activation barrier. The electrochemical CO₂ reduction commonly takes place in an H-cell, which consists of an anodic and cathodic compartment that are separated by a membrane, typically a proton exchange membrane (PEM). Other cell designs exist such as the flow-cell, but we will focus on the H-cell, which can be seen in figure 1-1. When a voltage is applied across the half-cells the oxidation of water occurs at the anode to form oxygen gas, protons, and electrons according to the reaction in equation 1:



At the cathode, CO₂ combines with the electrons provided by the current and the protons (H⁺) migrating through the membrane to form reduced products.

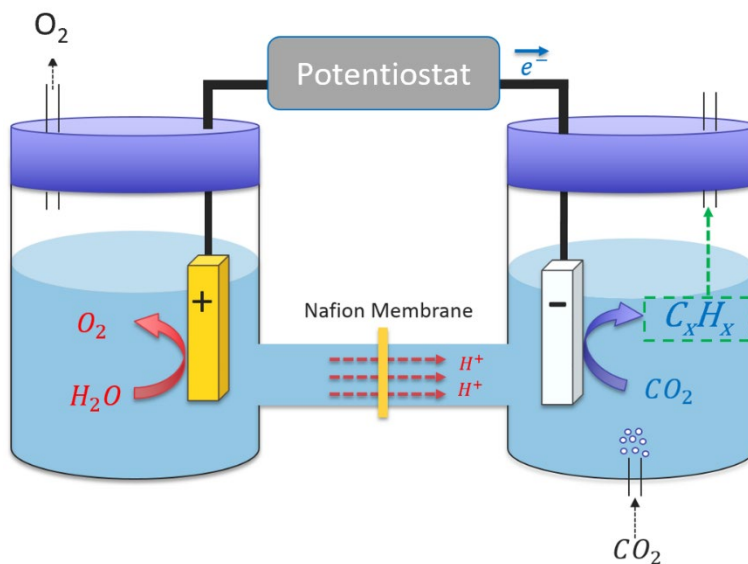


Figure 1-1 Working principle of electrochemical CO₂ reduction.

1.2.2 Reaction products

Compared to water splitting, the reduction of CO₂ is highly complex due to the sheer amount of reaction intermediates and reaction products involved. The reaction products can be divided into two categories: the one-carbon products (C1) and the multicarbon products (C2+). The C1 products include carbon monoxide (CO), formate/formic acid (HCOO⁻/HCOOH), methane (CH₄), and methanol (CH₃OH) whereas the C2 products consist of ethylene (C₂H₄), ethanol (C₂H₅OH), ethane (C₂H₆), etc. Most of the commonly encountered reaction products, their half reactions, and their theoretical reduction potential vs. the reversible hydrogen electrode (RHE) at neutral pH can be seen in table 1. The main distinction is that the C2 reaction products require a coupling of two surface bound CO (*CO), referred to as a CO-CO coupling or CO dimerization. The type of reaction product being formed depends almost entirely on the catalyst being used.

Table 1-1 Electrochemical CO₂ reduction reactions with equilibrium potentials [2].

Half reactions	E ⁰ (V) vs. RHE at pH 7
$\text{CO}_2 + \text{e}^- \rightarrow \text{CO}_2^-$	-1.48
$\text{CO}_2 + 2\text{H}^+ + 2\text{e}^- \rightarrow \text{HCOOH}(\text{l})$	-0.12
$\text{CO}_2 + 2\text{H}^+ + 2\text{e}^- \rightarrow \text{CO}(\text{g}) + \text{H}_2\text{O}$	-0.10
$\text{CO}_2 + 6\text{H}^+ + 6\text{e}^- \rightarrow \text{CH}_3\text{OH}(\text{l}) + \text{H}_2\text{O}$	0.03
$\text{CO}_2 + 8\text{H}^+ + 8\text{e}^- \rightarrow \text{CH}_4(\text{g}) + 2\text{H}_2\text{O}$	0.17
$2\text{CO}_2 + 12\text{H}^+ + 12\text{e}^- \rightarrow \text{C}_2\text{H}_4(\text{g}) + 4\text{H}_2\text{O}$	0.08
$2\text{CO}_2 + 14\text{H}^+ + 14\text{e}^- \rightarrow \text{C}_2\text{H}_5\text{OH}(\text{l}) + 3\text{H}_2\text{O}$	0.09
$2\text{CO}_2 + 14\text{H}^+ + 14\text{e}^- \rightarrow \text{C}_2\text{H}_6(\text{g}) + 4\text{H}_2\text{O}$	0.14
$3\text{CO}_2 + 18\text{H}^+ + 18\text{e}^- \rightarrow \text{C}_3\text{H}_7\text{OH}(\text{l}) + 5\text{H}_2\text{O}$	0.10

1.2.3 Transition metal catalysts

Based on the pioneering work of Hori et. al [3], the transition metals can be divided into groups depending on their product selectivity as seen in table 2. There is the HCOO⁻ group, the CO group, and the transition metals that do not noticeably reduce CO₂ but are more selective towards the HER. Note that Cu does not belong to any of the groups due to its unique capability of producing hydrocarbons and C2 products, which does not occur for any other transition metals. The tendency to favor one reaction product over another is associated with the binding energies of the CO₂ molecule and the subsequent reaction intermediates to the transition metal surface. For instance, in the case of the CO producing metals, the *CO binding strength is low, thus favoring desorption rather than further reduction. On the other side of the spectrum, the HER selective metals exhibit very high binding energies for CO, leading to CO poisoning (inactivation of binding sites that stops any further reduction of C) and therefore preference for H₂ formation. As for Cu, the binding energy is at a midway point between the two, which is optimal for further reduction beyond CO, including C2 products through C-C coupling.

Table 1-2 Faradaic efficiencies of reaction products attained for metal electrodes in 0.1 M KHCO₃ at 18.5 ± 0.5°C. Reprinted with permission from ref [3].

Electrode	Potential vs. SHE (V)	Current density (mA cm ⁻²)	Faradaic efficiency (%)							
			CH ₄	C ₂ H ₄	EtOH ^a	PrOH ^b	CO	HCOO ⁻	H ₂	Total
Pb	-1.63	5.0	0.0	0.0	0.0	0.0	0.0	97.4	5.0	102.4
Hg	-1.51	0.5	0.0	0.0	0.0	0.0	0.0	99.5	0.0	99.5
Tl	-1.60	5.0	0.0	0.0	0.0	0.0	0.0	95.1	6.2	101.3
In	-1.55	5.0	0.0	0.0	0.0	0.0	2.1	94.9	3.3	100.3
Sn	-1.48	5.0	0.0	0.0	0.0	0.0	7.1	88.4	4.6	100.1
Cd	-1.63	5.0	1.3	0.0	0.0	0.0	13.9	78.4	9.4	103.0
Bi ^c	-1.56	5.0	1.2	-	-	-	-	77	-	-
Au	-1.14	5.0	0.0	0.0	0.0	0.0	87.1	0.7	10.2	90.0
Ag	-1.37	5.0	0.0	0.0	0.0	0.0	81.5	0.8	12.4	94.6
Zn	-1.54	5.0	0.0	0.0	0.0	0.0	79.4	6.1	9.9	95.4
Pd	-1.20	5.0	2.9	0.0	0.0	0.0	28.3	2.8	26.2	60.2
Ga	-1.24	5.0	0.0	0.0	0.0	0.0	23.2	0.0	79.0	102.0
Cu	-1.44	5.0	33.3	25.5	5.7	3.0	1.3	9.4	20.5	103.5 ^d
Ni	-1.48	5.0	1.8	0.1	0.0	0.0	0.0	1.4	88.9	92.4 ^e
Fe	-0.91	5.0	0.0	0.0	0.0	0.0	0.0	0.0	94.8	94.8
Pt	-1.07	5.0	0.0	0.0	0.0	0.0	0.0	0.1	95.7	95.8
Ti	-1.60	5.0	0.0	0.0	0.0	0.0	tr.	0.0	99.7	99.7

^aethanol; ^bn-propanol; ^cfrom ref [4]; ^dthe total amount also includes C₃H₄OH(1.4%), CH₃CHO(1.1%), C₂H₅CHO(2.3%); ^ethe total amount includes C₂H₆(0.2%)

1.3 Reaction mechanisms and pathways

A substantial amount of research has been aimed at understanding the reaction mechanisms and the various reaction pathways through a combination of density functional theory (DFT) simulations and experimental in-situ detection of intermediates. While the reaction pathways for the C1 products are more established, the reaction pathways for the C2 products are vastly more complex. The general outline of the C1 reaction pathways can be seen in figure 1-2, although small differences could exist between the various transition metals. In the first step, the CO₂ molecule is physisorbed to the surface, before forming chemisorbed *CO₂. HCOO⁻ is formed by a direct reaction of physisorbed CO₂ with *H [5], or by protonation of *CO₂ to form the *OCHO

intermediate [6]. Experimentally formate/formic acid has been proven to not reduce any further, with no reaction products being detected when introducing formate/formic acid to the electrolyte [7, 8]. As for CO, a proton/electron transfer first facilitates the formation of *COOH from *CO₂⁻, which upon being subjected to a secondary proton/electron transfer leads to the formation of *CO that ultimately desorbs from the surface to form CO [5]. This is the common pathway identified for all the CO selective metals (Zn, Ag, Au). There are still some debates surrounding the reaction pathways for methane, but it is generally accepted that it forms through the protonation of the *CHO/*COH intermediate [9].

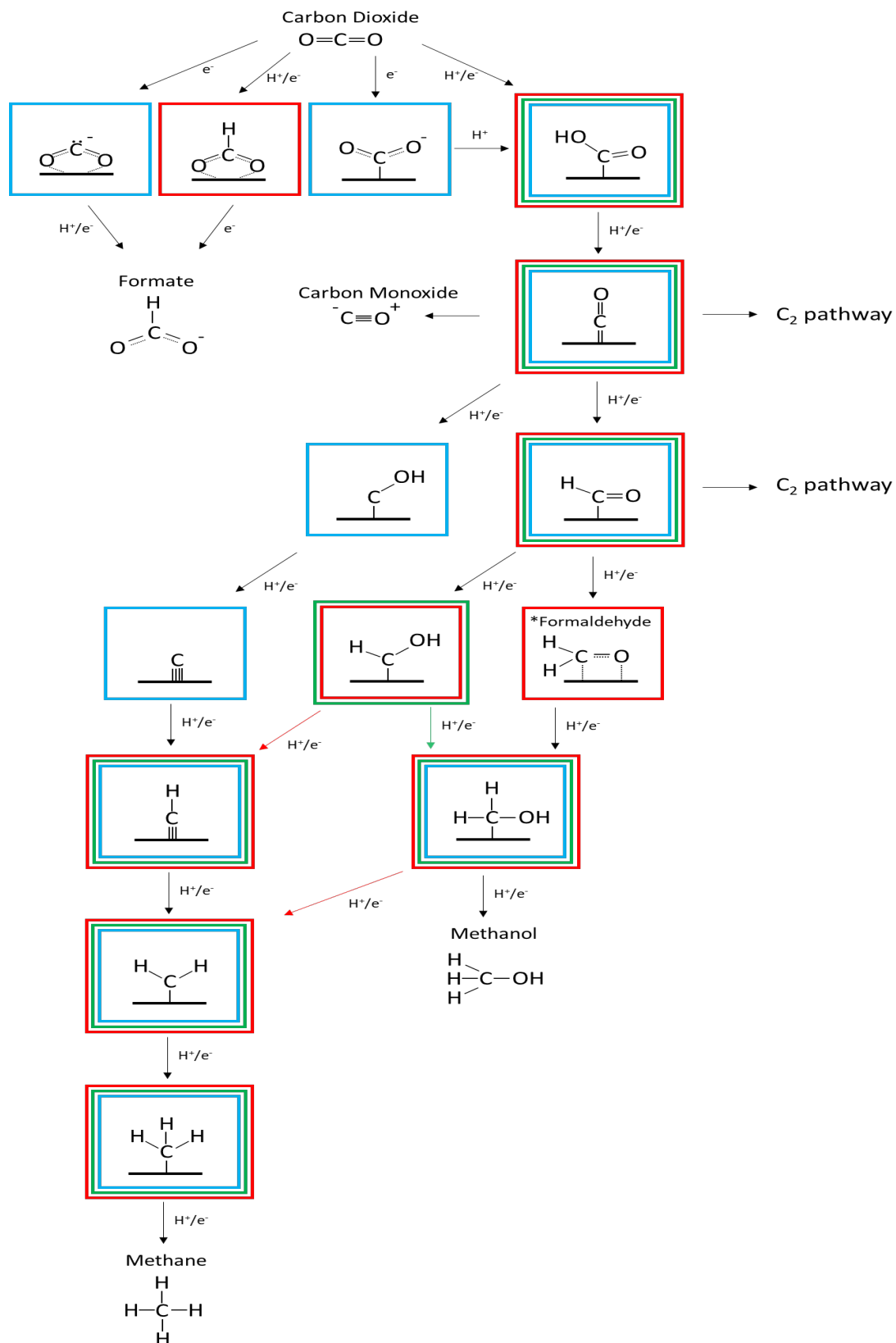


Figure 1-2 Possible reaction pathways for C1-products with colors representing the reaction pathways suggesting by different research groups. Reproduced from ref [10] with permission from the PCCP Owner Societies.

As for the C₂ reaction product pathways, they exist primarily for Cu-based catalysts, with the C₁ and C₂ reaction pathways separating at the *CO and *CHO intermediates. The C₂ products form either by a coupling of *CHO/*COH with *CO to form *COCHO/*COCOH or by dimerization of *CO to first form the *COCO intermediate which undergoes a subsequent protonation to form *COCHO/*COCOH [11]. Ethylene and ethanol are the two most common C₂ reaction products obtained from the CO₂RR, and their reaction pathways are depicted in figure 1-3. It is important to determine the selectivity determining intermediate (SDI) for these two reactions to further tune the selectivity towards either ethylene or ethanol after high yields of C₂ products have been attained. According to figure 1-3 *COCHO, *CHCOH, *CH₂CHO, CH₂CH₂O*, and *CH₃CH₂O have all been suggested as the SDI. In general, it is more favorable from a catalyst engineering point of view for the reaction pathways to separate as early as possible as it becomes easier to selectively stabilize/destabilize a given intermediate. For instance, *COCHO as the SDI would be an optimal scenario as it would involve less intermediates before separation of the ethylene and ethanol pathway. In this case the *COCHO intermediate is suggested to form glyoxal that can be chemisorbed to the catalyst surface before undergoing further reduction to ethanol and acetaldehyde. In fact, a study have confirmed the presence of glyoxal [12], and electrochemical reduction of glyoxal has been proven to convert to ethanol with small amounts of acetaldehyde [13, 14]. For the formation of ethylene, *COCHO undergoes protonation to form the *COCHOH intermediate. As is evident from figure 1-3, no clear consensus exists for the reaction pathways for these products. Most of these suggested pathways are also based solely on computational chemistry using ideal single crystal surfaces, which means that the pathways are not necessarily valid for different crystal facets or polycrystalline surfaces. For instance, the CO-CO coupling pathway to form the *COCO intermediate exists exclusively for the Cu (100) surface [15], whereas the formation of *CHO/*COH is favorable over Cu (111).

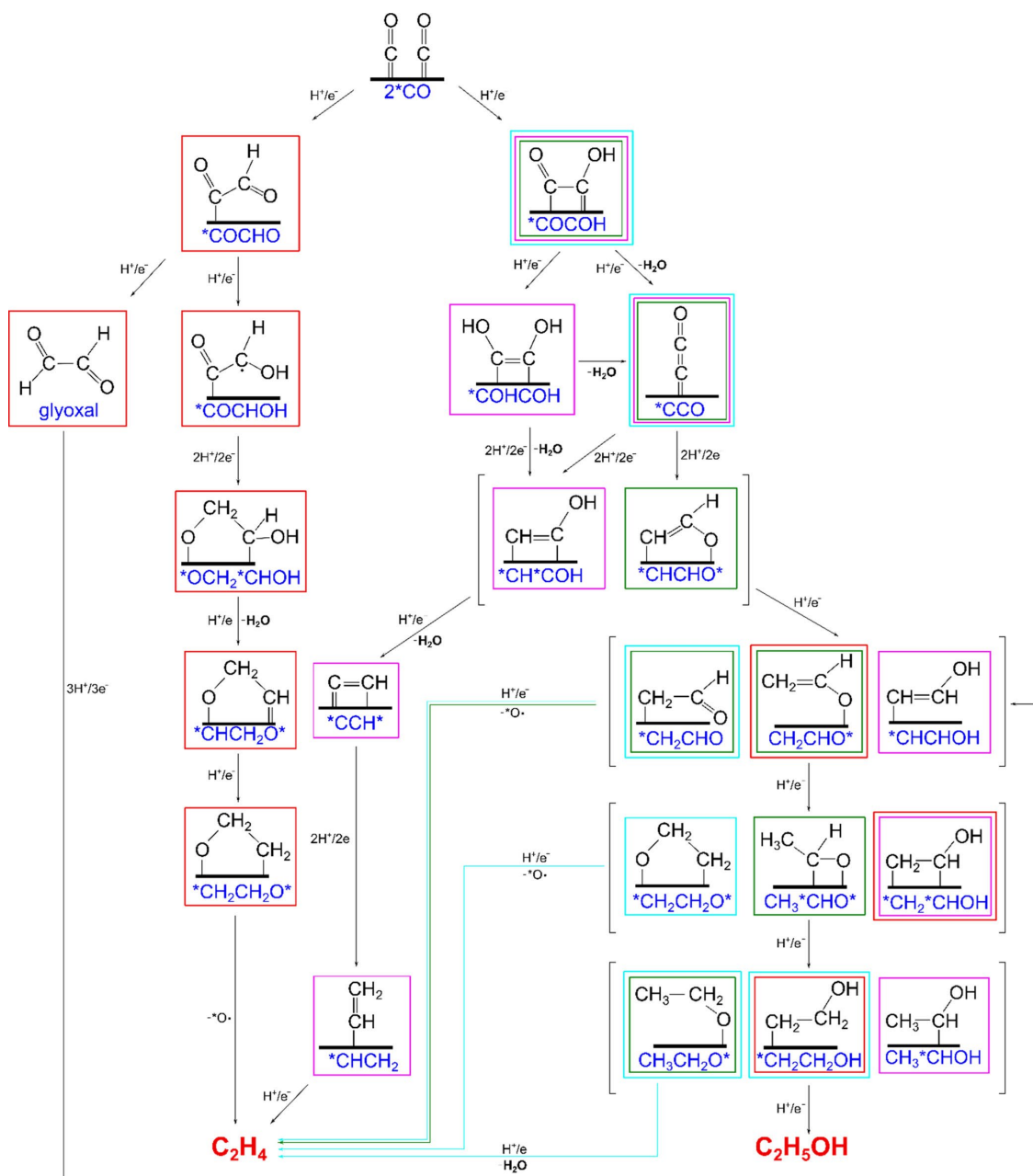


Figure 1-3 Possible reaction pathways for the formation of C₂H₄ and C₂H₅OH. The brackets surround the different tautomers of a given intermediate and the colors represent the reaction pathway suggested by different research groups as follows: Bell and Head-Gordon (red) [16], Goddard et al. (pink) [17, 18], Janik and Asthagiri (blue) [19], and Calle-Vallejo and Koper (green) [20, 21]. Reprinted with permission from ref [22] Copyright 2020 American Chemical Society.

1.4 Cu-based catalysts

In the CO₂RR Cu appears as an ideal candidate due to its abundance and its ability to form hydrocarbons. Unfortunately, Cu suffers from some severe limitations that needs to be overcome. As mentioned previously, Cu catalysts are unique in that they can produce hydrocarbons, being the only metal capable of facilitating the C-C coupling in its pristine form. Unfortunately, Cu produces a wide range of reaction products simultaneously, which means the selectivity is poor since high faradaic efficiency (FE) cannot be obtained for a single product. In addition, Cu is inherently unstable and tends to deactivate under reaction conditions. Thus, the selectivity of Cu needs to be tuned so that it favors the formation of one reaction product, and the stability needs to be improved. The reaction mechanisms over Cu catalysts are highly complex due to the number of intermediates and reaction pathways involved in the reaction as highlighted in the previous section. However, in-situ measurements and the development of computational chemistry have aided in the understanding of the reaction steps at Cu catalysts. Understanding the reaction mechanisms over Cu has been fundamental in developing facile strategies for improving its catalytic performance.

1.4.1 Strategies for enhancing the selectivity of Cu

Cu is perhaps the most studied catalyst for CO₂ reduction, and a plethora of strategies for steering the selectivity and increasing the stability of Cu-based catalysts has been developed. Most of these strategies are focused on steering the selectivity of Cu towards the C₂ reaction products, and primarily ethylene and ethanol. These strategies involve morphology and crystal facet engineering, incorporations of other metals, and oxidation. A brief introduction of the available methods and their impact on the catalytic activity is given below.

1.4.1.1 Facet engineering

It is well known that the various crystal facets of the transition metals exhibit differences in reactivity. For instance, Cu favors the formation of C₂H₄ at the (100) facet, while preferring CH₄ at the (111) facet [23]. This occurs due to existence of an additional

pathway for ethylene formation at low overpotentials that involves the dimerization of CO [15]. Thus, it allows for the formation of C₂H₄ through the *CO intermediate as opposed to *CHO, which is a shared intermediate of C₂H₄ and CH₄. Therefore, Cu (100) exhibits a higher selectivity for C₂H₄ at lower potentials than Cu (111), but the difference is negligible at sufficiently high overpotentials since the CHO pathway becomes available at Cu (100). Hence, finding ways to synthesize structures that expose as much of the (100) facet as possible can contribute towards enhancing the C₂H₄ selectivity. One such example is nanocubes, which consists of four large-area Cu (100) facets with (110) edges. It has been shown that the synergetic behavior of these two sites can further enhances the CO-CO coupling [24, 25]. Meaning that the size of these nanocubes also play an important role in formation of C₂H₄ [26].

1.4.1.2 Metal co-catalysts

Cu can be combined with other metals to enhance the C₂ product formation, predominately by utilizing CO producing metals like Ag, Au, and Zn. The concept utilizes the metal co-catalyst as a CO feedstock for the adjacent Cu sites, which enables further reduction into C₂ products by either surface diffusion or re-adsorption of the *CO to the Cu sites as illustrated in figure 1-4 [27, 28]. Note that this strategy requires the existence of two segregated metal phases since the formation of an alloy would change the overall reaction mechanisms.

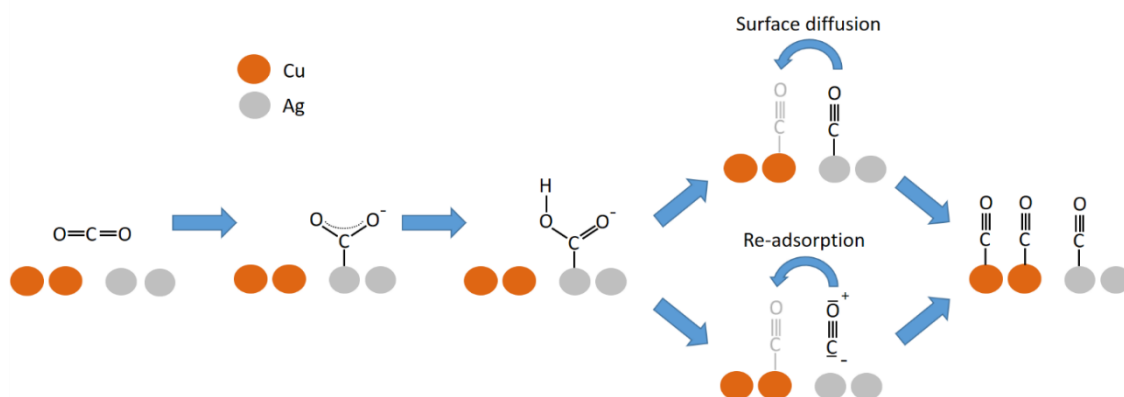


Figure 1-4 Mechanisms for the transfer of CO from Ag to Cu sites. Reproduced from ref [10] with permission from the PCCP Owner Societies.

1.4.1.3 Oxide-derived Cu

The oxide-derived Cu (OD-Cu) catalysts are simultaneously the most successful at promoting C₂ product formation and the most controversial due to the dispute within the research community of the underlying cause for the improved performance. In short, the OD-Cu consists of an oxidized Cu surface, which upon reduction exhibits significantly improved selectivity towards C₂ products [29, 30]. Furthermore, the method used for oxidation and the subsequent reduction process of the oxide also affects the overall product selectivity. As for the mechanism responsible for the change in selectivity, numerous theoretical and experimental studies have attempted to explain the phenomenon. The debate is usually centered around whether any oxides can survive during the reaction conditions, since the electrochemical reduction of CO₂ into C₂ products occur at a potential way beyond that of the reduction of the Cu oxide. However, there are claims that a small amount of sub-surface oxide can be present during reaction conditions and thereby impact the reaction mechanics [31, 32]. While DFT studies have shown that the Cu oxides themselves are detrimental to the overall CO₂ reduction reaction, the combined existence of Cu⁺ and metallic Cu⁰ sites can enhance the CO-CO coupling due to opposite charges being imposed onto the carbon atom of *CO (figure 1-5) [33]. Proving the existence of sub-surface oxide experimentally is extremely difficult since any exposure to ambient air following the CO₂RR will lead to oxidation of the Cu surface. Therefore, in-situ measurements are necessary for analyzing the chemical composition of the Cu catalyst surface post-reduction, which is challenging from a practical point of view.

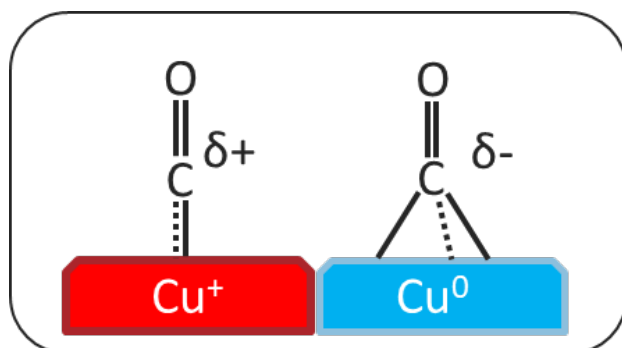


Figure 1-5 Oppositely charged *CO at oxidized Cu and metallic Cu sites.

1.4.1.4 *Alternative oxidizers*

Based on the increase in performance observed for the OD-Cu catalysts, a new set of catalysts were developed that could create stable Cu⁺ sites that did not deteriorate during the reaction conditions. A prime example is the B-doped Cu catalyst, which achieved a 52% FE for C₂H₄ (FE(C₂) of 79%) and remained stable for the whole duration of the 40-hour stability test [34]. On the other hand, the reference Cu and OD-Cu deactivated after 6 and 12 hours, respectively. Theoretical calculations suggested that the average oxidation state of the Cu surface could be tuned by varying the B concentration, where an optimal FE of C₂ products was obtained at an average oxidation state of 0.35. Enhancement in C₂ product formation has also been achieved for other p-block dopants such as sulfur and the halogen group [35, 36].

1.5 Ag-based catalysts

While significant effort has been dedicated to tuning the selectivity of Cu towards multicarbon products, there is also an incentive to optimize the transition metals capable of achieving high FE for C₁ products. The electrochemical reduction of CO₂ to CO is currently much more viable for scale-up due to being a one electron process, where high faradaic efficiencies (~90%) can be achieved. On top of that, CO can be utilized as a feedstock for the Fischer-Tropsch process to produce hydrocarbons, which makes it an attractive reaction product. Ag together with Au belongs to the group of transition metals that produce CO. FE of up to 90% can be obtained for both these metals, but the overpotentials required to reach this FE(CO) for Ag is considerably higher than for Au. Additionally, Ag is significantly cheaper than Au, and is therefore a more viable alternative for large scale reactors. Thus, reducing the overpotential of Ag is necessary to make the catalyst feasible.

1.5.1 Strategies for enhancing the formation of CO

The overpotential for CO formation of Ag is governed by the binding energy of the *COOH intermediate. Au exhibits a stronger affinity for *C bound species, which allows for stronger *COOH binding and thus a lower activation barrier. Research has therefore

focused on developing strategies for increasing the binding affinity of *COOH at the Ag surface. The most common approaches for improving the catalytic performance of Ag are highlighted below.

1.5.1.1 Nanostructuring

Like Cu, the catalytic activity of Ag is highly dependent on the crystal facet at which the reaction occurs. The difference between the catalytic performance of the Ag crystal facets were discovered early on by Hori et.al [37]. Compared to Ag (100) and Ag (111) the stepped sites of the Ag (110) display significantly enhanced performance with five times larger partial current density for CO. This is mainly due to the increased binding strength of the *COOH intermediate on the Ag (110) surface [38]. Nanostructures have been frequently utilized to expose these preferential active sites. Furthermore, the size of these nanostructures can be adjusted to achieve an optimal ratio of the atoms at the edge, corner, or surface, which allows for tuning the binding energy of the *COOH intermediate [38-42]. A range of nanostructures has been developed for this purpose (figure 1-6), such as nanowires [43], nanocorals [44], dendrites [45], triangular nanoplates [46], and nanocubes [47].

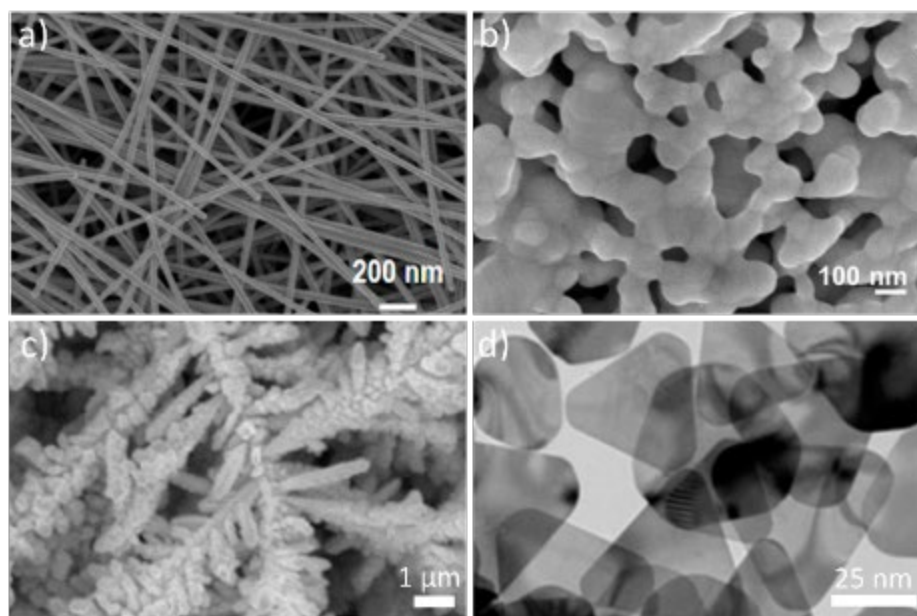


Figure 1-6 Different Ag nanostructures, a) nanowires, b) nanocorals, c) dendrites, and d) triangular nanoplates. Adapted with permission from a) ref [43] Copyright 2018 American Chemical Society, b) ref [44] Copyright 2015 American Chemical Society, c) ref [45], and d) ref [46] Copyright 2017 American Chemical Society.

1.5.1.2 Metal co-catalyst and alloys

There are two main approaches to selecting an appropriate metal as a co-catalyst or for alloy: (i) reducing the amount of Ag through alloying with a different element to reduce the cost, but without compromising the efficiency of the catalyst; or (ii) improve the efficiency by suppressing the competing HER. In the first category it is primarily Cu, Zn, and Sn that are used. It has been found that Ag₈₄Cu₁₆ displays 2.5 times the FE(CO) compared to the pristine Ag₁₀₀ reference electrode at lower potentials. If the amount of Cu is increased further, the FE(CO) unfortunately declines [48]. Although Zn exhibits high selectivity towards CO (like Ag), it suffers from even larger overpotentials and the FE(CO) is negatively impacted when Ag is alloyed with Zn, making it a less attractive option [49]. This is also the case for Sn, where the pristine Ag outperforms the AgSn catalyst [50], except from some cases where AgZn foils have shown the capability to break the scaling relations to enable the formation of methane and methanol due to the stabilization of the *CHO intermediate [49]. In contrast, HER by inhibition is pursued by incorporating metals that are known to exhibit low catalytic activity for that reaction. For instance, indium (In) is a prime candidate since it possesses a high overpotential for HER. Therefore, the introduction of In in Ag leads to a suppression of the HER, which allows for high FE(CO) at lower overpotentials [51].

1.5.1.3 Doping with p-block elements

Another potent strategy that enables lower overpotentials and higher reactivity of the Ag catalyst is based on the modulation of the Ag d-band through introduction of defects or impurities. The d-band theory has its foundation in molecular orbital theory, where the interaction of the catalyst with a molecule is governed by the formation of the bonding and anti-bonding orbitals. Since Ag has a full d-shell, the antibonding states are always filled, and thus shifting the d-band center towards the fermi-level can reduce the filling of the anti-bonding states, which gives a stronger chemisorption of intermediates. However, there is a theoretical limit to the reduction in overpotential that can be achieved using this method due to the linear scaling relations. Since the increased reactivity of the Ag imposed by the shift in the d-band center does not discriminate

between the *COOH and *CO intermediates, the binding of *CO also becomes stronger, which eventually will make it incapable of desorption. Not to mention that the binding strength of *H also becomes enhanced, which can enhance the HER. The utilization of p-block dopants has recently emerged as a viable route for circumventing the linear scaling relation between the d-band and the binding energies of the *COOH and *CO intermediates. It has been found that a partial covalency can be imposed on Ag by the p-block element to allow for it to interact with the *COOH and *CO by two independent mechanisms. More precisely, dissimilar σ -binding behaviors of the two intermediates allow for the stabilization of *COOH independent of *CO in a mechanism termed the covalency-aided electrochemical reaction (CAER). In a high-throughput screening of potential dopants in Ag, the d-block dopants displayed strong adherence to the linear scaling relations (figure 1-7a), whereas no such relations were found for the p-block dopants (figure 1-7b) [52]. These findings are also in agreement with experimental studies, where sulfur and phosphorus have been utilized to enhance the catalytic performance of Ag [52, 53].

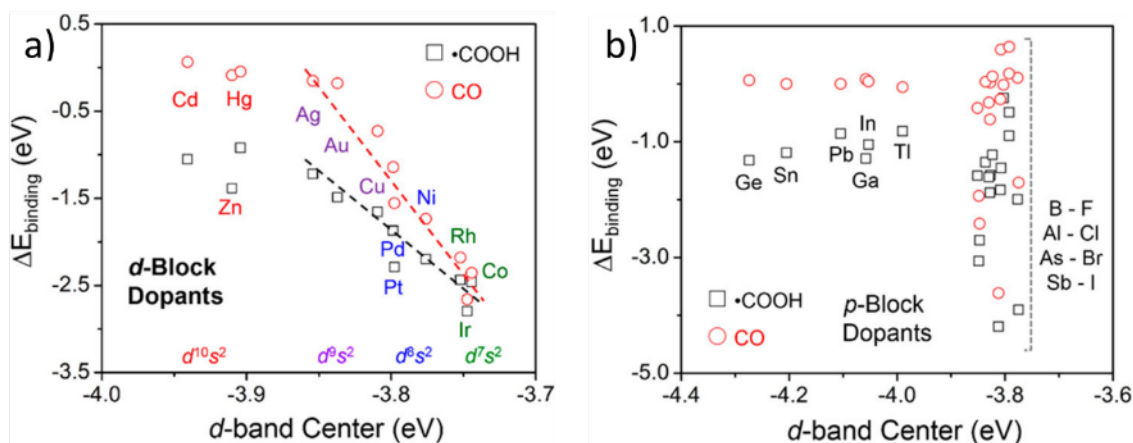


Figure 1-7 Intermediate binding energy as a function of the d-band center using a) d-block dopants and b) p-block dopants in Ag. Reproduced with permission from ref [52] Copyright 2014 American Chemical Society.

1.5.2 Promoting syngas formation

The above-mentioned strategies take aim at suppressing HER to enable high FE(CO) at low overpotentials. An alternative route is to combine HER with the CO₂RR to form syngas with adjustable H₂/CO ratios which can be utilized directly in existing thermocatalytic processes such as the Fischer-Tropsch or methanol synthesis. A specific H₂/CO ratio is necessary for each of these processes and is usually obtained from the water gas-shift reaction. In the water-gas shift reaction, CO and water at high temperature and pressure is converted into H₂ and CO₂ to obtain appropriate ratios [54]. On top of being an energy-intense process, the release of CO₂ as a byproduct raises environmental concerns. Thus, it incentivizes the development of catalysts for direct electrochemical syngas formation. Ag is a prime candidate as a catalyst for syngas formation due to its significantly lower cost compared to other alternative syngas catalysts like Au and Pd. However, the low catalytic activity of Ag needs to be addressed, and more importantly design strategies that enable control of the H₂/CO ratio need to be developed.

In effect, the strategies employed for enhancing syngas formation are very similar to those used to boost CO production highlighted above, but instead of maximizing FE(CO), the overarching goal is to develop a design where one parameter of the catalyst can easily be tweaked to tune the H₂/CO ratio while also maximizing the reaction rate. Therefore, nanostructures are often utilized, as the proportion of H₂/CO can be regulated by for instance manipulating the edge to surface ratio of nanoparticles. Another strategy that separates the design of Ag syngas catalysts from that of CO producing Ag catalysts is the widespread use of C supports. In general, C is not catalytically active for CO₂ reduction, but is rather used as a method for increasing the porosity of the catalyst to obtain large current densities and promote HER. These composite catalysts are designed according to figure 1-8, with Ag acting as the CO₂ reduction catalysts. Utilization of this strategy has shown that the H₂/CO ratio can be tuned by modifying the number of Ag nanowires deposited on C sheets [55]. In similar fashion, the overall Ag loading has also been used to control the syngas ratio [56].

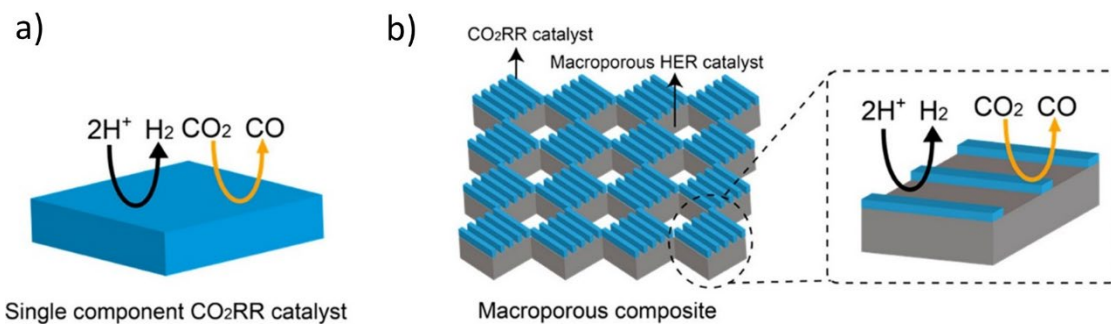


Figure 1-8 a) single-element and b) composite catalyst design for adjustable H₂/CO ratio from CO₂RR [57].

1.6 Research focus and objectives

The use of nanostructuring and light elements as dopants or modifiers in transition metal catalysts can have tremendous influence on their catalytic properties as discussed above. It is assumed that by precisely controlling the concentration of the modifier element, the product selectivity of the catalyst can be tuned, and depending on the material system the linear scaling relation can be circumvented. Still, the exploration of modifier elements beyond oxygen has been limited, in part due to complicated synthesis methods that often give unsatisfactory control over the concentration. Thus, in this project we aspired to design catalysts through the development of innovative synthesis processes aimed at nanostructuring and incorporating light elements into transition metals to manipulate their catalytic properties. An important aspect was to ensure control over the concentration of the modifier element. In this thesis three different catalyst designs are presented, an anodized Cu catalyst targeting the formation of C₂H₄, and two Ag-based catalyst, one modified with C for the purpose of syngas formation, and the other modified with B for the formation of CO. The project can be divided into four tasks as listed below:

Task 1: Design and build a reactor for the electrochemical reduction of CO₂ and quantification of gaseous reaction products.

Task 2: Develop a synthesis process for electrochemical anodization of Cu to yield a nanostructured Cu(OH)₂ catalyst for the formation of C₂H₄.

Task 3: Synthesize Ag-C thin film catalysts with controllable C concentration to enable syngas formation with tunable H₂/CO ratios at elevated current densities.

Task 4: Utilize a magnetron co-sputtering process to synthesize a B modified Ag catalyst to circumvent the linear scaling relation and enhance CO formation.

2 Experimental Setup

2.1 Reactor configuration

To evaluate the catalytic performance of the electrodes a reactor setup was needed to simultaneously monitor the reaction rate and analyze the gaseous reaction products. A continuous on-line reactor system was constructed, where an electrochemical H-cell is directly connected to a Shimadzu-GC-2010 PLUS gas chromatograph (GC). A mass flow controller was used to set the flow rate of CO₂ being continuously fed into a custom-made H-cell from Adams & Chittenden (figure 2-1). Injection of the gas stream into the GC was done using a 6-port gas sampling valve, which upon activation directs the content of the sampling loop into the carrier gas stream of the GC. Initially the measurements were performed with the H-cell directly connected to the gas sampling valve, but a significant amount of water vapor in the gas stream resulted in a large water peak that covered the peaks of interest. Therefore, a filter mechanism had to be implemented that could selectively remove the water vapor out of the gas stream without the loss of analytes. A Nafion tube dryer that could filter out water vapor continuously from the gas stream was selected for this purpose. The dryer is seen connected between the H-cell and gas sampling valve as seen in the schematic in figure 2-2 and works by allowing water vapor to permeate through a thin Nafion membrane. A dry gas, in this case nitrogen flows counter to the main gas stream to create a dry environment inside the steel casing surrounding the Nafion tubing to enable the water to permeate due to the existing gradient. The incorporation of the dryer into the sampling system significantly reduced the water peak from thousands of mV to ~100 mV.

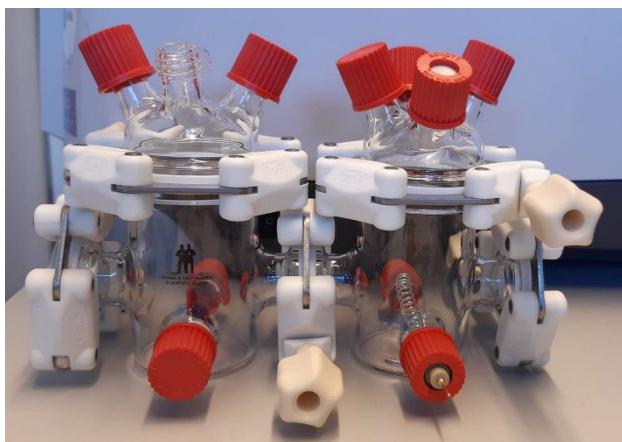


Figure 2-1 The H-cell used for the electrochemical reduction experiments.

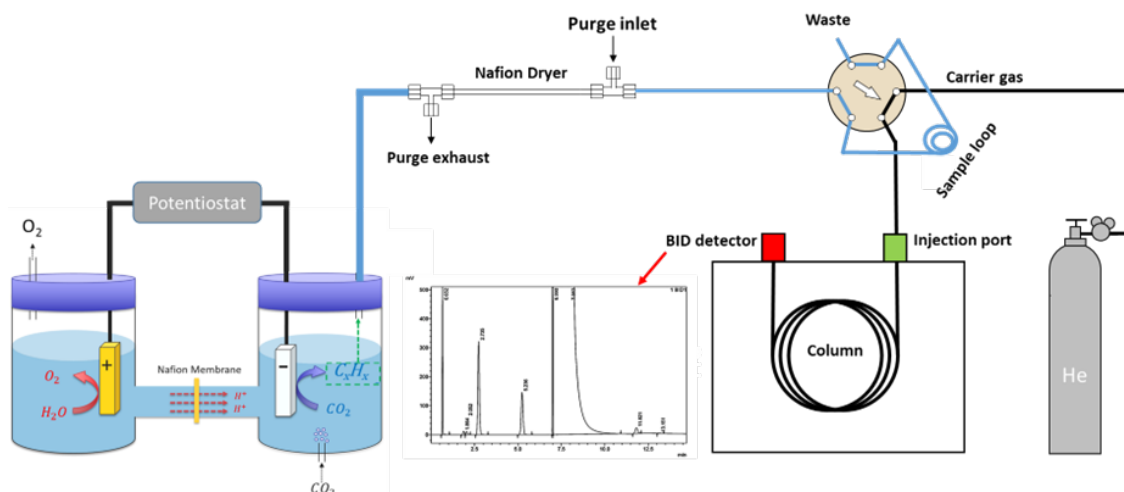


Figure 2-2 Schematic showing the reactor setup used for the electrochemical CO₂ reduction and gas quantification.

2.2 Electrochemical test conditions

All electrochemical experiments were performed using a three-electrode configuration with an Ag/AgCl (3 M KCl) reference and a Pt coil counter electrode. The cathodic and anodic chamber was separated by a Nafion 117 proton exchange membrane (PEM), and each chamber was filled with 75 mL of KHCO₃ electrolyte saturated with CO₂. The geometric surface area of the catalyst was typically 0.5 – 1 cm².

2.3 Quantification of gaseous reaction products

2.3.1 GC calibration and measurement parameters

The gas quantification was performed with a GC equipped with a barrier ionization (BID) detector and a ShinCarbon ST column. Initially, the GC measurements were performed under isothermal conditions with constant pressure (~400 kPa), which required lengthy measurements to detect ethylene (retention time ~27 minutes). Since multiple measurements at a given potential is necessary for it to be statistically significant it would require the electrochemical tests to run for extended amounts of time. Lengthy measurements are problematic since the catalyst might become unstable over the test period, giving incorrect FE's when averaging several measurements. More importantly, while the gas dryer significantly reduced the amount of water vapor, it did not eliminate it completely. This becomes a problem when the water peak starts to appear at the same time as the ethylene, making it hard to make consistent quantifications. To ensure that the peak of the water vapor did not interfere with the ethylene peak and to shorten the time required for each measurement the GC temperature and pressure program was optimized according to table 2-1. The measurement time was reduced to less than 15 minutes with ethylene appearing at 12 minutes using the temperature and pressure program seen in table 2-1. A further reduction in the measurement time could not be achieved since increasing the temperature beyond the settings given in table 2-1 led to an overlap of the water and ethylene peaks. The final temperature step from 150 – 200°C were added to ensure that the water vapor was eluded from the column before cooling down, increasing the total run time to 19 minutes. The pressure program also includes a reduction in pressure from 400 kPa to 100 kPa to permit switching of the gas sampling valves without suffering blow-back of gas inside the sampling loop back into the cell. This is important as it disrupts the flow, which can cause inconsistencies in the measurements or potentially damage the dryer. When the reaction products exclusively consist of C1 products, the measurement time can be further reduced by using the parameters in table 2-2. The detector parameters were the same for all measurements

(table 2-3). Figure 2-3 shows the GC spectrum obtained with the optimized parameters, which separates the C₂H₄ and water peak, while placing C₂H₆ on top of it.

Table 2-1 GC pressure and temperature program used for the quantification of gaseous reaction products, including hydrocarbons.

Pressure program		
Rate (kPa/min)	Pressure (kPa)	Hold time (minutes)
0	250	2.0
60	400	14.5
-400	100	0.3
Temperature program		
Rate (°C/min)	Temperature (°C)	Hold time (minutes)
0	30	2.0
10	150	0
20	200	2.5

Table 2-2 GC pressure and temperature program used for the quantification of H₂ and CO

Pressure program		
Rate (kPa/min)	Pressure (kPa)	Hold time (minutes)
0	250	2.0
60	400	3.73
-400	100	0.3
Temperature program		
Rate (°C/min)	Temperature (°C)	Hold time (minutes)
0	30	2.0
45	200	3.5

Table 2-3 GC parameters used for quantification.

GC parameters	
Injection temperature	150°C
Detector temperature	280°C
Purge flow	10 ml/min
Split ratio	20

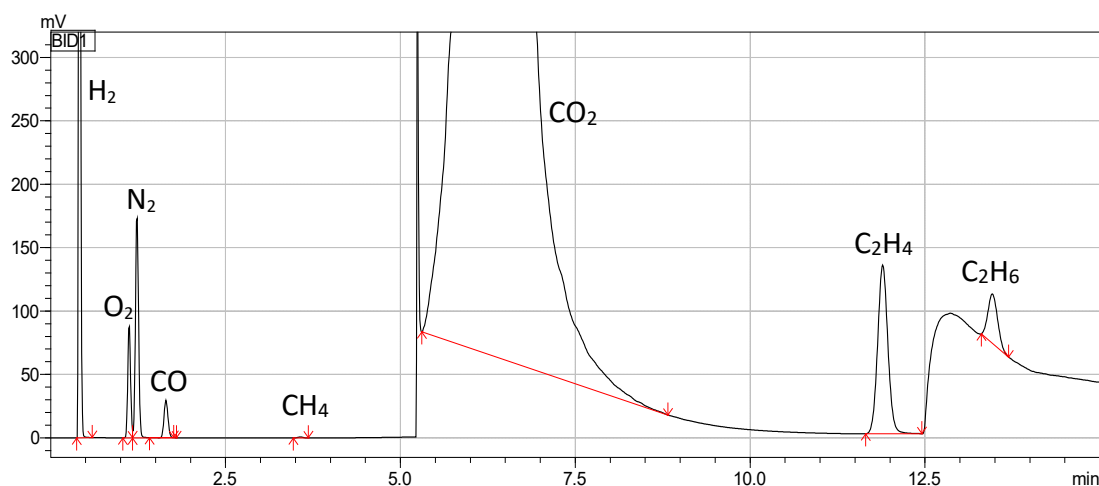


Figure 2-3 A typical GC spectrum obtained with the optimized GC program.

To quantify the gaseous reaction products the detector response (peak area or height) needs to be compared to that of an external standard with a known concentration. Initially, four custom gas mixtures containing various concentrations of the gases of interest with nitrogen as a balance gas were acquired. The calibration gas cylinders were connected directly to a mass flow controller and fed into the electrochemical cell and into the gas sampling valve. To make the environment as close to the reaction conditions as possible the cell was filled with electrolyte to mitigate any effect of the water vapor. Calibration curves were created for each of the gases, showing high linearity and repeatability. However, upon quantifying the reaction products generated from the electrochemical CO₂ reduction, it was found that the total calculated FE exceeded 100% and was often as high as 140%, which meant that the quantification overestimated the reaction product concentrations. After great lengths of troubleshooting, it was discovered that the error was with the calibration itself. The calibration gas used N₂ as

a balance gas, while the experiments effectively used CO₂ as balance as it is continuously pumped through the system. Therefore, upon attaining a new set of calibration mixtures with CO₂ as a balance (concentrations seen in table 2-4), the peak areas of the gases were reduced by approximately 40%. By using an Ag foil (produces only CO and H₂) and Pt (produces H₂) as working electrodes it was possible to achieve an FE of about 100%, verifying that the setup was working properly. Therefore, the choice of balance gas is tremendously important to ensure accurate quantification of the gases of interest. There are two possibilities for this occurrence, either it is due to CO₂ not being an ideal gas, meaning that it might compress and allow for additional analytes to enter the sampling loop, or it could be that the large concentrations of N₂ or CO₂ influences the BID detector response. Since the BID detector is less common than detectors like FID, the latter might be a possibility, but there is no reference to this in the literature. The calibration curves were created using a weighted linear fit (1/C) without forcing the line through origin, where the C represents the concentration of the gas. The calibration curve for H₂ (100-3000 ppm) can be seen in figure 2-4. The R² of the calibration curves was ~0.99 for all gases.

Table 2-4 Gas concentrations used for creating the calibration curves.

Concentration (ppm)				
H ₂	CO	CH ₄	C ₂ H ₄	C ₂ H ₆
100	40	20	20	10
300	200	200	200	100
3000	2000	2000	2000	1000

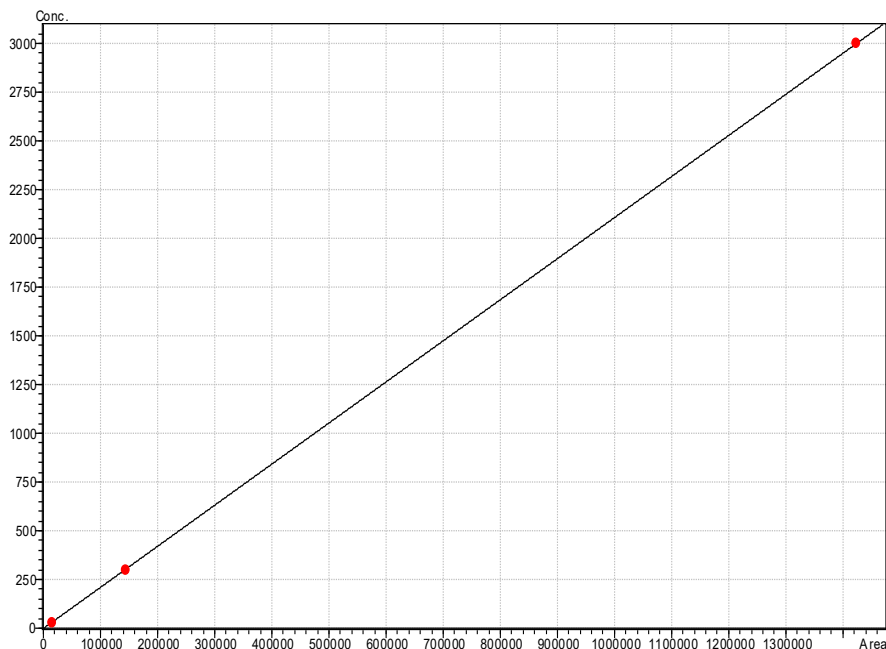


Figure 2-4 GC Calibration curve for H₂ with concentration in parts per million as a function of peak area.

2.3.2 Calculating the Faradaic efficiency

Faradaic efficiency for a given product was calculated using equation 2:

$$FE = \frac{m \times n \times F}{Q} \times 100 \quad (2)$$

Where m is the mol of product obtained by multiplying the mol% value derived from the GC measurements with the total moles contained in the sampling loop assuming standard pressure and temperature. The number of electrons required to produce a given product is given as n . F is Faraday's constant (96500 C/mol), and the charge Q is found by multiplying the current (I) with the time (t) it takes to fill the sampling loop considering a gas flow (f) of 20 sccm.

As an example, given $I = 5$ mA, $f = 20$ sccm, and the detection of 1060 ppm of H₂. The total moles in the sample loop can be determined using the ideal gas law in equation 3:

$$PV = nRT \quad (3)$$

Where P is the pressure, T is the temperature, V is the volume, n the amount of substance and R the ideal gas constant. At standard pressure and temperature, there is a total of 4.09×10^{-5} mol in 1 mL. Since 1060 ppm equals 0.106 mol%, this can be multiplied by the total moles in the sampling loop, which gives $\sim 4.34 \times 10^{-6}$ mol of H₂.

To find the charge Q , the time (t) it takes to fill the sampling loop needs to be found from equation 4:

$$t = \frac{\text{sample loop volume (1 mL)}}{20 \text{ mL/min}} \times 60 = 3 \text{ s} \quad (4)$$

The charge then becomes:

$$Q = I \times t = 5 \text{ mA} \times 3 \text{ s} = 0.015 \text{ C} \quad (5)$$

Considering that 2 electrons is needed to produce H₂ ($n=2$), the FE is calculated from equation 6:

$$FE = \frac{4.34 \times 10^{-6} \text{ mol} \times 2 \times 96485 \frac{\text{C}}{\text{mol}}}{0.015 \text{ C}} \times 100\% = 55.83\% \quad (6)$$

3 Summary of Main Research

3.1 Copper hydroxide nanoneedles (Article 2)

Motivation

Cu(OH)₂ has proven itself to be an excellent catalyst for the electrochemical reduction of CO₂ into C₂H₄ [58]. Anodization of Cu foil is the most attractive method for synthesizing Cu(OH)₂ films since large areas can be attained, while also providing high aspect ratio nanoneedle growth. However, the film quality is highly dependent upon the initial conditions of the Cu foil surface, where surface irregularities and insufficient wettability can lead to poor current distribution and thus an inhomogeneous film in terms of both thickness and morphology. A common process applied to circumvent this problem consists of first using HCl to remove surface oxides, and then apply mechanical and electrochemical polishing to remove crevices and surface irregularities [59-62]. A combination of these methods would normally be necessary to achieve satisfactory film quality. Therefore, we aimed to streamline the pre-treatment process into a single step by using Na₂S₂O₈. This approach could address both the problem of surface oxides and surface irregularities simultaneously.

Experiments

With the foregoing motivation in mind, a process was developed for growing homogenous Cu(OH)₂ nanoneedles over large surface areas (> 10 cm²). The method is intended to significantly simplify the synthesis of Cu(OH)₂ films by reducing the Cu foil pre-treatment to a single step, and thus making Cu(OH)₂ a viable catalyst material for large scale reactors. In the following study, the process was used to grow homogenous films over Cu foils with a surface area of 63 cm². First, the Cu foils were cleaned using acetone and isopropanol before being rinsed with DI water. Etching of the top-most surface was then performed by dipping the Cu foil in 20% Na₂S₂O₈ solution for 5 minutes and 30 seconds. The samples were rinsed using DI water followed by ethanol before

drying the samples with nitrogen. Anodization of the copper foil was then performed in 3 M KOH solution in a Teflon beaker according to the process described in figure 3-1.

Results and discussion

The process that was developed utilizes a single pre-treatment step of the Cu foil, which is intended to remove surface oxides and crevices or other surface irregularities. A light-blue film is observed following the anodization process, indicative of Cu(OH)₂. When the pre-treatment step is left out, a significant number of pinholes are observed. Additionally, contact angle measurements reveal that the surface energy is considerably increased upon pre-treatment, enhancing the wettability of the Cu foil when immersed in the KOH solution.

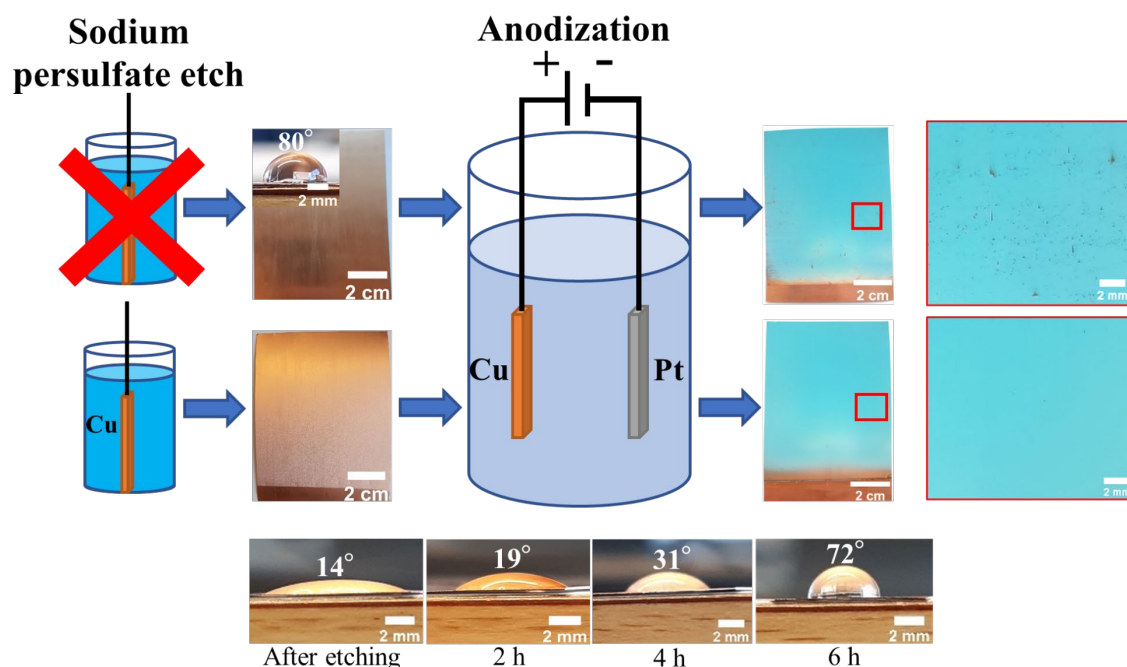


Figure 3-1 Process flow showing the development of the Cu(OH)₂ nanoneedle films.

Investigation of the Cu foil before (figure 3-2a) and after pre-treatment (figure 3-2d) shows that crevices are removed upon pre-treatment, but a lower hierarchy surface roughness has been added. Furthermore, it was found that the pinholes consisted of empty areas that are 30-50 μm in size as seen in figure 3-2b. There were also several patches where the growth of nanoneedles had been inhibited (figure 3-2c). On the other hand, the Cu(OH)₂ film that was grown on the pre-treated Cu foil showed a high density

of nanoneedles without the presence of patches (figure 3-2e). The nanoneedles were ~ 200 nm wide at the needle tip (figure 3-2f), and the film was ~ 21 μm thick.

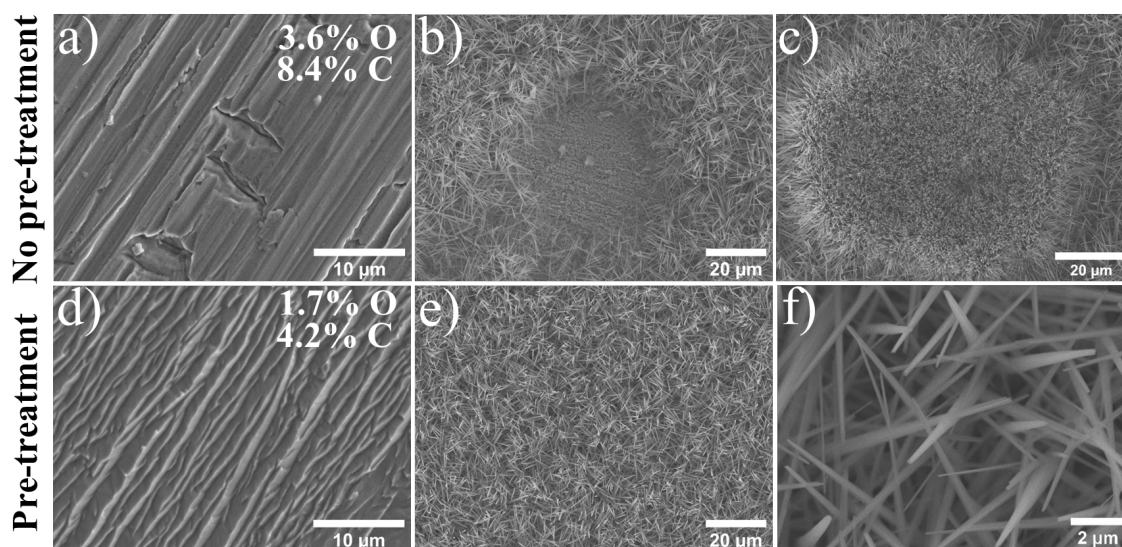


Figure 3-2 SEM images of the a) pristine Cu foil, b)-c) pinhole and patch with reduced growth found on the anodized Cu foil. SEM images of the d) Cu foil after pre-treatment with sodium persulfate, e)-f) the surface morphology of the pre-treated Cu foil after anodization.

Electron dispersive spectroscopy (EDX) measurements performed inside the pinhole revealed a layer of Cu_2O . The layer was estimated to be ten times thicker than the native oxide layer measured at the pristine Cu foil. Such a thick oxide layer could create an insulating area which could fully or partially block the growth of $\text{Cu}(\text{OH})_2$ as seen in figure 3-2b-c. Side reactions such as the formation of Cu_2O , which is more prevalent at lower current densities might also occur if the site is sufficiently blocked. EDX was also performed at the nanoneedles of the sample that had undergone pre-treatment, with the EDX spectrum showing an atomic ratio of approximately 2:1 of oxygen to copper. The presence of the $\text{Cu}(\text{OH})_2$ phase was confirmed by x-ray diffraction (XRD), with peaks indicating an orthorhombic $\text{Cu}(\text{OH})_2$ phase. Smaller peaks were also detected, showing the presence of Cu_2O and CuO . The presence of $\text{Cu}(\text{OH})_2$ was also confirmed by Fourier-transform infrared spectroscopy (FTIR), with peaks at 3566 cm^{-1} and 3296 cm^{-1} , which can be attributed to the free OH group and the hydrogen bonded OH group, respectively [63]. Additionally, the peaks at 934 cm^{-1} and 678 cm^{-1} are due to the Cu-O-H bonds [64].

Figure 3-3a-b shows the product selectivity for the Cu foil and the Cu(OH)₂ catalyst. As expected, the Cu foil displays the highest selectivity for CH₄ at all potentials with an exception at -0.9V vs. RHE where the FE for C₂H₄ is slightly higher. As for the Cu(OH)₂ catalyst, C₂H₄ is the main reaction product at all potentials. Contrary to the Cu foil, there is almost no formation of CH₄ occurring over Cu(OH)₂. Due to the increase in surface area resulting from the nanoneedle structures the current densities were normalized to the electrochemical active surface area (ECSA) to identify any increase in intrinsic activity. The roughness factor of the Cu(OH)₂ catalyst was 6.17 relative to the Cu foil. The ECSA normalized current density and FE(C₂H₄) over the course of the stability test can be seen in figure 3-3c. While the Cu foil exhibits a larger ECSA normalized current density than the Cu(OH)₂, it quickly declines together with the FE(C₂H₄). Over the duration of the stability test, the Cu foil goes from a FE(C₂H₄) of ~19% to ~4%. The decline was accompanied by a doubling in the FE(H₂), revealing a deactivation of the active sites for CO₂ reduction and proves the inherent instability of the Cu catalyst. As for the Cu(OH)₂ catalyst, it displays excellent retention of FE(C₂H₄) while also showing a slight increase in current density. The ratio of the FE(C₂H₄) to FE(CH₄) together with J_{C₂H₄} (geometrical) can be seen in figure 3-3d. A decline in the product ratio of 10.6 is observed over the six hours, mainly due to FE(CH₄) increasing from 0.6% to 1.2%. Still, a ratio of 27.8 is retained after six hours, which proves the excellent selectivity for C₂H₄ over CH₄ for the Cu(OH)₂ catalyst.

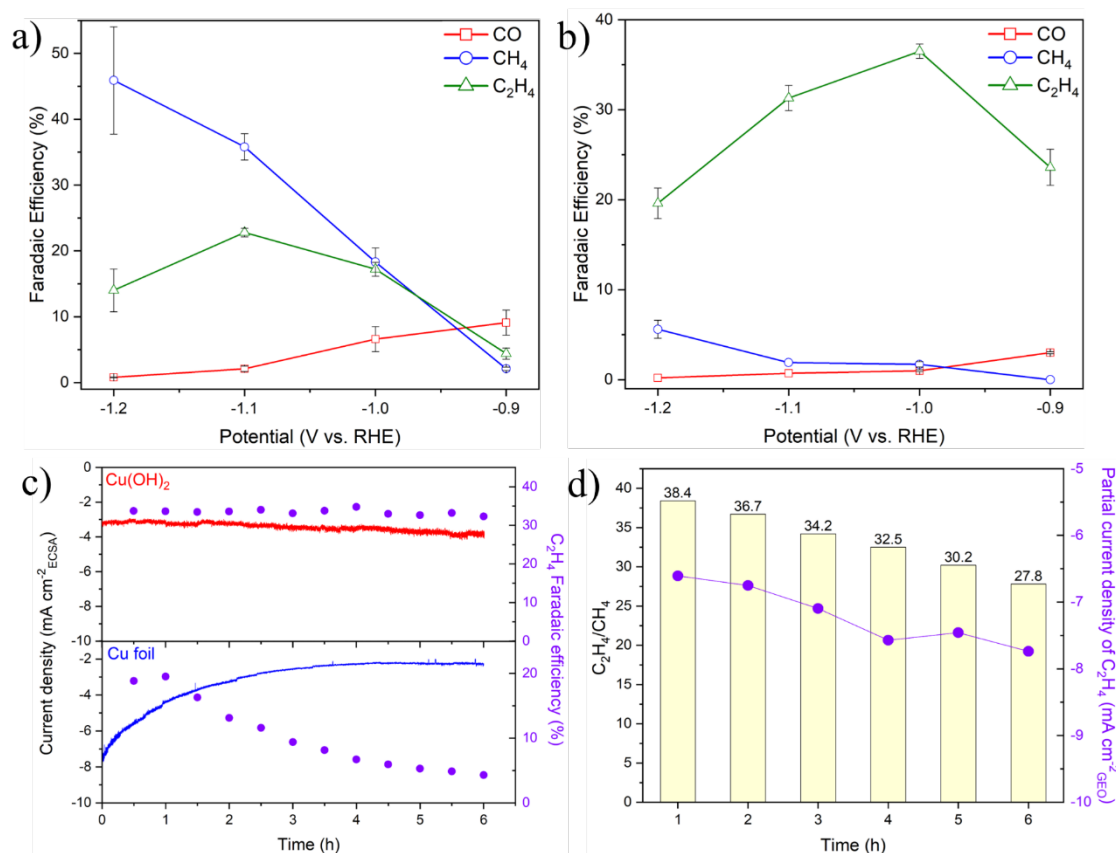


Figure 3-3 Electrochemical characterization: a) selectivity of the Cu foil catalyst, b) selectivity of the Cu(OH)₂ catalyst, c) stability test, and d) C₂H₄ to CH₄ ratio and C₂H₄ partial current density obtained for the Cu(OH)₂ catalyst during the stability test.

Conclusion

A two-step anodization process was developed to produce homogenous Cu(OH)₂ nanoneedle films over larger areas. The method consisted of a sodium persulfate pre-treatment of the Cu foil, which simultaneously removes native oxides, contaminations, and crevices or other surface irregularities. Cu foils that underwent pre-treatment also exhibited an increase in surface energy, which improved the wetting and resulted in enhanced contact between the KOH and Cu foil interface. The Cu(OH)₂ films displayed excellent catalytic performance for the electrochemical reduction of CO₂, with a clear preference for C₂H₄ formation over CH₄, reaching an FE(C₂H₄) of 36.5% at -1.0V vs. RHE. Moreover, the catalyst showed stable formation of C₂H₄ over the course of the 6-hour stability test, whereas the Cu foil reference rapidly declined in terms of both C₂H₄ selectivity and current density while doubling the HER selectivity.

3.2 C-modified Ag catalysts (Article 3)

Motivation

The formation of CO from the CO₂RR faces challenges such as the activation of the CO₂ molecule and competition with the HER, leading to low FE. Therefore, significant effort has been dedicated to suppressing HER to increase the FE(CO). An alternative solution is to combine HER with CO₂RR to produce syngas with adjustable H₂/CO ratio that can be utilized directly in thermocatalytic processes such as Fischer-Tropsch and methanol synthesis, and thereby eliminating the energy-intensive water-gas shift reactions that emits CO₂ as a side product.

Transition metals belonging to group two, such as Au, Ag, and Pd have been explored for this purpose due to their ability to form CO. Among them, Ag is the most attractive due to its significantly lower cost but exhibits the lowest catalytic activity. Nanostructuring of Ag has been used to improve performance and reduce costs. These nanostructures are often supported by C, which enhances reaction rates and gives control over the H₂/CO ratio. In this regard, the synthesis of Ag-C thin films by co-sputtering is an attractive prospect since it provides control of the C concentration and film thickness while also offering the opportunity for scale-up. Moreover, the porosity of C can maximize the exposed surface area without the use of binders that are utilized to attach nanostructures to electrodes, which have the potential to block active sites [55].

Experiments

Soda-lime glass wafers were diced into 3.0 x 0.5 cm² pieces and were subsequently ultrasonically cleaned for 10 minutes in acetone before rinsing with isopropanol. The samples were then subject to 10 minutes of plasma at a power of 300 W in a plasma cleaner using an Ar gas flow of 50 sccm and an O₂ flow rate of 100 sccm at a pressure of 58 Pa. Next, the samples were loaded into the sputtering chamber where a 15 nm adhesion layer of Cr was deposited using e-beam evaporation. The Ag-C films were deposited through co-sputtering, where the DC power of the Ag target was set to 100

W and the RF power of the C target was 350 W and 500 W to create two thin films with different concentrations of C, which will be referred to as Ag-C-1 Ag-C-2, respectively. A pristine Ag thin film was also synthesized as a reference.

Results and discussion

Surface morphology of the sputtered films can be seen in figure 3-4a-c. The pristine Ag film consists of large grains, approximately 150 nm wide. When C is co-sputtered with Ag the particles shrink to ~35 nm for the Ag-C-1 and ~25 nm for the Ag-C-2. Both Ag-C films have a similar morphology except for a slight difference in particle size and more cluster formation for the Ag-C-2 film. EDX measurements gave C concentrations of 2.3 at% for pristine Ag, which increased to 7.6 and 13.4 at% for the Ag-C-1 and Ag-C-2, respectively. The EDX spectrum obtained for the Ag-C-2 film is seen in figure 1d inset. Detection of C in the pristine Ag film was attributed to the presence of C on the surface. The XRD patterns (figure 3-4d) show a polycrystalline structure with a dominant Ag (111) peak for the pristine Ag film, whereas the addition of C reduced the Ag (111) peak intensity while simultaneously broadening the peaks. The broadening of the peaks can be explained by the reduction in the crystallite size. The Debye-Scherrer equation was used to calculate the average crystallite size, which was 18.8 nm, 14.0 nm, and 9.5 nm for the Ag, Ag-C-1, and Ag-C-2, respectively. The reduction in particle and crystallite size suggests that the growth kinetics are disrupted when C is co-sputtered with Ag. More specifically, the nucleation rate is increased with increasing concentration of C due to the competitive growth of the two materials, leading to suppressed growth of Ag and smaller particles.

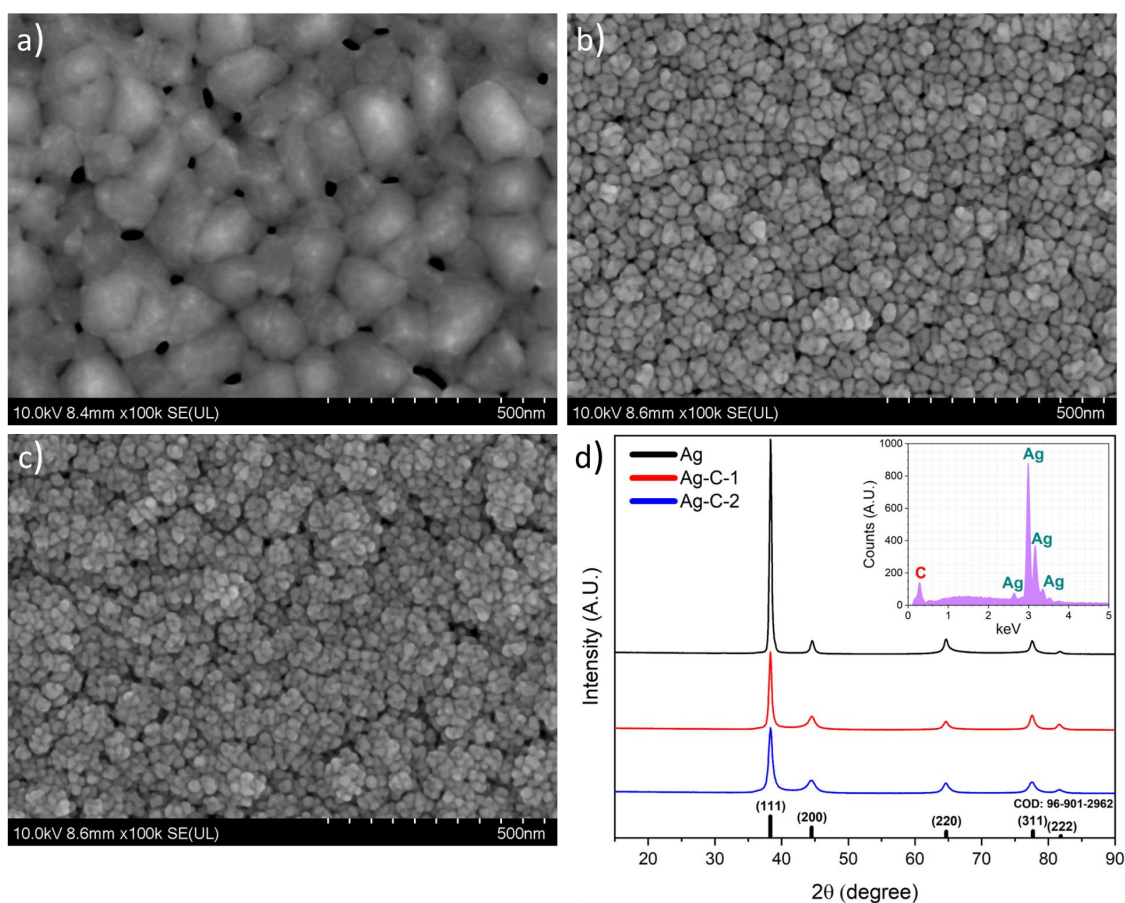


Figure 3-4 SEM image of the a) Ag, b) Ag-C-1, and c) Ag-C-2 films. d) XRD patterns of the Ag and Ag-C films with the EDX spectrum obtained for the Ag-C-2 film inset.

The catalytic properties of the films were studied by conducting electrochemical CO₂ reduction in a potential range from -0.6 to -1.0 V vs. RHE. A drastic increase in current density was observed in the LSV for the Ag-C films relative to Ag (figure 3-5a). CO and H₂ were the only gaseous reaction products detected for the catalysts, with a total FE close to 100% as seen in figure 3-5b. Ag showed a steady increase in FE(CO) as the potential became more negative, with an FE(CO) of 84.5% at -1.0 V vs. RHE. A decline was seen in the CO selectivity in favor of HER when the C concentration increased. The Ag-C-1 and Ag-C-2 achieved a peak FE(CO) of 56.1% and 40.4% at -0.9 V and -0.8 V vs. RHE, respectively. Thus, as the C concentration increased the selectivity towards HER was enhanced. However, the catalytic activity was significantly increased for the Ag-C catalysts with the J_{CO} exceeding that of Ag at all potentials. It should be noted that the difference in J_{CO} was subtle at -1.0 V vs. RHE due to the increase in FE(CO) for Ag in combination with a decrease in FE(CO) for the Ag-C catalysts. A more substantial

increase was seen in J_{H_2} for the Ag-C catalysts, with the J_{H_2} being 28-fold higher for the Ag-C-2 catalyst compared to Ag at -1.0 V vs. RHE. A H_2/CO ratio of ~ 1 is obtained for Ag at -0.6 V vs. RHE, which rapidly declines as the potential becomes more negative, reaching ~ 0.1 at -1.0 V vs. RHE (figure 3-5c). The Ag-C-1 catalyst displays a similar trend as Ag as a function of the applied potential, but the H_2/CO ratio went from 2.5 – 0.8 in the potential range from -0.6 to -1.0 V vs. RHE. Interestingly, a parabolic curve is obtained for Ag-C-2, with start and endpoints above 2. Thus, the H_2/CO ratio can be tuned by adjusting the C concentration of the thin films and by controlling the applied potential. It was found that the Tafel slope was increased for the Ag-C catalysts relative to Ag (figure 3-5d), suggesting that the increase observed in J_{CO} was not due to improved reaction kinetics.

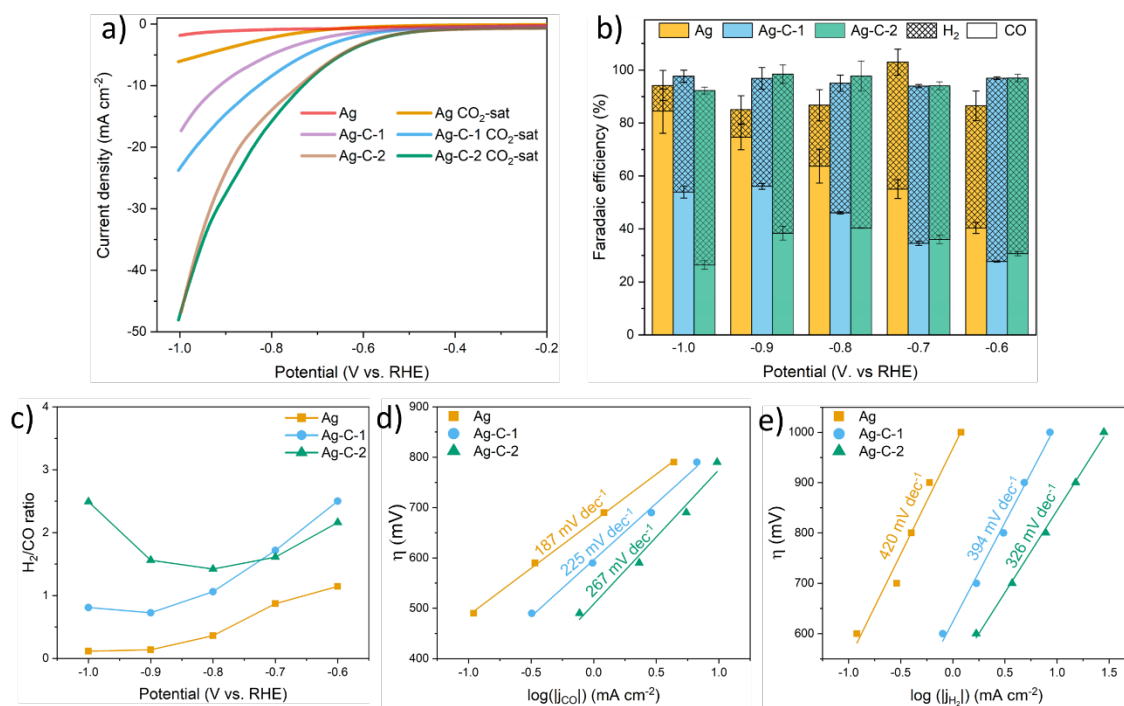


Figure 3-5 Electrochemical characterization of the Ag-C catalysts. a) LSV of the Ag and Ag-C catalysts, b) their product selectivity as a function of potential, c) the ratio of H₂/CO for the Ag-C catalysts, the Tafel slope for d) CO and e) HER.

The ECSA was therefore calculated using the C_{DL} obtained through conducting CV scans at various scan rates in the non-faradaic potential region and plotting the peak-to-peak current density as a function of scan rate. Ag had a C_{DL} of 0.16 mF/cm², which increased to 5.13 mF/cm² for Ag-C-1 and 7.71 mF/cm² for Ag-C-2. This translates to a roughness factor relative to the Ag reference of 32 and 48 for the Ag-C-1 and Ag-C-2 catalyst, respectively. This translates to an ECSA of 0.75 cm² (Ag), 27 cm² (Ag-C-1), and 36 cm² (Ag-C-2), thus, the ECSA is significantly increased for the Ag-C films, which explains the large current density.

Conclusion

The co-sputtering of C with Ag reduces the particle size from ~150 nm to < 40 nm while simultaneously reducing the crystallite size due to an increase in the nucleation rate that suppresses Ag growth. A significant increase in the current density is observed for the Ag-C films relative to Ag, but the overall selectivity for CO is reduced in favor of HER. The smaller particle size and increased porosity due to C leads to a substantial increase in the ECSA. Thus, the Ag-C films can generate large geometric current densities due to an abundance of active sites, with the ability to tune the H₂/CO ratio, which is an important feature for the design of syngas catalysts.

3.3 Ag-B catalysts (Article 4)

Motivation

Developing catalysts capable of selectively producing CO at low overpotentials is highly attractive since CO can be utilized in the Fischer-Tropsch process to produce hydrocarbons. Formation of CO occurs for catalysts that exhibit low binding energy of *CO, such as Au and Ag. Naturally, Ag would be the preferred choice due to its lower cost, allowing for large-scale industrial reactors. However, compared to Au, Ag requires significantly larger overpotentials to reach satisfactory FE(CO). It has been shown that the overpotential is linked to the activation barrier for *COOH formation, indicating that increasing the binding energy of *COOH could lower the overpotential. Unfortunately, the linear scaling relations between the d-band center and the *COOH and *CO intermediates prevents the tuning of the binding strength of *COOH and *CO independently by d-band modulation. Therefore, there needs to be a decoupling between the d-band center and the intermediate binding energies. The utilization of p-block elements as modifiers of Ag has emerged as an attractive strategy to circumvent these scaling relations. Among the p-block elements, B has been extensively used as a modifier with great success in other transition metals for electrochemical CO₂ reduction [34, 65]. With that as a motivation, B was incorporated into Ag to determine its impact on the catalytic properties of Ag.

Experiments

The catalyst synthesis is identical to the process reported for the Ag-C thin films, with the exception that the soda-lime glass pieces in this case were 2.5 x 0.5 cm². The Ag was deposited with a DC power of 100 W while simultaneously depositing B with an RF power varied in the range of 0-150 W at room temperature as depicted in figure 3-6. The resulting film thickness was ~1.7 μm as determined by scanning transmission electron microscopy (STEM).

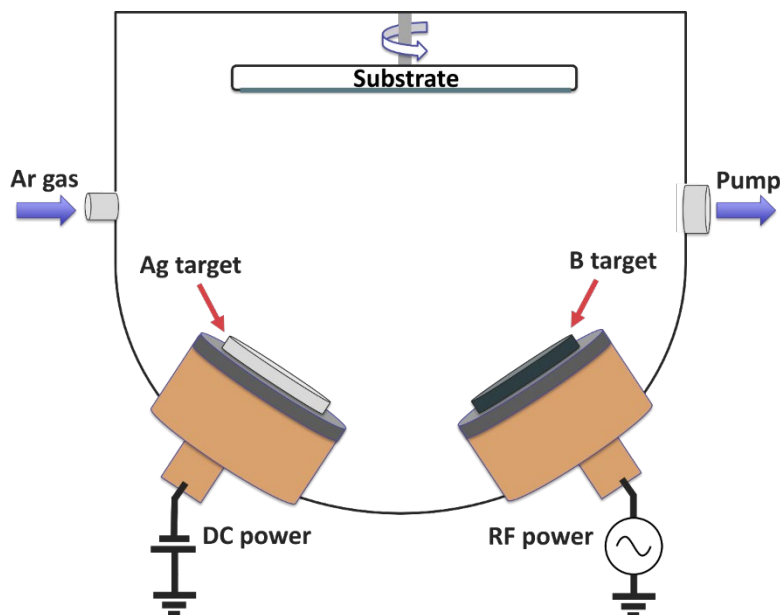


Figure 3-6 Schematic showing the co-sputtering arrangement used for growing the Ag-B films.

Results and discussion

DFT simulations were performed to evaluate B as a modifier in Ag, and to determine the effect on the reaction mechanisms of the electrochemical reduction of CO₂ to CO. The model consisted of an Ag (111) slab with B placed interstitially into the Ag lattice. A change in the band structure is observed with the incorporation of B into Ag (figure 3-7a-b). More specifically, the d-band center is shifted by 0.24 eV towards the fermi level for Ag-B (figure 3-7c). Looking at the free-energy profile for the electrochemical reduction of CO₂ to CO (figure 3-7d), the formation of *COOH remains the rate-determining step (RDS) for both Ag and Ag-B. However, the activation barrier for *COOH formation is lowered from 1.58 eV to 1.33 eV when B is placed into the Ag lattice due to a stronger binding strength of *COOH, in line with the observed shift in the d-band. Interestingly, the shift in the d-band center should also increase the binding strength for *CO according to the linear scaling relations, which is not the case for the Ag-B surface. On the contrary, the *CO binding strength is reduced by 0.15 eV, demonstrating a deviation from the linear scaling relations. Thus, the free-energy profile is in line with the trend observed for p-block elements in Ag and the CAER mechanism proposed by

Lim et.al. [52] where the *COOH intermediate can be stabilized independent of *CO. As the DFT simulations indicated that B could enhance the catalytic performance of Ag we proceeded to synthesize B modified Ag films.

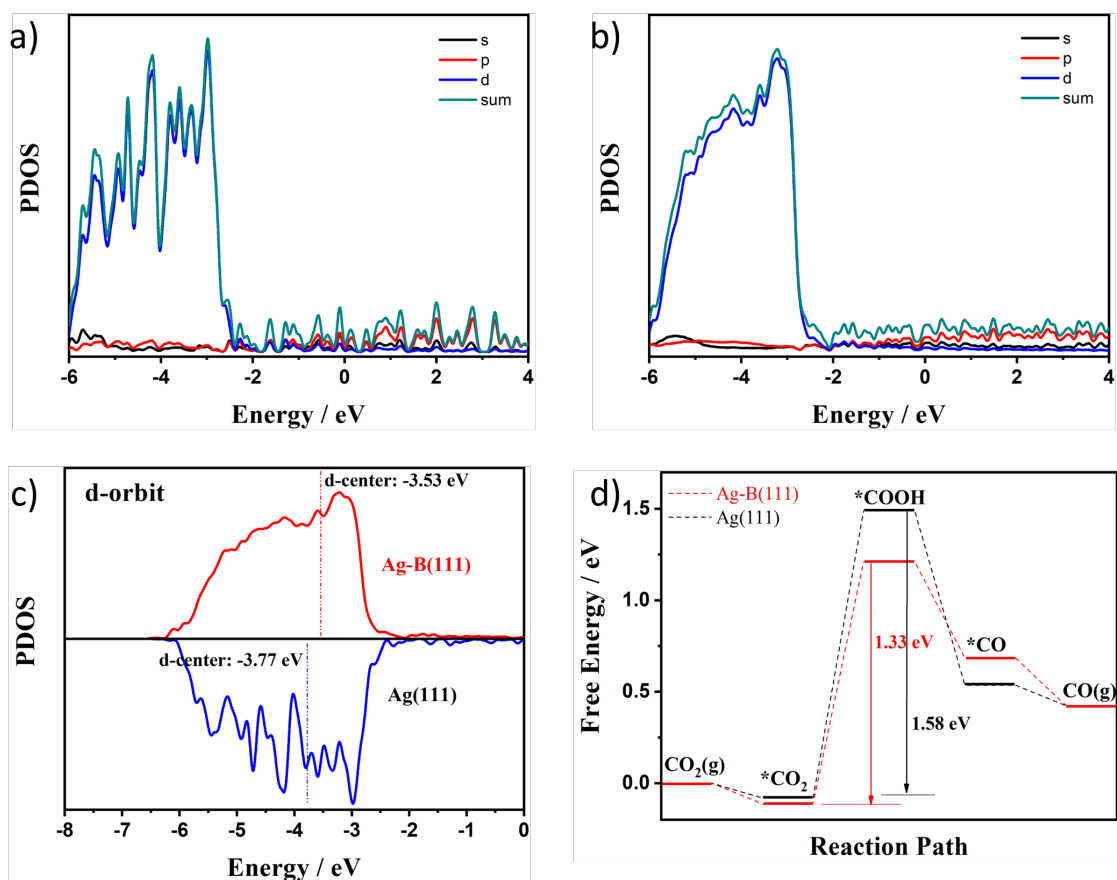


Figure 3-7 Band structure of the a) Ag-B (111) and b) Ag (111) slabs. c) comparison of the d-bands of the two slabs, showing the change in d-band center. d) free energy diagram for CO₂ reduction over the two surfaces.

In total three films with varying concentrations of B were deposited. These were labelled according to the RF power of the B target during deposition as Ag (0 W), Ag-B-1 (100 W), and Ag-B-2 (150 W). The structural properties of the films were investigated using XRD, of which the resulting XRD patterns of the films can be seen in figure 3-8a. As for most metals deposited by DC magnetron sputtering, the pristine Ag film displays an XRD pattern characteristic of a polycrystalline FCC crystal structure. Interestingly, the incorporation of B significantly increases the intensity of the Ag (111) peak while simultaneously reducing the intensity of the rest of the Ag peaks. The Ag (111) peak intensified when increasing the RF power of the B target, whereby the Ag (111) peak

became totally dominant for the Ag-B-2 sample. Ag and B can form the AgB₂ phase with a dominant peak at ~28°, but no such peak could be found for any of the films. A shift of the Ag (111) peak towards lower angles was also found for the Ag-B films (figure 3-8b), indicating an expansion of the lattice due to the incorporation of B.

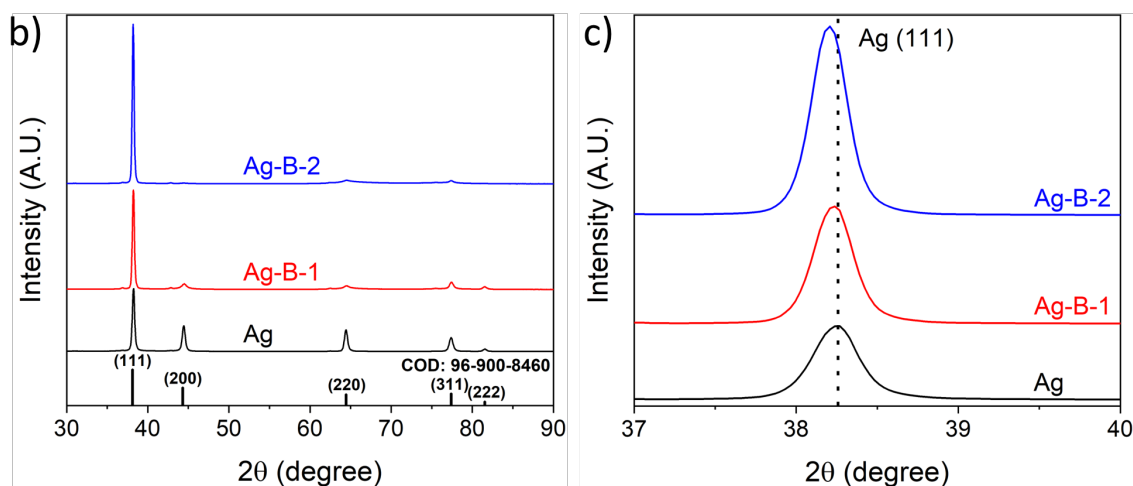


Figure 3-8 a) XRD spectra of the Ag and Ag-B films and b) zoomed in plot showing the Ag (111) peak.

Next, TEM was employed to gain insight into the crystal transformation observed from the XRD patterns. A high density of columns aligned in the growth direction is revealed by the cross-sectional imaging in figure 3-9b. Further investigation of these columns shows a significant number of Ag (111) coherent twin boundaries approximately 5-10 nm wide that are aligned perpendicular to the growth direction (figure 3-9c-e). The lattice spacing is determined as 2.385 Å, significantly larger than 2.360 Å which is expected for Ag (111). Thus, it shows that the B is incorporated into the Ag lattice. Selected area electron diffraction (SAED) (figure 3-9b inset) gives a spotted pattern typical of a single crystal structure, with duplicate points induced by the twinned crystal structure. Thus, the increase in the Ag (111) intensity in the XRD pattern is a result of Ag (111) twin boundary growth, which is facilitated by the incorporation of B. In general, the growth of twin boundaries is related to the stacking fault energy (SFE). When the SFE is sufficiently low it favors the formation of twin boundaries. As for Ag, the growth of twin boundaries by sputter deposition occurs exclusively for epitaxially growth Ag [66]. However, there are examples where adding minute impurities of non-metals to Ag

can lower its SFE [67]. Thus, it is a reasonable assumption that when added to Ag, B can effectively lower the SFE to facilitate twin boundary growth.

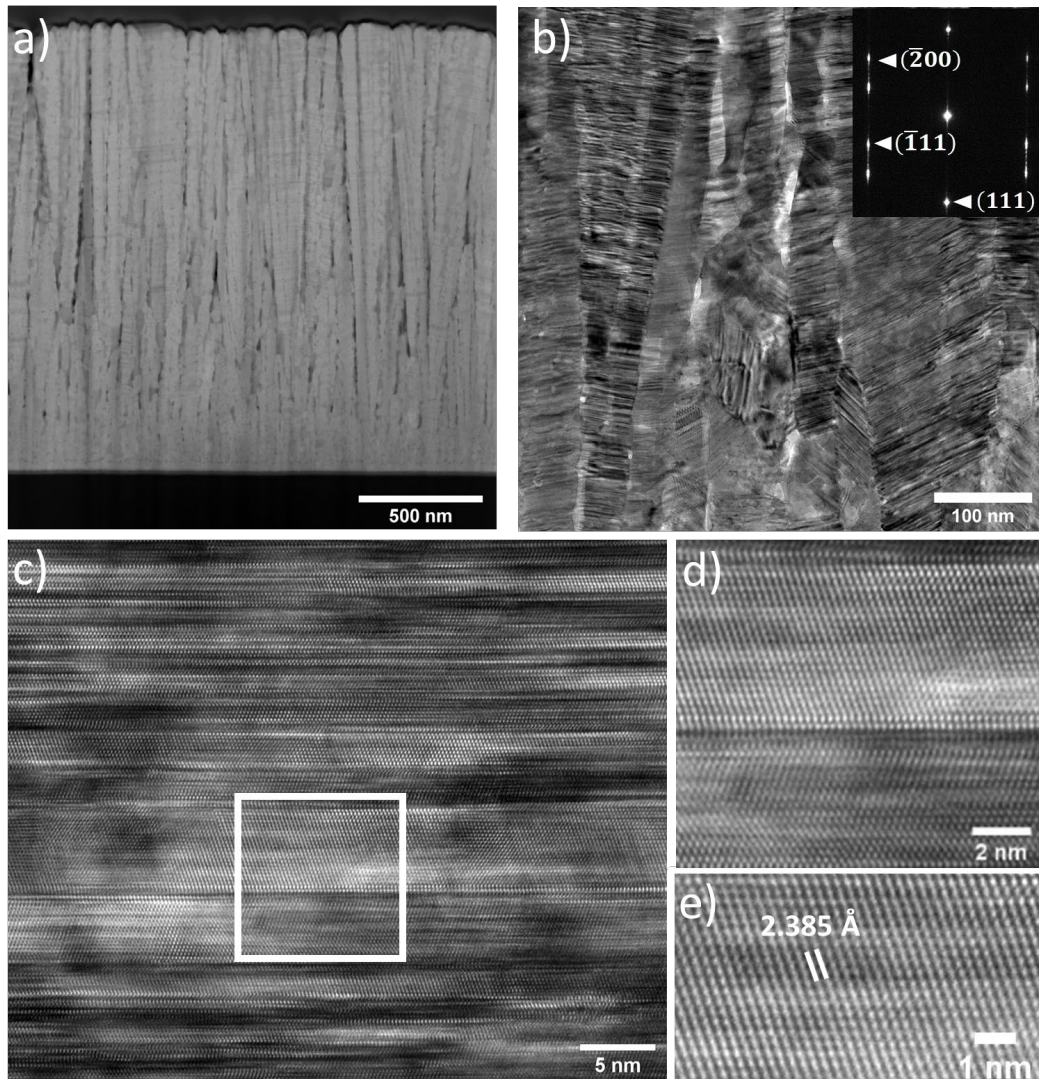


Figure 3-9 TEM images of the Ag-B-2 film. a) STEM, b) HRTEM with SAED (inset), c)-e) HRTEM of the coherent twin boundaries.

Drastic changes are also observed for the surface morphology of the films, as evident from the SEM images in figure 3-10. The pristine Ag film consists of a granular morphology with large grains that are ~ 100 nm wide. Whereas the co-deposition of B with Ag give rise to nano-tentacle structures, with a mixture of grains and nano-tentacles displayed for the Ag-B-1 film, whereby a complete transformation to nano-tentacle structures is seen for the Ag-B-2 film.

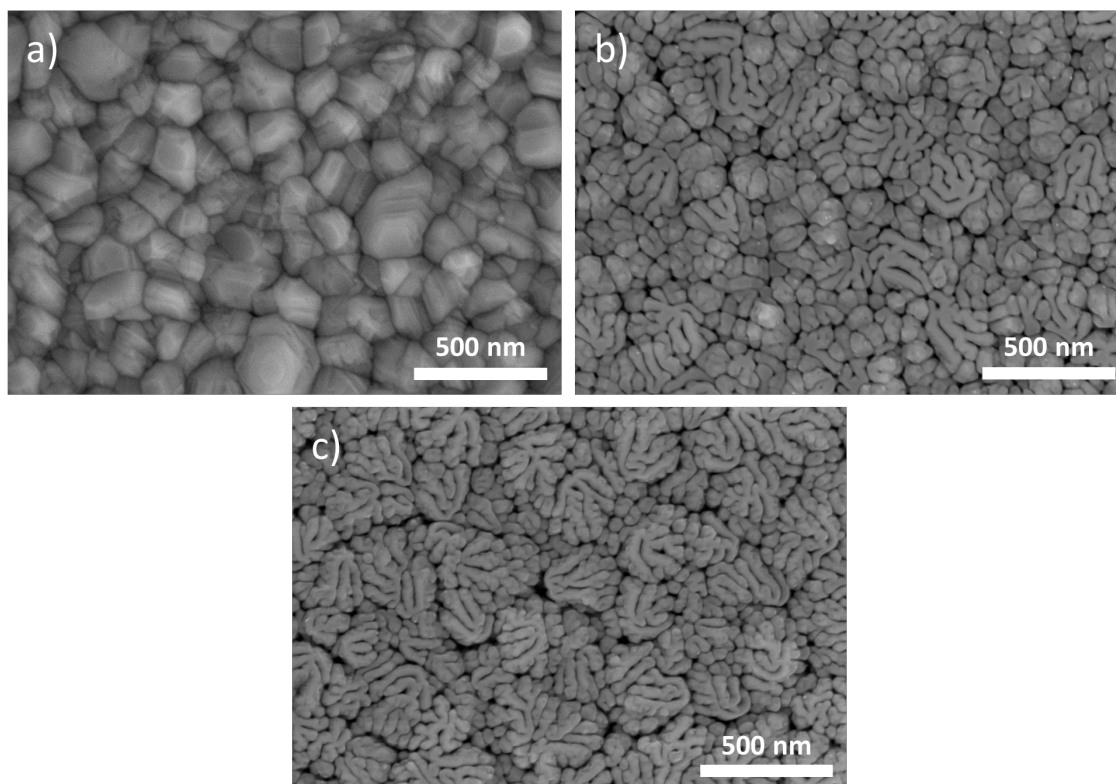


Figure 3-10 SEM images of the a) Ag, b) Ag-B-1, c) and Ag-B-2.

A similar morphology was attained by AFM, and the surface roughness increases from ~ 7.2 nm for the pristine Ag, to 12.0 nm for the Ag-B-2 film. There is less than 1 nm difference in surface roughness between the B containing films.

The chemical structure of the films was characterized by x-ray photoelectron spectroscopy (XPS) and Auger electron spectroscopy (AES). XPS measurements resulted in the detection of the B1s peak at ~ 188 eV for both the Ag-B-1 and Ag-B-2 films (figure 3-11), giving concentrations of 7 and 19 at%, respectively. Strong Ag 3d peaks are detected for all the films and a positive peak shift of about 0.2 eV can be observed for the Ag-B films relative to the Ag sample. However, the shift is inconsistent with the presumed B concentration as the Ag-B-1 exhibits a larger shift than the Ag-B-2 sample. Quantification of the oxygen concentrations revealed a large variation between the samples. The oxygen concentration at the surface of the films were 38.3, 14.6, and 25.2 at% for the Ag, Ag-B-1, and Ag-B-2, respectively. Since oxygen causes a large shift in the Ag 3d peak position, the effect of the B on the peak position cannot be determined.

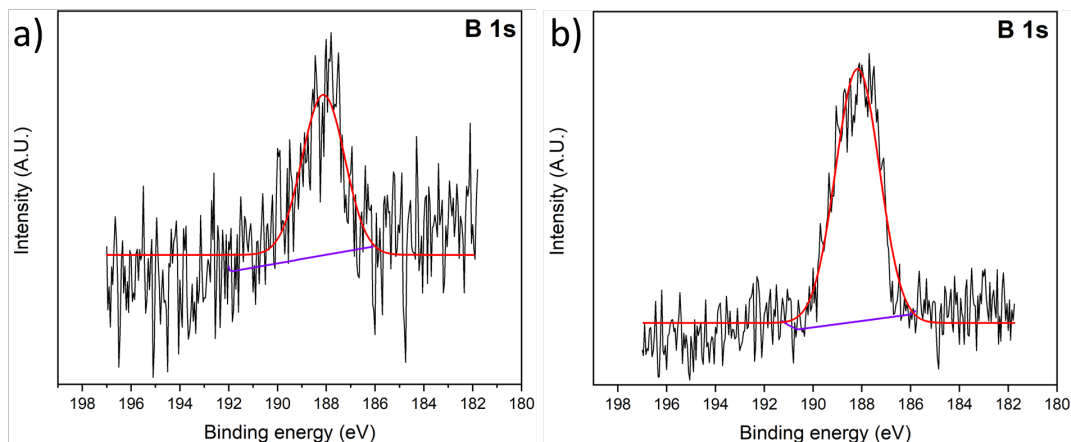


Figure 3-11 XPS measurements showing the B 1s peak for the a) Ag-B-1 and b) Ag-B-2 films.

Attempting to circumvent the oxygen induced peak shift, ion milling was employed to remove ~200 nm of the top surface layer with an Ar⁺ energy of 2 keV prior to performing XPS. However, the B1s could not be detected for any of the samples following the ion milling. AES measurements performed at two different points on the Ag-B-2 sample gave B concentrations of 28 and 25 at%. Ion milling for 6 and 18 s prior to AES reduced the concentration to 12 and 0 at%, respectively. Therefore, there are two possibilities; either the B is heavily concentrated near the top-most surface, or the ion milling preferentially removes B. Since the films are synthesized using a co-sputtering method, it is rather unlikely that the B should be concentrated near the surface. Instead, a difference in the sputtering yield would lead to removal of B during ion milling, which is more reasonable. In fact, problematic behavior with B being preferentially sputtered due to ion milling has been identified for a range of transition metal borides [68]. The effect is more pronounced at higher ion beam energies, but in our case the B1s peak remained undetectable in the XPS spectra even when reducing the ion beam energy from 2 keV to 0.5 keV.

Analysis of the gaseous reaction products revealed the formation of CO and H₂ for all the catalysts. The FE(CO) of the catalysts attained at different potentials can be seen in figure 3-12a. All catalysts displayed a high FE(CO) in the chosen potential range. Interestingly, the pristine Ag catalyst obtained an FE(CO) of 86% at -1.0 V vs. RHE. At a less negative potential the Ag-B-2 showed considerably higher FE(CO) compared to the Ag reference, reaching an FE(CO) of 69% at -0.6 V, and 79% at -0.7 V vs. RHE.

Comparatively the Ag exhibited an FE(CO) of 16% and 28% at the respective potentials, meaning that a lower potential is required to reach high FE(CO) for the Ag-B-2 catalyst. Moreover, the Ag-B-2 catalyst obtained a peak FE(CO) of 97.9% at -0.9 V vs. RHE. The partial current density for CO (J_{CO}) is also significantly larger for the Ag-B-2 at all potentials (figure 3-12b). With J_{CO} being 4 times larger than that of Ag at -0.9 V vs. RHE.

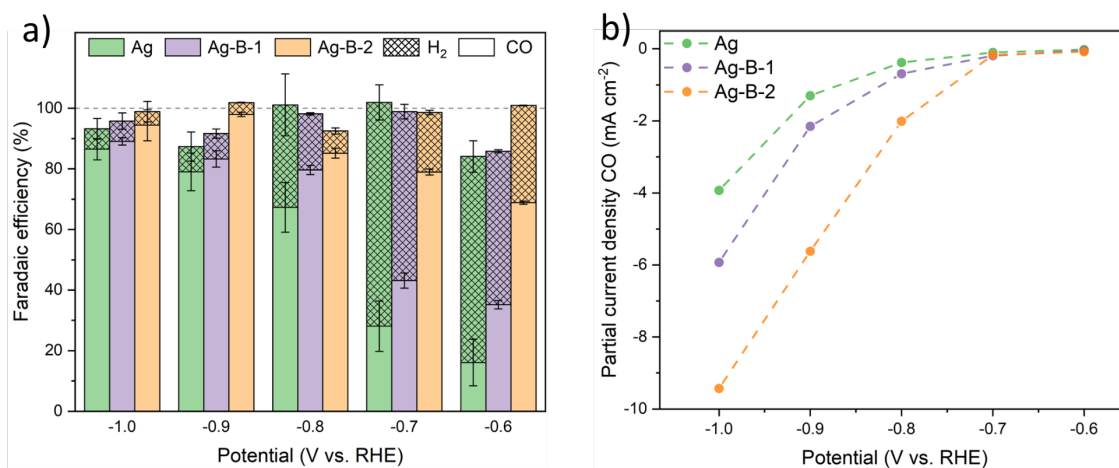


Figure 3-12 a) Faradaic efficiencies obtained for the catalysts as a function of applied potential and b) the partial current density of CO.

A 10-hour stability test was conducted for the Ag-B-2 catalyst at -0.9 V vs. RHE. Both the current density and FE(CO) over the duration of the stability test can be seen in figure 3-13. The catalyst retains a high FE(CO) ($\sim 98\%$) for the first 6 hours, with a slight decrease in FE(CO) to $\sim 90\%$ from the six-hour mark. A minor decrease was also observed for the current density. The reduction in current density was attributed to water evaporation from the electrolyte due to the continuous bubbling of CO₂ through the system, which reduced the liquid level in the cell, and thus reduced the surface area of the catalyst.

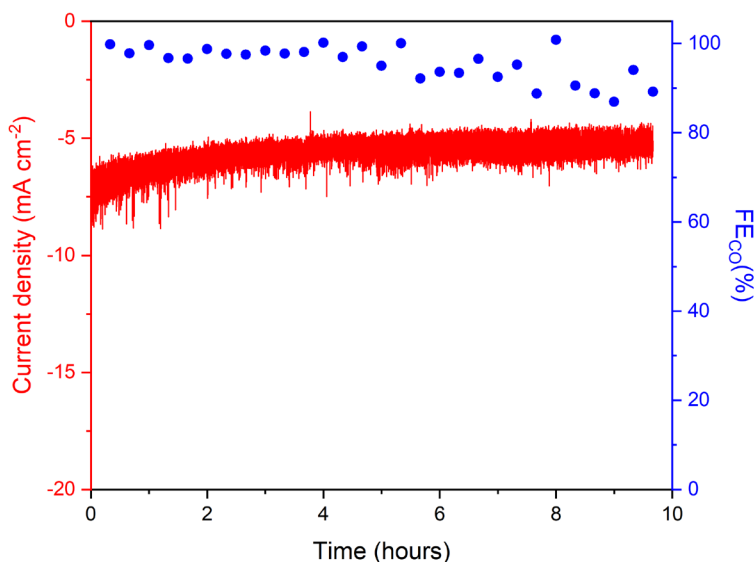


Figure 3-13 Stability test conducted for the Ag-B-2 catalyst, showing the current density and FE(CO) as a function of time.

Since the incorporation of B induced drastic changes in terms of both crystal structure and morphology, it was hard to determine the primary source for the enhanced catalytic activity. While it is well established that the Ag (111) surface exhibits the largest activation barrier compared to Ag (100) and Ag (110), the presence of the coherent twin boundaries has shown to be important active sites [69, 70]. Thus, we conducted DFT simulations to evaluate the effect on the Ag (111) coherent twin boundaries, using a model based on a single Ag (111) twin boundary as seen in figure 3-14a. Based on the free-energy profile (figure 3-14b) the *COOH remains the RDS, but the activation energy is reduced by 0.11 eV relative to the Ag (111) surface (figure 3-14b). Furthermore, the binding of CO₂ is strengthened at the twin boundary, which leads to higher catalytic activity. Contrary to the Ag-B surface, the twin boundary exhibits a stronger binding of *CO, giving the desorption a barrier of 0.16 eV. Considering the combined contributions of the B and twin boundaries, the formation of *COOH should occur more readily on the Ag-B-2 catalyst since the binding strength of *COOH is increased in both cases. Also, since an opposite effect is observed for the *CO intermediate it indicates that the combination of these effects could cancel each other, leading to a relatively unaffected *CO binding energy.

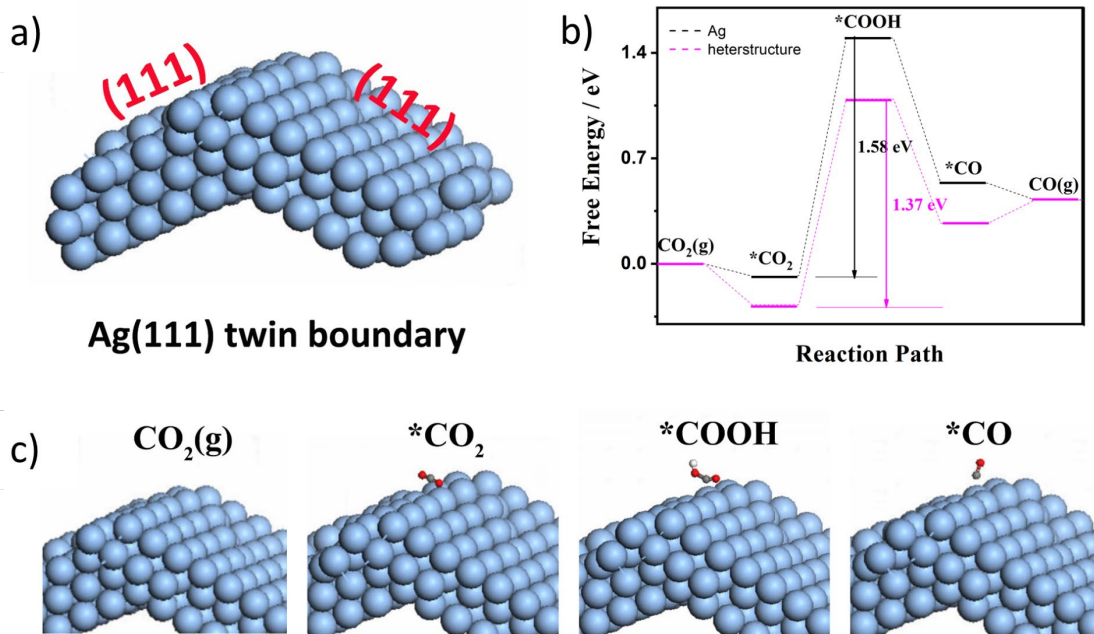


Figure 3-14 a) the twin boundary structure used in the simulations, b) the free energy diagram, and c) reaction geometries.

Conclusion

The use of B was investigated as a p-block element modifier in Ag through a combination of simulations and experiments. DFT simulations show that the introduction of B can stabilize *COOH while destabilizing the *CO intermediate, revealing a deviation from the linear scaling relations. The co-sputtering of Ag and B facilitates the growth of coherent Ag (111) twin boundaries due to a reduction in the SFE, resulting in a highly textured Ag (111) film. It is found that the unique growth mechanism gives rise to novel nano-tentacle structures. The Ag-B films show significant improvement in catalytic performance, with a FE(CO) of 97.9% attained for the Ag-B catalyst at -0.9V vs. RHE. The improved catalytic activity is attributed to the lowering of the *COOH activation barrier in combination with enhanced CO₂ adsorption at the coherent twin boundaries.

4 Conclusions and Outlook

The project work described in this thesis focused on the development of new transition metal catalysts for the electrochemical reduction of CO₂ and the design of a custom reactor setup for the precise quantification of their gaseous reaction products. This enabled the electrocatalytic performance of these catalysts to be characterized. In total three different catalyst designs were developed based on nanostructuring and light element modification that enabled enhanced catalytic properties. These catalysts included an anodized Cu catalyst, developed for the formation of C₂H₄, while two different Ag-based catalyst was synthesized, one modified with C for syngas formation with tunable H₂ to CO ratios and the other modified with B for the purpose of CO production. The main conclusions and achievements are listed below:

- A reactor setup with a continuous flow arrangement of CO₂ was successfully implemented, allowing for high accuracy detection and quantification of H₂, CO, CH₄, C₂H₄, and C₂H₆. The setup utilizes a Nafion dryer to remove water vapor from the gas stream, which enables the setup to be run for extended periods of time without the deterioration of the GC baseline. Catalysts known for exclusively producing gases in the electrochemical CO₂ reduction (Pt and Ag) were used as reference catalysts to quality check the system and to confirm that FE's close to 100% could be obtained.
- An electrochemical anodization process was developed for the synthesis of uniform large-area Cu(OH)₂ films. The process incorporates a sodium persulfate pre-treatment step of the Cu foil, which removes surface contaminations while simultaneously eliminating crevices and surface irregularities, improving the current distribution during anodization and increases the wetting of the surface. Furthermore, as a catalyst for the electrochemical CO₂ reduction the films display high geometric current densities owing to the dense nanoneedle structures with a strong preference for C₂H₄ formation over CH₄, obtaining a FE(C₂H₄) of 36.5%. The Cu(OH)₂ catalyst remains stable during reaction

conditions, making it a promising catalyst for the electrochemical CO₂ reduction to C₂H₄.

- Ag-C composite films were synthesized through co-sputtering using an Ag and C sputtering target. The introduction of C into the sputter deposition reduced the particle size in addition to the crystallite size as evident from the broadened diffraction peaks in the XRD spectrum. The change in the film morphology occurred as the co-sputtering of C disrupted the growth kinetics due to the competitive growth between the two materials. More specifically, the nucleation rate was increased, resulting in suppressed growth of Ag. The Ag-C films displayed vastly enhanced current densities, ~10-fold that of the Ag reference. By regulating the C concentration, the H₂/CO ratio could be tuned while also providing large geometric current densities. Thus, the Ag-C catalyst offers large surface areas, tunable H₂/CO ratio, and reduced silver content, rendering it a promising catalyst design for syngas applications.
- DFT simulations were conducted to evaluate B as a modifier in Ag, and its effect on the catalytic properties of Ag. It was found that the placement of B in the Ag lattice could stabilize *COOH while destabilizing the *CO intermediate, thereby breaking the scaling relations. Ag and B were co-sputtered to synthesize Ag-B films. The incorporation of B into the Ag lattice facilitates the formation of Ag (111) coherent twin boundaries due to lowering the SFE. Changes in the surface morphology are observed as it transitions from granular to novel nano-tentacle structures with the introduction of B. The Ag-B catalyst displays excellent catalytic activity, with an FE(CO) of 97.9% -0.9V vs. RHE. The unique transformation in the crystal structure combined with novel nanostructures and enhanced catalytic performance makes Ag-B a potent catalyst for the electrochemical reduction of CO₂ into CO.

- The synthesis of Ag-B films was replicated on various substrates, resulting in highly textured Ag (111) thin films. Formation of primarily Ag (111) with high deposition rates (17 nm/min) at room temperature regardless of the substrate is highly attractive for plasmonic devices due to the patterning that is necessary to manipulate the plasmonic waves. These patterns are usually created by a focused ion beam, which is an anisotropic process and therefore requires highly textured or single crystal films to achieve a satisfactory result. Thus, the following process was patented and has been included in the thesis (Norwegian Industrial Property Office, Pat. No. 347559).

Significant advancements have been made in the engineering of transition metal catalysts for the electrochemical CO₂ reduction since the pioneering work of Hori. et. al. [3]. Particularly for Cu, which arguably has been the center of attention of all the transition metals due to its unique ability to form hydrocarbons. Fundamental understanding of the C-C coupling mechanisms on Cu has aided in the development of catalysts capable of achieving high selectivity for C₂ products. The focus on minimizing the size of catalytic active sites to enhance utilization and catalytic activity has resulted in recent breakthroughs, including single-atom Cu catalysts. These stand out for their notable attributes, featuring high reaction rates and selectivity, capable of achieving ethanol FE above 90% [71]. It should be noted that the stability of these catalysts is a concern as cluster formation tends to occur during reaction conditions, but the use of nitrogen to bind and stabilize Cu single atoms using organic frameworks appears promising [72].

As for Ag, the reaction mechanisms are easier to understand and optimize since it involves a single electron transfer step. Thus, high selectivity can be obtained with Ag catalysts, but the performance is still held back by some fundamental limitations such as the linear scaling relations, which prevents lowering the overpotential. On the other hand, p-block elements have shown overcome these limitations by breaking the scaling relations. The utilization of p-block elements as modifiers for Ag is thus a potential source for further development of Ag-based catalysts that should be explored further.

For direct electrochemical syngas formation, Ag remains the most viable choice but suffers from low activity compared to the other group 2 transition metals, and nanostructuring and the use of C-based supports are therefore required. This complicates the synthesis of the catalyst, making it intricate and challenging to scale up. However, the sputter technology presented in this thesis exhibits the scale-up potential to address and potentially overcome this challenge.

Despite achieving high FE's for specific products, such as in the case of Ag, the industrial demand for current density (200-500 mA/cm² for CO and greater than 200 mA/cm² for syngas) requires the exploration of alternative reactor designs. [73, 74]. The H-cell, which is described in this work is useful for screening catalysts, however, the cell design suffers from mass transfer limitations caused by the low solubility of CO₂ in aqueous electrolyte, limiting the reaction rates to <100 mA/cm². To overcome these constraints, there has been a heightened emphasis on various types of flow electrolyzers. Specifically, the utilization of gas diffusion layers (GDL) for creating gas diffusion electrodes (GDE) has gained significance. In this configuration, the catalyst is applied to a GDL, and the CO₂ is introduced in the gaseous phase, diffusing through the porous GDL layer to reach the triple-phase interface comprised of the catalyst, CO₂ gas, and electrolyte. Consequently, the solubility concern is alleviated, enabling the system to achieve current densities relevant to industrial applications. The flow-reactor also allows for larger versatility in terms of electrolyte choice, as it opens for the possibility of using alkaline electrolytes like KOH where CO₂ would normally react to form bicarbonates. Cu has shown enhanced performance in these types of alkaline electrolytes as it promotes CO-CO coupling while suppressing the HER [75]. Nevertheless, challenges persist with these reactor cell designs. An essential characteristic of the GDL is its hydrophobic nature, acting as a preventive measure against the flooding phenomenon. Flooding occurs when the liquid electrolyte infiltrates the GDL, leading to obstructions in the porous CO₂ pathways and potential permanent blockages due to salt precipitation. This often results in a substantial increase in the HER and typically manifests a few hours into the reaction. Some studies have indicated a relation between flooding and the applied potential due to the electrochemical activity of the carbon [76], which would further

incentivize the development of catalyst able to provide high selectivity at low overpotentials. Thus, the flow-cell surpasses numerous fundamental limitations of the traditional H-cell, exhibiting high mass transfer efficiency. However, the technology related to these designs is still in its early stages of development for CO₂RR, necessitating further research to optimize the membrane, GDL, anode, and electrolyte.

An aspect that requires consideration is the origin of the CO₂. Presently, most reactor designs utilize a pure CO₂ feed, which can be expensive and often impractical for many potential applications. For example, CO₂ feeds from chemical or power plants may contain impurities such as SO_x, NO_x, O₂, etc., which have the potential to influence the catalytic properties of the electrode [77]. The presence of SO₂ impurities in these CO₂ feeds adversely affects the efficiency and selectivity of the catalyst for CO₂ reduction. [78]. Therefore, it is recommended to expose catalysts to impure and diluted streams of CO₂ in the future, ensuring that product selectivity and catalytic activity can be maintained under such conditions. Another promising avenue for research is pulsed electrocatalytic CO₂ reduction, involving the application of potential using differently shaped pulses to manipulate the local electrolytic environment. Optimizing pulse shape, potential, and frequency has demonstrated a significant impact on both product selectivity and long-term stability [79]. Pulsed electrocatalysis is versatile in terms of reactors, making it compatible with both H-cell and flow cell designs, and is an area that warrants further investigation.

References

1. Lu, Q. and F. Jiao, *Electrochemical CO₂ reduction: Electrocatalyst, reaction mechanism, and process engineering*. Nano Energy, 2016. **29**: p. 439-456.
2. Zhao, X., et al., *Integrated design for electrocatalytic carbon dioxide reduction*. Catalysis Science & Technology, 2020. **10**(9): p. 2711-2720.
3. Hori, Y., et al., *Electrocatalytic process of CO selectivity in electrochemical reduction of CO₂ at metal electrodes in aqueous media*. Electrochimica Acta, 1994. **39**(11): p. 1833-1839.
4. Komatsu, S., et al., *Electrochemical Reduction of CO₂ at Sb and Bi Electrodes in KHCO₃ Solution*. Denki Kagaku Oyobi Kogyo Butsuri Kagaku, 1995. **63**(3): p. 217-224.
5. Cheng, T., H. Xiao, and W.A. Goddard, *Reaction Mechanisms for the Electrochemical Reduction of CO₂ to CO and Formate on the Cu(100) Surface at 298 K from Quantum Mechanics Free Energy Calculations with Explicit Water*. Journal of the American Chemical Society, 2016. **138**(42): p. 13802-13805.
6. Chernyshova, I.V., P. Somasundaran, and S. Ponnurangam, *On the origin of the elusive first intermediate of CO₂ electroreduction*. Proceedings of the National Academy of Sciences, 2018. **115**(40): p. E9261.
7. Cook, R.L., R.C. MacDuff, and A.F. Sammells, *Evidence for Formaldehyde, Formic Acid, and Acetaldehyde as Possible Intermediates during Electrochemical Carbon Dioxide Reduction at Copper*. Journal of The Electrochemical Society, 1989. **136**(7): p. 1982-1984.
8. Hori, Y., A. Murata, and R. Takahashi, *Formation of hydrocarbons in the electrochemical reduction of carbon dioxide at a copper electrode in aqueous solution*. Journal of the Chemical Society, Faraday Transactions 1: Physical Chemistry in Condensed Phases, 1989. **85**(8): p. 2309-2326.
9. Peterson, A.A., et al., *How copper catalyzes the electroreduction of carbon dioxide into hydrocarbon fuels*. Energy & Environmental Science, 2010. **3**(9): p. 1311-1315.
10. Gustavsen, K.R. and K. Wang, *Recent advances on enhancing the multicarbon selectivity of nanostructured Cu-based catalysts*. Physical Chemistry Chemical Physics, 2021. **23**(22): p. 12514-12532.
11. Montoya, J.H., A.A. Peterson, and J.K. Nørskov, *Insights into C₂C Coupling in CO₂ Electroreduction on Copper Electrodes*. ChemCatChem, 2013. **5**(3): p. 737-742.
12. Kuhl, K.P., et al., *New insights into the electrochemical reduction of carbon dioxide on metallic copper surfaces*. Energy & Environmental Science, 2012. **5**(5): p. 7050-7059.
13. Resasco, J., et al., *Promoter Effects of Alkali Metal Cations on the Electrochemical Reduction of Carbon Dioxide*. Journal of the American Chemical Society, 2017. **139**(32): p. 11277-11287.
14. Schouten, K.J.P., et al., *A new mechanism for the selectivity to C₁ and C₂ species in the electrochemical reduction of carbon dioxide on copper electrodes*. Chemical Science, 2011. **2**(10): p. 1902-1909.

15. Montoya, J.H., et al., *Theoretical Insights into a CO Dimerization Mechanism in CO₂ Electroreduction*. The Journal of Physical Chemistry Letters, 2015. **6**(11): p. 2032-2037.
16. Garza, A.J., A.T. Bell, and M. Head-Gordon, *Mechanism of CO₂ Reduction at Copper Surfaces: Pathways to C₂ Products*. ACS Catalysis, 2018. **8**(2): p. 1490-1499.
17. Xiao, H., T. Cheng, and W.A. Goddard, *Atomistic Mechanisms Underlying Selectivities in C₁ and C₂ Products from Electrochemical Reduction of CO on Cu(111)*. Journal of the American Chemical Society, 2017. **139**(1): p. 130-136.
18. Cheng, T., H. Xiao, and W.A. Goddard, *Full atomistic reaction mechanism with kinetics for CO reduction on Cu(100) from ab initio molecular dynamics free-energy calculations at 298 K*. Proceedings of the National Academy of Sciences, 2017. **114**(8): p. 1795.
19. Luo, W., et al., *Facet Dependence of CO₂ Reduction Paths on Cu Electrodes*. ACS Catalysis, 2016. **6**(1): p. 219-229.
20. Calle-Vallejo, F. and M.T.M. Koper, *Theoretical Considerations on the Electroreduction of CO to C₂ Species on Cu(100) Electrodes*. Angewandte Chemie International Edition, 2013. **52**(28): p. 7282-7285.
21. Hanselman, S., M.T.M. Koper, and F. Calle-Vallejo, *Computational Comparison of Late Transition Metal (100) Surfaces for the Electrocatalytic Reduction of CO to C₂ Species*. ACS Energy Letters, 2018. **3**(5): p. 1062-1067.
22. Todorova, T.K., M.W. Schreiber, and M. Fontecave, *Mechanistic Understanding of CO₂ Reduction Reaction (CO₂RR) Toward Multicarbon Products by Heterogeneous Copper-Based Catalysts*. ACS Catalysis, 2020. **10**(3): p. 1754-1768.
23. Hori, Y., et al., *Electrochemical reduction of carbon dioxide at various series of copper single crystal electrodes*. Journal of Molecular Catalysis A: Chemical, 2003. **199**(1): p. 39-47.
24. Roberts, F.S., K.P. Kuhl, and A. Nilsson, *Electroreduction of Carbon Monoxide Over a Copper Nanocube Catalyst: Surface Structure and pH Dependence on Selectivity*. ChemCatChem, 2016. **8**(6): p. 1119-1124.
25. Mangione, G., et al., *Dual-Facet Mechanism in Copper Nanocubes for Electrochemical CO₂ Reduction into Ethylene*. The Journal of Physical Chemistry Letters, 2019. **10**(15): p. 4259-4265.
26. Loiudice, A., et al., *Tailoring Copper Nanocrystals towards C₂ Products in Electrochemical CO₂ Reduction*. Angewandte Chemie, 2016. **128**(19): p. 5883-5886.
27. Dutta, A., et al., *Activation of bimetallic AgCu foam electrocatalysts for ethanol formation from CO₂ by selective Cu oxidation/reduction*. Nano Energy, 2020. **68**: p. 104331.
28. Lum, Y. and J.W. Ager, *Sequential catalysis controls selectivity in electrochemical CO₂ reduction on Cu*. Energy & Environmental Science, 2018. **11**(10): p. 2935-2944.
29. Mistry, H., et al., *Highly selective plasma-activated copper catalysts for carbon dioxide reduction to ethylene*. Nature Communications, 2016. **7**(1): p. 12123.

30. Gao, D., et al., *Plasma-Activated Copper Nanocube Catalysts for Efficient Carbon Dioxide Electroreduction to Hydrocarbons and Alcohols*. ACS Nano, 2017. **11**(5): p. 4825-4831.
31. Eilert, A., et al., *Subsurface Oxygen in Oxide-Derived Copper Electrocatalysts for Carbon Dioxide Reduction*. The Journal of Physical Chemistry Letters, 2017. **8**(1): p. 285-290.
32. Cavalca, F., et al., *Nature and Distribution of Stable Subsurface Oxygen in Copper Electrodes During Electrochemical CO₂ Reduction*. The Journal of Physical Chemistry C, 2017. **121**(45): p. 25003-25009.
33. Xiao, H., et al., *Cu metal embedded in oxidized matrix catalyst to promote CO₂ activation and CO dimerization for electrochemical reduction of CO₂*. Proceedings of the National Academy of Sciences, 2017. **114**(26): p. 6685.
34. Zhou, Y., et al., *Dopant-induced electron localization drives CO₂ reduction to C₂ hydrocarbons*. Nature Chemistry, 2018. **10**(9): p. 974-980.
35. Zhuang, T.-T., et al., *Steering post-C-C coupling selectivity enables high efficiency electroreduction of carbon dioxide to multi-carbon alcohols*. Nature Catalysis, 2018. **1**(6): p. 421-428.
36. Ma, W., et al., *Electrocatalytic reduction of CO₂ to ethylene and ethanol through hydrogen-assisted C-C coupling over fluorine-modified copper*. Nature Catalysis, 2020.
37. Hoshi, N., M. Kato, and Y. Hori, *Electrochemical reduction of CO₂ on single crystal electrodes of silver Ag(111), Ag(100) and Ag(110)*. Journal of Electroanalytical Chemistry, 1997. **440**(1): p. 283-286.
38. Back, S., M.S. Yeom, and Y. Jung, *Active Sites of Au and Ag Nanoparticle Catalysts for CO₂ Electroreduction to CO*. ACS Catalysis, 2015. **5**(9): p. 5089-5096.
39. Hatsukade, T., et al., *Insights into the electrocatalytic reduction of CO₂ on metallic silver surfaces*. Physical Chemistry Chemical Physics, 2014. **16**(27): p. 13814-13819.
40. Rosen, J., et al., *Mechanistic Insights into the Electrochemical Reduction of CO₂ to CO on Nanostructured Ag Surfaces*. ACS Catalysis, 2015. **5**(7): p. 4293-4299.
41. Sun, Y. and Y. Xia, *Shape-Controlled Synthesis of Gold and Silver Nanoparticles*. Science, 2002. **298**(5601): p. 2176-2179.
42. Salehi-Khojin, A., et al., *Nanoparticle Silver Catalysts That Show Enhanced Activity for Carbon Dioxide Electrolysis*. The Journal of Physical Chemistry C, 2013. **117**(4): p. 1627-1632.
43. Xi, W., et al., *Ultrathin Ag Nanowires Electrode for Electrochemical Syngas Production from Carbon Dioxide*. ACS Sustainable Chemistry & Engineering, 2018. **6**(6): p. 7687-7694.
44. Hsieh, Y.-C., et al., *Effect of Chloride Anions on the Synthesis and Enhanced Catalytic Activity of Silver Nanocoral Electrodes for CO₂ Electroreduction*. ACS Catalysis, 2015. **5**(9): p. 5349-5356.
45. Ham, Y.S., et al., *Electrodeposited Ag catalysts for the electrochemical reduction of CO₂ to CO*. Applied Catalysis B: Environmental, 2017. **208**: p. 35-43.

46. Liu, S., et al., *Shape-Dependent Electrocatalytic Reduction of CO₂ to CO on Triangular Silver Nanoplates*. Journal of the American Chemical Society, 2017. **139**(6): p. 2160-2163.
47. Yang, M., et al., *Facet Sensitivity of Capping Ligand-Free Ag Crystals in CO₂ Electrochemical Reduction to CO*. ChemCatChem, 2018. **10**(22): p. 5128-5134.
48. Choi, J., et al., *Electrochemical CO₂ reduction to CO on dendritic Ag–Cu electrocatalysts prepared by electrodeposition*. Chemical Engineering Journal, 2016. **299**: p. 37-44.
49. Hatsukade, T., et al., *Carbon Dioxide Electroreduction using a Silver–Zinc Alloy*. Energy Technology, 2017. **5**(6): p. 955-961.
50. Luc, W., et al., *Ag–Sn Bimetallic Catalyst with a Core–Shell Structure for CO₂ Reduction*. Journal of the American Chemical Society, 2017. **139**(5): p. 1885-1893.
51. Park, H., et al., *AgIn dendrite catalysts for electrochemical reduction of CO₂ to CO*. Applied Catalysis B: Environmental, 2017. **219**: p. 123-131.
52. Lim, H.-K., et al., *Embedding Covalency into Metal Catalysts for Efficient Electrochemical Conversion of CO₂*. Journal of the American Chemical Society, 2014. **136**(32): p. 11355-11361.
53. Liu, S., et al., *Rational Design of Silver Sulfide Nanowires for Efficient CO₂ Electroreduction in Ionic Liquid*. ACS Catalysis, 2018. **8**(2): p. 1469-1475.
54. Pal, D.B., et al., *Performance of water gas shift reaction catalysts: A review*. Renewable and Sustainable Energy Reviews, 2018. **93**: p. 549-565.
55. Hong, J., et al., *Ag/C composite catalysts derived from spray pyrolysis for efficient electrochemical CO₂ reduction*. Chemical Engineering Journal, 2022. **431**: p. 133384.
56. Sastre, F., et al., *Efficient Electrochemical Production of Syngas from CO₂ and H₂O by using a Nanostructured Ag/g-C₃N₄ Catalyst*. ChemElectroChem, 2016. **3**(9): p. 1497-1502.
57. Cho, M., et al., *Silver Nanowire/Carbon Sheet Composites for Electrochemical Syngas Generation with Tunable H₂/CO Ratios*. ACS Omega, 2017. **2**(7): p. 3441-3446.
58. Iijima, G., et al., *Role of a Hydroxide Layer on Cu Electrodes in Electrochemical CO₂ Reduction*. ACS Catalysis, 2019. **9**(7): p. 6305-6319.
59. Xiao, F., et al., *Superhydrophobic CuO nanoneedle-covered copper surfaces for anticorrosion*. Journal of Materials Chemistry A, 2015. **3**(8): p. 4374-4388.
60. Babu, T.G.S. and T. Ramachandran, *Development of highly sensitive non-enzymatic sensor for the selective determination of glucose and fabrication of a working model*. Electrochimica Acta, 2010. **55**(5): p. 1612-1618.
61. Shooshtari, L., R. Mohammadpour, and A.I. Zad, *Enhanced photoelectrochemical processes by interface engineering, using Cu₂O nanorods*. Materials Letters, 2016. **163**: p. 81-84.
62. Stepniowski, W.J., et al., *Morphology and photoluminescence of nanostructured oxides grown by copper passivation in aqueous potassium hydroxide solution*. Materials Letters, 2017. **198**: p. 89-92.

63. M. Awwad, A. and B. Albiss, *Biosynthesis Of Colloidal Copper Hydroxide Nanowires Using Pistachio Leaf Extract*. *Advanced Materials Letters*, 2015. **6**(1): p. 51-54.
64. Henrist, C., et al., *Study of the morphology of copper hydroxynitrate nanoplatelets obtained by controlled double jet precipitation and urea hydrolysis*. *Journal of Crystal Growth*, 2003. **254**(1): p. 176-187.
65. Chen, C., et al., *Efficient electroreduction of CO₂ to C₂ products over B-doped oxide-derived copper*. *Green Chemistry*, 2018. **20**(20): p. 4579-4583.
66. Bufford, D., H. Wang, and X. Zhang, *High strength, epitaxial nanotwinned Ag films*. *Acta Materialia*, 2011. **59**(1): p. 93-101.
67. Velasco, L. and A.M. Hodge, *The mobility of growth twins synthesized by sputtering: Tailoring the twin thickness*. *Acta Materialia*, 2016. **109**: p. 142-150.
68. Greczynski, G. and L. Hultman, *Towards reliable X-ray photoelectron spectroscopy: Sputter-damage effects in transition metal borides, carbides, nitrides, and oxides*. *Applied Surface Science*, 2021. **542**: p. 148599.
69. Tang, C., et al., *Direct electrosynthesis of 52% concentrated CO on silver's twin boundary*. *Nature Communications*, 2021. **12**(1): p. 2139.
70. Tang, C., et al., *CO₂ Reduction on Copper's Twin Boundary*. *ACS Catalysis*, 2020. **10**(3): p. 2026-2032.
71. Xu, H., et al., *Highly selective electrocatalytic CO₂ reduction to ethanol by metallic clusters dynamically formed from atomically dispersed copper*. *Nature Energy*, 2020. **5**(8): p. 623-632.
72. Xia, W., et al., *Adjacent Copper Single Atoms Promote C–C Coupling in Electrochemical CO₂ Reduction for the Efficient Conversion of Ethanol*. *Journal of the American Chemical Society*, 2023. **145**(31): p. 17253-17264.
73. Masel, R.I., et al., *An industrial perspective on catalysts for low-temperature CO₂ electrolysis*. *Nature Nanotechnology*, 2021. **16**(2): p. 118-128.
74. Debergh, P., et al., *The Economics of Electrochemical Syngas Production via Direct Air Capture*. *ACS Energy Letters*, 2023. **8**(8): p. 3398-3403.
75. Wang, L., et al., *Electrochemical Carbon Monoxide Reduction on Polycrystalline Copper: Effects of Potential, Pressure, and pH on Selectivity toward Multicarbon and Oxygenated Products*. *ACS Catalysis*, 2018. **8**(8): p. 7445-7454.
76. Yang, K., et al., *Role of the Carbon-Based Gas Diffusion Layer on Flooding in a Gas Diffusion Electrode Cell for Electrochemical CO₂ Reduction*. *ACS Energy Letters*, 2021. **6**(1): p. 33-40.
77. Last, G.V. and M.T. Schmick, *Identification and Selection of Major Carbon Dioxide Stream Compositions*. 2011: United States.
78. Luc, W., et al., *SO₂-Induced Selectivity Change in CO₂ Electroreduction*. *Journal of the American Chemical Society*, 2019. **141**(25): p. 9902-9909.
79. Masaud, Z., et al., *Progress on pulsed electrocatalysis for sustainable energy and environmental applications*. *Chemical Engineering Journal*, 2023. **475**: p. 145882.

Article 1

Gustavsen, K.R, and Wang, K. (2021). Recent Advances on Enhancing the Multicarbon Selectivity of Nanostructured Cu-based Catalysts. *Physical Chemistry Chemical Physics*, 38(4), 407-416. doi: 10.1080/02602938.2011.638738

Article 1 is omitted from online publication due to publisher's restrictions

Article 2

Gustavsen, K.R, Johannessen E.A, and Wang, K. (2022). Sodium Persulfate Pre-treatment of Copper Foils Enabling Homogenous Growth of $\text{Cu}(\text{OH})_2$ Films for Electrochemical CO_2 Reduction. *ChemistryOpen*, 11(10), e202200133. doi: 10.1002/open.202200133

Sodium Persulfate Pre-treatment of Copper Foils Enabling Homogenous Growth of $\text{Cu}(\text{OH})_2$ Nanoneedle Films for Electrochemical CO_2 Reduction

Kim Robert Gustavsen, Erik Andrew Johannessen, and Kaiying Wang^{*[a]}

Oxide-derived copper (OD–Cu) catalysts have received widespread attention for their ability to produce energy-dense multicarbon products. Within this class of materials, nanostructured copper hydroxide ($\text{Cu}(\text{OH})_2$) has shown excellent catalytic properties, but its synthesis requires complex pre-treatment steps of the Cu surface. In this study, we have developed a simple two-step synthesis method for homogenous $\text{Cu}(\text{OH})_2$ nanoneedle films using a sodium persulfate pre-treatment step prior to anodization. The $\text{Cu}(\text{OH})_2$ nanoneedle

films show drastically enhanced uniformity after the pre-treatment due to improved current distribution and can be grown over large surface areas (63 cm^2). As a catalyst for CO_2 reduction, the $\text{Cu}(\text{OH})_2$ favours ethylene formation, with a near total suppression of methane production. A peak faradaic efficiency (FE) of 36.5% is found at -1.0 V vs. the reversible hydrogen electrode (RHE), and the catalyst remains stable while providing an ethylene to methane ratio of 27.8 after 6 h of reaction.

Introduction


The electrochemical reduction of CO_2 into higher order organic chemicals and fuels has shown to be a potent green methodology to help reducing our dependence on fossilized fuels. Copper (Cu) has in this respect been extensively investigated in search for a suitable catalyst due to its intrinsic ability to form energy-dense hydrocarbons. The modification of Cu into oxygen-derived Cu (OD–Cu) catalysts has emerged as a prime candidate as it facilitates carbon-carbon (C–C) coupling, leading to significantly higher selectivity for ethylene (C_2H_4) production.^[1] Numerous mechanisms for this enhanced selectivity have been proposed, such as the existence of sub-surface oxides during reaction conditions as well as increased local pH induced by the larger surface roughness on the reduced Cu surface. However, there has been no clear consensus on the exact cause for the improved catalytic activity. The emergence of OD–Cu triggered an incentive to identify in what way the method of oxide growth affects the catalytic properties of Cu. A prime example is the anodization of Cu foils to yield copper hydroxide ($\text{Cu}(\text{OH})_2$) films with high-aspect-ratio nanoneedle structures. These $\text{Cu}(\text{OH})_2$ nanoneedles shows greater affinity towards the generation of C_2H_4 at the expense of methane (CH_4), with stable performance for more than 40 h.^[2] Recent studies also suggest that local electric fields induced by the

unique nanoneedle morphology play a key role in promoting the C–C coupling.^[3]

While the effect of anodization parameters on the $\text{Cu}(\text{OH})_2$ film morphology and properties have been extensively studied, the initial condition of the Cu foil surface itself is crucial for achieving a satisfactory film quality. Factors such as surface irregularities and wettability can result in poor current distribution during the anodization process. This may lead to an uneven nanoneedle film in terms of thickness and morphology, which in turn can have detrimental effect on the CO_2 reduction reaction (CO_2RR) selectivity. Thus, extensive surface treatment procedures have been applied to address these issues, such as mechanical polishing with emery papers^[4] or alumina powders,^[5] chemical polishing with HNO_3 ,^[6] electrochemical polishing,^[7] and chemical treatment using HCl to remove surface oxides.^[4a,8] Often, a rather complicated process including a combination of polishing and chemical treatment steps must be used to obtain a film quality that is satisfactorily uniform.^[4a,7]

In this paper, we report a two-step synthesis method for large area $\text{Cu}(\text{OH})_2$ nanoneedle films using a simple sodium persulfate pre-treatment step that increases the wettability of the Cu foils. The sodium persulfate removes crevices and surface contaminants such as carbon and oxygen which in turn reduces the formation of defects such as pinholes. A cleaner surface will permit the current distribution to become more uniform in the subsequent anodization step, allowing the formation of homogenous $\text{Cu}(\text{OH})_2$ nanoneedle films over a large surface area (63 cm^2). Moreover, investigation of the catalytic properties of the $\text{Cu}(\text{OH})_2$ nanoneedle films reveals a strong preference for C_2H_4 production over CH_4 , with a substantial increase in current density and catalytic stability compared to the pristine Cu foil catalyst.

[a] K. R. Gustavsen, Prof. Dr. E. A. Johannessen, Prof. Dr. K. Wang
Department of Microsystems
University of South-Eastern Norway
Raveien 205
3184 Horten, (Norway)
E-mail: kaiying.wang@usn.no

 © 2022 The Authors. Published by Wiley-VCH GmbH. This is an open access article under the terms of the Creative Commons Attribution Non-Commercial License, which permits use, distribution and reproduction in any medium, provided the original work is properly cited and is not used for commercial purposes.

Results and Discussion

An illustration of the anodization process and the experimental setup used subsequently for the electrochemical CO_2 reduction and quantification of the gaseous reaction products is explained in detail in the Experimental Section. Figure 1a shows the result of the anodization with and without the pre-treatment step. Upon pre-treating the Cu foil with sodium persulfate, the surface becomes brighter in colour. Furthermore, contact angle measurements with water show that the hydro-

philic properties of the surface increases from 80° for the pristine Cu foil to 14° following the pre-treatment, indicating an increase in surface energy.^[9]

Subsequent measurement repeated for the treated Cu following exposure to ambient air shows that the contact angle gradually increased to 72° after 6 h, suggesting that the surface energy was returning to its original level due to reoxidation. An SEM image of the pristine Cu foil in Figure 2a shows a significant number of crevices of roughly $10\ \mu\text{m}$ in width. After pre-treatment, most of the crevices have been eliminated while adding a surface roughness at a lower-hierarchy level (Fig-

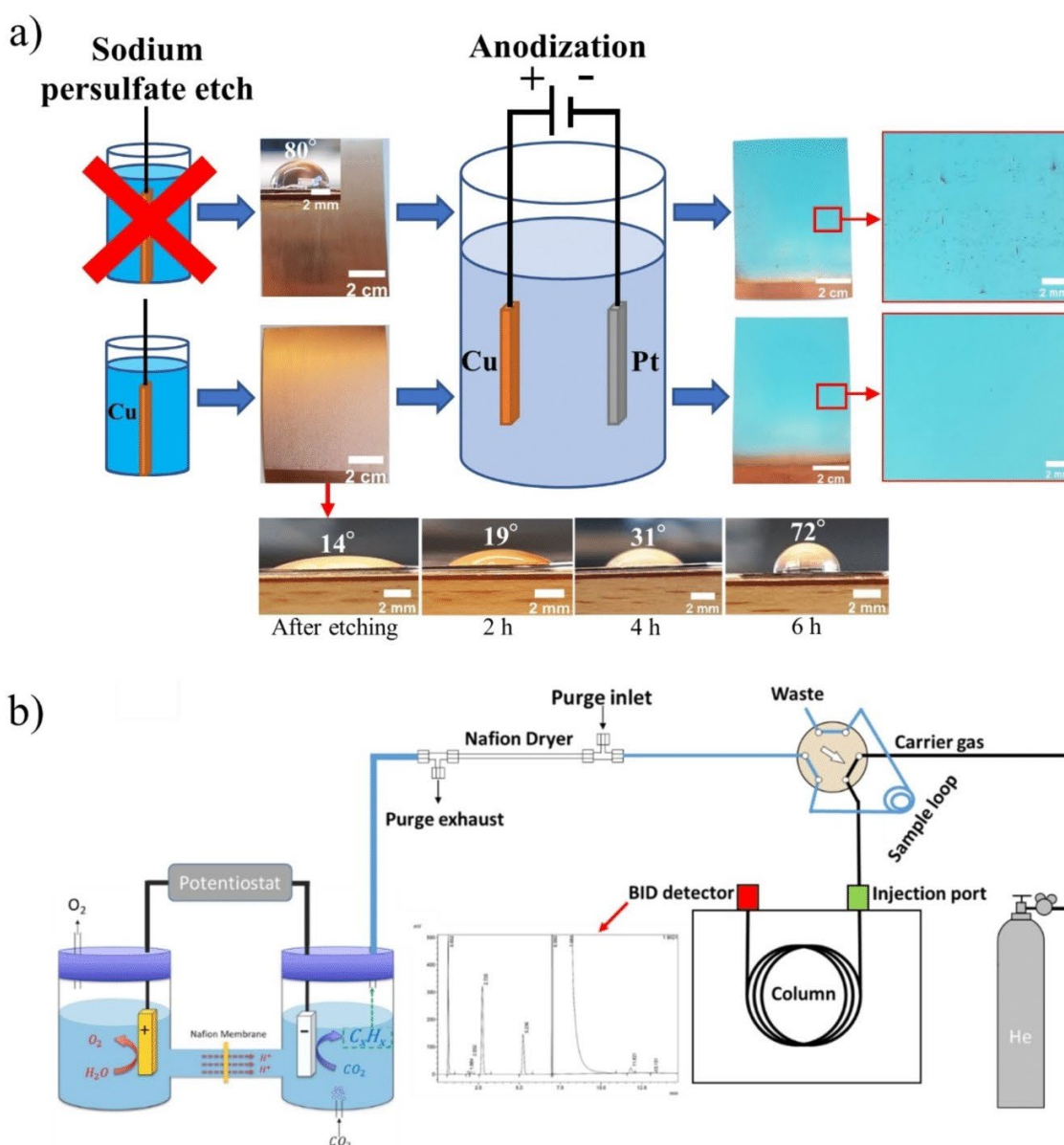


Figure 1. a) The process flow illustrating the development of the $\text{Cu}(\text{OH})_2$ nanoneedle films and b) schematic of the setup used for the electrochemical measurements and gas quantification.

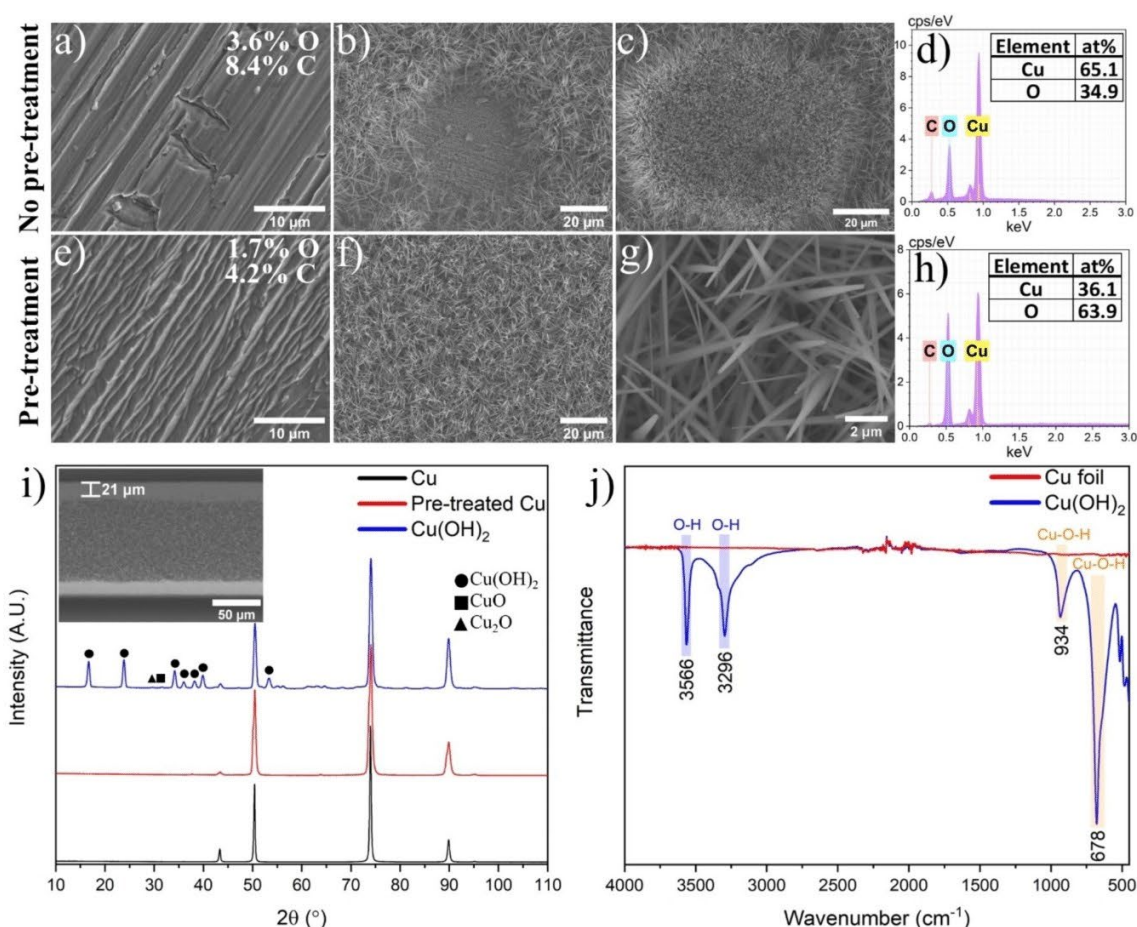


Figure 2. SEM images of a) the pristine Cu foil, b) pinhole and c) patch with reduced growth on the anodized surface, and d) EDX spectrum of the layer inside the pinhole observed in c). SEM images of the e) Cu foil after pre-treatment, f)–g) pre-treated Cu sample after anodization, and h) EDX spectrum of the nanoneedles in Figure g). i) XRD spectra of the Cu foil before and after pre-treatment as well as the Cu(OH)₂ film. j) FTIR spectra of the pristine Cu foil and Cu(OH)₂ film.

ure 2e) that increased the effective surface area. Energy Dispersive X-Ray Analysis (EDX) performed before and after pre-treatment shows a reduction in both oxygen and carbon content from 3.6% and 8.4% to 1.7% and 4.2%, respectively.

Anodization of the Cu foils results in a light-blue film as observed in Figure 1a. However, a significant amount of surface defect in form of “black” spots are found when anodizing the pristine Cu foil. On the other hand, anodization of the pre-treated Cu foil leads to a smooth and uniform surface without noticeable surface defects. Further investigation of the black spots in the SEM reveals the growth of nanoneedles surrounding empty areas of 30–50 μm in size as shown in Figure 2b.

The EDX analysis confirms the formation of Cu₂O layers in these areas (Figure 2d). There are also several patches where the density, shape, and size of nanoneedles vary drastically, indicating a variation in nucleation rate (Figure 2c). In contrast, anodization following the pre-treatment (etching) with sodium persulfate results in a high and even density of nanoneedles

across the whole surface area (Figure 2f). The nanoneedles have an average width close to the needle tip of ~200 nm (Figure 2g), and the film thickness is ~21 μm (Figure 2i, inset). Moreover, EDX measurements of the nanoneedles show an oxygen concentration of 64.5%, roughly a 2:1 ratio of oxygen to copper (Figure 2h). Overall, the pre-treatment leads to a vastly improved uniformity compared to the direct anodization of the pristine sample. Since the surface energy has been reduced back to approximately that of the pristine Cu sample after 6 h, it indicates that it is primarily the removal of carbon and the native oxide layer from the surface rather than an increase in surface area that is responsible for the initial increase in surface energy.

To evaluate the defect mechanism, we first considered the side reactions during anodization. There are two main competing side reactions to the formation of Cu(OH)₂, namely the formation of CuO through the dehydration of Cu(OH)₂^[10] and the oxidation of Cu to form Cu₂O.^[11] As the dehydration of

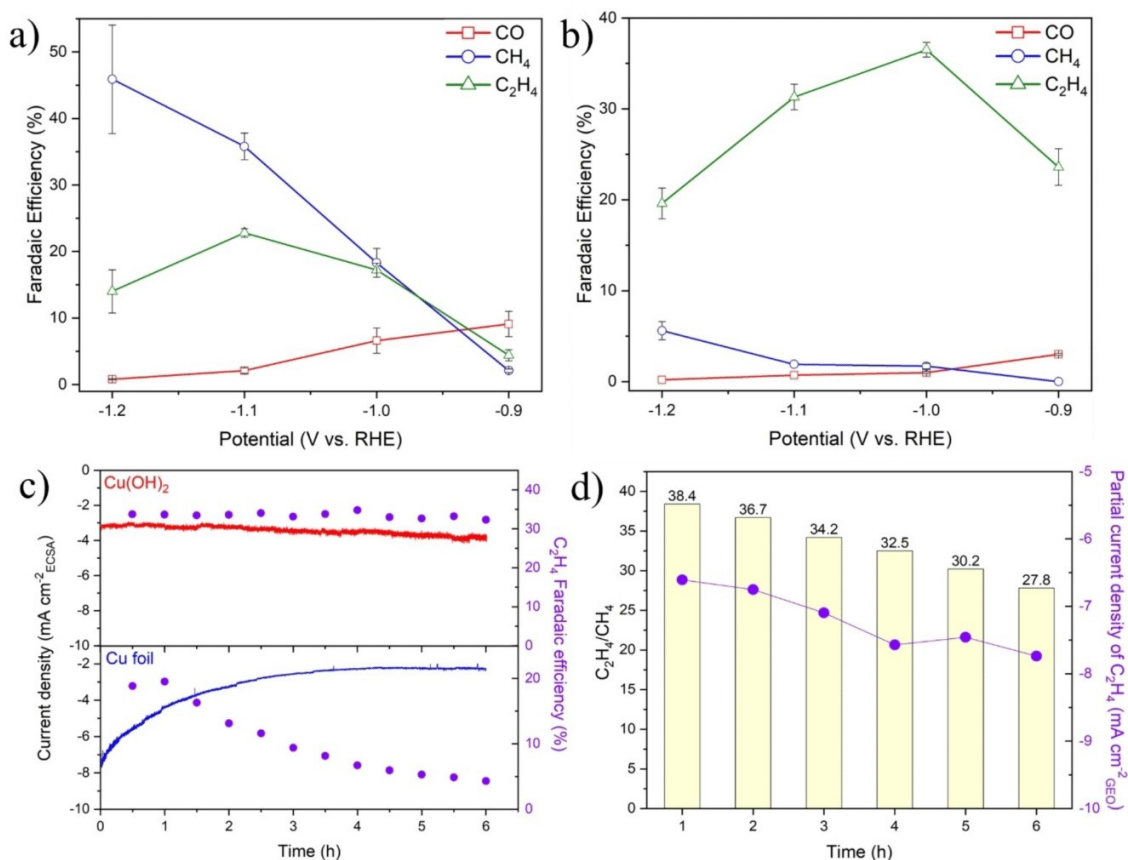
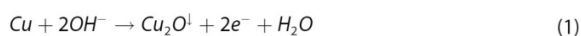


Figure 3. Electrochemical characterization: a) selectivity of the Cu foil catalyst, b) selectivity of the Cu(OH)₂ catalyst, c) stability test, and d) the C₂H₄ to CH₄ production ratio including the partial current density from C₂H₄ production obtained for the Cu(OH)₂ catalyst during the stability test.

Cu(OH)₂ is a purely chemical reaction, it is more pronounced at higher temperature and KOH concentration. On the other hand, the formation of Cu₂O arises from the side reaction given in Equation (1).



In general, the formation of both CuO and Cu₂O can be circumvented by increasing the current density (> 1.0 mA cm⁻²) as they are more favourable at lower current densities.^[10] In our case, an applied current density of 1.6 mA cm⁻² should be sufficient to avoid these parasitic reactions. While the cracks and crevices will negatively impact the current distribution, they will not result in the type of defects observed in Figures 2b–c, as the sharp edges in these surface irregularities would attract a higher current density, inducing rapid growth of Cu(OH)₂. Thus, the pinholes occur due to the presence of surface contaminants partially or fully blocking the growth of Cu(OH)₂. Consequently, there will be areas without growth as shown in Figure 2b, or with a reduction in growth rate as shown in Figure 2c.

The empty sites consist of a Cu₂O layer, that, according to the EDX measurements, is significantly thicker (~10-fold) than the native oxide layer found on the pristine Cu. Areas with thicker oxide layers on the pristine Cu surface would effectively block or reduce the current at that site during anodization. While a partial blockage can result in a reduced growth rate of the Cu(OH)₂ as shown in Figure 2c, it can also favour side reactions if the current density is reduced sufficiently.

The structure of the Cu(OH)₂ nanoneedle films was analysed by X-ray diffraction (XRD) and Fourier-transform infrared spectroscopy (FTIR). The acquired XRD spectra (Figure 2i) show strong peaks indicative of the orthorhombic copper hydroxide phase with small diffraction peaks associated with Cu₂O and CuO. The FTIR spectra of the anodized Cu sample and Cu foil reference can be seen in Figure 2j. No peaks were detected for the Cu foil, whereas the Cu(OH)₂ sample displayed four major peaks. The peaks found at 3566 cm⁻¹ and 3296 cm⁻¹ are ascribed to the stretching modes of the OH groups. More precisely, the peak at 3566 cm⁻¹ belongs to the free OH group and the peak at 3296 cm⁻¹ is due to the hydrogen-bonded OH group.^[12] Furthermore, the peaks at 934 cm⁻¹ and 678 cm⁻¹ arise from the Cu–O–H bonds.^[13]

The product selectivity of the Cu foil as a function of potential is shown in Figure 3a. Consistent with previous reports, the Cu foil favours the formation of CH₄. In comparison, the Cu(OH)₂ catalyst effectively suppresses the formation of CH₄ in favour of C₂H₄ production (Figure 3b). A peak FE(C₂H₄) of 36.5% is attained for the Cu(OH)₂ catalyst at a potential of −1.0 V vs. RHE, which is more than double that of the pristine Cu foil operating at the same potential.

Next, we sought to test the stability of the catalysts by performing CO₂RR for 6 h at −1.0 V vs. RHE. In the stability test, the electrochemically active surface area (ECSA) was used to normalize the current. The roughness factor of the Cu(OH)₂ catalyst was calculated to be 6.17 relative to the pristine Cu, with an ECSA of 2.96 cm². Over the duration of the test, the Cu foil shows a decrease in current density from 8.5 to 2.2 mA cm^{−2}, with FE(C₂H₄) declining after one hour of operation (Figure 3c). At the end of the 6-hour stability test, the Cu foil displayed a FE(C₂H₄) of ~4%, down from an initial FE of ~19%. The decline in FE(C₂H₄) was accompanied by a doubling in the FE(H₂) and FE(CO), showing clear signs of deactivation. On the other hand, the Cu(OH)₂ catalyst showed exceptionally stable C₂H₄ selectivity. An increase in the current density from 3.3 to 3.9 mA cm^{−2}, together with a minor increase in both FE(H₂) and FE(CH₄), was observed. The increase in FE(CH₄) is rather low, from 0.6% at the beginning of the test, to 1.2% after 6 h, whereas the FE(H₂) increased by ~2%. The increase in CH₄ production, in combination with a drop of ~1% in the FE(C₂H₄), results in a slightly lower C₂H₄ to CH₄ ratio as seen in Figure 3d. After one hour of operation, a C₂H₄ to CH₄ ratio of 38 is observed, whereas a ratio of 30 is retained after 6 h.

Conclusion

In summary, a two-step synthesis method for growing homogeneous Cu(OH)₂ nanoneedle films over large surface areas was developed by using a sodium persulfate pre-treatment step prior to anodization. A direct anodization of the pristine Cu foil resulted in low quality Cu(OH)₂ nanoneedle films with several pinholes and patches with uneven growth. In contrast, inclusion of the pre-treatment step aided in the homogenous growth of Cu(OH)₂ without defects by providing a uniform surface roughness through the elimination of crevices, removal of the native oxide layer and carbon on the surface and improving the contact at the interface of the Cu foil and electrolyte due to better wetting as the surface energy had been increased. As a catalyst for CO₂RR, the Cu(OH)₂ demonstrates a strong preference for C₂H₄, reaching a FE(C₂H₄) of 36.5% at −1.0 V vs. RHE. Furthermore, a stable formation of C₂H₄ was obtained for 6 h in which a ratio of C₂H₄ to CH₄ production of 30:1 was achieved at the end of the 6-hour stability test. In comparison, the pristine Cu foil rapidly declined in terms of both C₂H₄ selectivity and current density while the hydrogen evolution reaction selectivity doubled.

Experimental Section

Catalyst preparation. The catalyst was made from 0.1 mm thick Cu foils (99.9999%) with a geometrical surface area of 63 cm². The foils were cleaned using acetone and isopropanol and rinsed in deionized water. The Cu foils were then etched in 20% sodium persulfate solution for 5 min and 30 seconds (Step 1), rinsed in deionized water and ethanol before drying with nitrogen. Anodization of the copper foils was immediately performed in a 3 M KOH solution in a Teflon beaker with a Pt mesh acting as a counter electrode (Step 2). A current density of 1.6 mA cm^{−2} was applied for 15 min at room temperature. For the electrochemical CO₂ reduction measurements, the Cu(OH)₂ samples were cut into smaller pieces with a geometrical surface area of 0.48 cm², while the Cu foil catalyst had a geometrical surface area of 1 cm².

Material characterization. The crystal structure of the catalysts was investigated with low angle X-ray diffraction (XRD) (Thermo Fischer Equinox 1000) using Cu-K α radiation with a wavelength of 1.54 Å. Fourier-transform infrared spectroscopy, FTIR, (Thermo Fischer Nicolet iS50) was used to detect the chemical bonds associated with Cu(OH)₂. Surface morphologies were observed using a scanning electron microscope (SEM) (Hitachi SU 3500), which was equipped with an electron dispersive x-ray spectroscopy (EDX) for elemental analysis.

Electrochemical measurements. All electrochemical measurements were performed with a CHI660E electrochemical workstation in a custom glass H-cell (Adams and Chittenden). A Nafion 117 proton exchange membrane separated the anodic and cathodic compartments. The counter and reference electrodes consisted of a coiled Pt wire and Ag/AgCl (3 M KCl), respectively. The cathodic and anodic side were filled with 80 mL of CO₂-saturated 0.1 M KHCO₃ electrolyte with a measured pH of 6.8. iR compensation was performed by measuring the resistance vs. the open circuit potential and was in the range of 6–14 Ω . Measurements were conducted for 90 min at each potential, with a fresh catalyst and electrolyte used for each run. All catalysts were pre-conditioned at a potential of −1.1 V vs the reversible hydrogen electrode (RHE) for 300 s prior to the CO₂RR. The potentials were converted to RHE using Equation (2).

$$E \text{ vs RHE} = E \text{ vs Ag/AgCl (3 M KCl)} + 0.209V + 0.05916 \times \text{pH} \quad (2)$$

The roughness factor and ECSA were determined by running cyclic voltammetry (CV) scans at different scan rates in the non-faradaic region of −0.1 to −0.3 V vs. RHE. The double layer capacitance (C_{dl}) was calculated from the difference between the cathodic (i_c) and anodic (i_a) currents peaks divided by the scan rate according to Equation (3). The value obtained from the pristine Cu foil was used as a reference.

$$C_{dl} = \frac{i_c - i_a}{\text{scan rate}} \quad (3)$$

The roughness factor (R_f) of the Cu(OH)₂ catalyst was calculated by dividing the C_{dl} to that of the pristine Cu catalyst. ECSA was obtained from Equation (4), where S is the geometrical surface area.

$$\text{ECSA} = R_f S \quad (4)$$

Gas quantification. The experimental setup is presented in Figure 1b. The quantification of gaseous reaction products was done using a gas chromatograph, GC, (Shimadzu-GC-2010 PLUS) equipped with a ShinCarbon ST column for separation of the gases and a Dielectric-Barrier Discharge Ionization Detector (BID). Helium

(99.9999%) was used as the carrier gas. The H-cell was set up in an on-line configuration with the headspace of the cathodic compartment connected to a 6-port sampling valve equipped with a 0.5 mL sample loop for injection. A Nafion tubing dryer was connected between the cell and the gas-sampling valve to reduce the amount of water vapour present in the gas stream. The calibration curves were made using custom-made gas mixtures containing H₂, CO, CH₄, C₂H₄, and C₂H₆ in a CO₂ balance (Nippon Gases). A mass flow controller was used to set the flow rate of CO₂ (20 sccm) being continuously fed into the cell. The content of the sample loop was injected into the GC every 30 min over the duration of the experiments. The Faradaic efficiency (FE) was calculated using the formula in Equation (5), where m is the number of moles of product derived from the GC measurement, n_x is the number of electrons required for reduction to product x , F is Faraday's constant (96500 C/mol), and Q is the charge (in C). In our case, the charge was calculated as the time it takes to fill the sample loop based on the gas flow rate multiplied with the current averaged 30 s prior to injection.

$$FE = \frac{m \times n_x \times F}{Q} \times 100 \quad (5)$$

Prior to the experiments, a silver foil was used as a catalyst for CO₂RR to ensure that the setup was working properly. Silver foil is known to produce only H₂ and CO, meaning that the FE should be close to 100%. A total FE of 98.1% was attained for the silver catalyst at a potential of -1.1 V vs RHE.

Acknowledgements

The authors acknowledge support from the research grants GRAFTID (project #RO-NO-2019-0616 from EEA (European Economic Area)-Norway-Romania), EEA-Poland NOR/POLNORCCS/PhotoRed/0007/2019-00, and the Research Council of Norway projects #314012 and #295864.

Conflict of Interest

The authors declare no conflict of interest.

Data Availability Statement

The data that support the findings of this study are available from the corresponding author upon reasonable request.

Keywords: anodization · copper hydroxide · electrochemical CO₂ reduction · multicarbon reaction products · nanoneedles

- [1] K. R. Gustavsen, K. Wang, *Phys. Chem. Chem. Phys.* **2021**, *23*, 12514–12532.
- [2] G. Iijima, T. Inomata, H. Yamaguchi, M. Ito, H. Masuda, *ACS Catal.* **2019**, *9*, 6305–6319.
- [3] Y. Zhou, Y. Liang, J. Fu, K. Liu, Q. Chen, X. Wang, H. Li, L. Zhu, J. Hu, H. Pan, M. Miyauchi, L. Jiang, E. Cortés, M. Liu, *Nano Lett.* **2022**, *22*, 1963–1970.
- [4] a) F. Xiao, S. Yuan, B. Liang, G. Li, S. O. Pehkonen, T. Zhang, *J. Mater. Chem. A* **2015**, *3*, 4374–4388; b) T. G. S. Babu, T. Ramachandran, *Electrochim. Acta* **2010**, *55*, 1612–1618.
- [5] a) L. Shooshtari, R. Mohammadpour, A. I. Zad, *Mater. Lett.* **2016**, *163*, 81–84; b) N. K. Allam, C. A. Grimes, *Mater. Lett.* **2011**, *65*, 1949–1955.
- [6] L. Arurault, M. H. Belghith, R. S. Bes, *J. Mater. Sci.* **2007**, *42*, 1190–1195.
- [7] W. J. Stepniowski, S. Stojadinović, R. Vasilčić, N. Tadić, K. Karczewski, S. T. Abrahami, J. G. Buijnsters, J. M. C. Mol, *Mater. Lett.* **2017**, *198*, 89–92.
- [8] D. S. Zimbovskiy, A. I. Gavrilov, B. R. Churagulov, *Iop. Conf. Ser. Mater. Sci. Eng.* **2018**, *347*, 012010.
- [9] G. Liu, K. Du, K. Wang, *Appl. Surf. Sci.* **2016**, *388*, 313–320.
- [10] X. Wu, H. Bai, J. Zhang, F. e Chen, G. Shi, *J. Phys. Chem. B* **2005**, *109*, 22836–22842.
- [11] a) D. Reyster, M. Odziemkowski, D. Bélanger, L. Roué, *J. Electrochem. Soc.* **2007**, *154*, K36; b) Y. Deng, A. D. Handoko, Y. Du, S. Xi, B. S. Yeo, *ACS Catal.* **2016**, *6*, 2473–2481.
- [12] A. M. Awwad, B. Albiss, *Adv. Mater. Lett.* **2015**, *6*, 51–54.
- [13] C. Henrist, K. Traina, C. Hubert, G. Toussaint, A. Rulmont, R. Cloots, *J. Cryst. Growth* **2003**, *254*, 176–187.

Manuscript received: June 10, 2022

Revised manuscript received: August 29, 2022

Article 3

Gustavsen, K.R, Johannessen E.A, and Wang, K. (2023). Carbon Modified Thin-film Catalysts for Electrochemical Reduction of CO₂ with Tunable H₂/CO Ratio. *Electrochemistry Communications*, 155, 107582. doi: 10.1016/j.elecom.2023.107582.



Carbon modified silver thin-film catalysts for electrochemical reduction of CO₂ to syngas with tunable H₂/CO ratio

Kim Robert Gustavsen, Erik Andrew Johannessen, Kaiying Wang*

Department of Microsystems, University of South-Eastern Norway, Horten 3184, Norway

ARTICLE INFO

Keywords:

AgC
Carbon doped silver
electrochemical CO₂ reduction
Silver catalyst
Syngas production
Thin films

ABSTRACT

This study investigates carbon (C)-modified silver (Ag) thin film catalysts for electrochemical syngas production. The Ag-C catalyst is synthesized using a co-deposition process with separate C and Ag sputtering targets. It is found that co-deposition with C increases nucleation rate during film growth, which reduces particle size and increases the surface area, as well as increasing the selectivity for the hydrogen evolution reaction (HER). A 10-fold improvement in the geometric current density is obtained for the Ag-C thin film relative to Ag due to a high abundance of active sites, and a H₂/CO ratio between 1.4 and 2.5 is attained within the potential range of – 0.6 to – 1.0 V. vs RHE. Thus, regulating the C concentration allows the H₂/CO ratio to be tuned while maintaining a surface architecture that permits large geometric current densities, both being desirable properties for catalysts used in syngas applications.

1. Introduction

The electrochemical reduction of carbon dioxide through the CO₂ reduction reaction (CO₂RR) could help meet future energy demands by generating value-added liquid fuels and chemical feedstocks that are carbon neutral. One challenge lies in activating the CO₂ molecule, which requires high overpotentials, as well as being in the potential range of the hydrogen evolution reaction (HER). The result is a low faradaic efficiency (FE) for the CO₂ reduction process. Despite significant efforts to suppress HER and activate CO₂ molecules through catalyst design, there remains an urgent need for cost effective stable catalysts with high FE and selectivity for CO₂. One potential solution is to permit the HER process to proceed and to combine this with CO₂RR to produce syngas with adjustable H₂/CO ratios. Syngas is commonly generated from the energy-intensive water–gas shift reaction, which utilizes CO and water at high temperatures to produce H₂ at desired ratios [1]. However, the process emits CO₂ as a byproduct, which raises environmental concerns. Being able to fine tune the H₂/CO ratio of the syngas allows the mixture to be used directly in existing thermocatalytic processes such as the Fischer-Tropsch (FT) and direct methanol synthesis, eliminating the need for the water gas shift reaction [2].

Designing catalysts for syngas formation requires the use of group 2 transition metals in the CO₂RR. These produce CO as their main product due to their inherent weak binding of CO, which permits efficient

desorption of the CO molecule [3]. Among these transition metals, silver (Ag), gold (Au), and palladium (Pd) have been explored as potential catalysts for production of syngas [2,4–8], of which Ag is considered the most viable from an economic perspective due to its significantly lower cost compared to Au and Pd. However, Ag exhibits the lowest catalytic activity of the three and often requires larger overpotentials to achieve satisfactory reaction rates. Thus, to utilize Ag as a catalyst for syngas formation the reaction rate must be enhanced, the H₂/CO ratio must be controlled, and preferably the Ag content should be minimized to further reduce the cost. To address these challenges, nanostructured Ag catalysts have been employed [6,9], which can maximize the exposed surface area to increase the number of active sites, which in turn boost reaction rates at the same time as the Ag loading is reduced. In order to achieve this, carbon (C) and its derivatives are often used as a support for Ag to make use of its porous structure [10]. In addition, the H₂/CO production ratio can be controlled by adjusting the Ag loading [11]. Therefore, from this viewpoint, the creation of Ag-C thin films is appealing as it allows for control over C concentration and film thickness. This could help minimize the Ag loading, thus reducing costs. Moreover, thin film deposition can readily be scaled up, and it eliminates the use of binders that are necessary for fixing Ag nanostructures to electrodes, which can block access to active sites [10].

* Corresponding author.

E-mail address: kaiying.wang@usn.no (K. Wang).

<https://doi.org/10.1016/j.elecom.2023.107582>

Received 23 August 2023; Received in revised form 11 September 2023; Accepted 13 September 2023

Available online 15 September 2023

1388-2481/© 2023 The Author(s). Published by Elsevier B.V. This is an open access article under the CC BY license (<http://creativecommons.org/licenses/by/4.0/>).

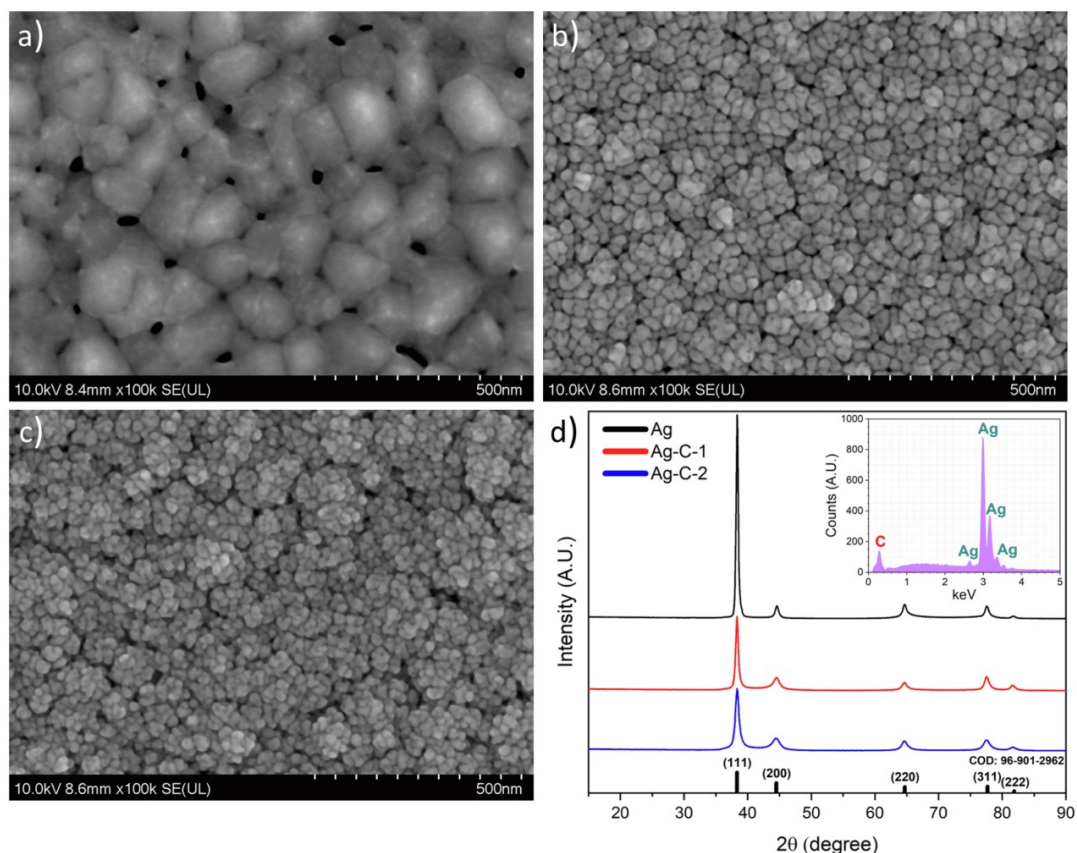


Fig. 1. SEM image of the a) Ag, b) Ag-C-1, and c) Ag-C-2 thin films. d) XRD patterns of the Ag and Ag-C films with inset of the EDX spectrum of Ag-C-2.

2. Methods

2.1. Catalyst synthesis

A 15 nm Chromium (Cr) adhesion layer was deposited onto soda lime glass pieces ($3 \times 0.5 \text{ cm}^2$) by e-beam deposition. The thin films were deposited by a magnetron co-deposition process with a direct current (DC) power of 100 W applied to the Ag target, while the radio frequency (RF) power of the C target was varied to synthesize two different Ag-C films: Ag-C-1 (350 W) and Ag-C-2 (500 W).

2.2. Material characterization

The XRD spectra were obtained using a Thermo Fisher Equinox 1000 low angle x-ray diffraction (XRD). The surface morphology and electron dispersive spectroscopy (EDX) analysis were performed using a Hitachi SU 8230 FE-SEM.

2.3. Electrochemical measurements

Electrochemical measurements were performed using an H-cell where the anodic and cathodic compartments were separated by a Nafion 117 proton exchange membrane. The chambers were filled with 75 mL of 0.5 M KHCO_3 electrolyte saturated with CO_2 , having a pH of 7.4. iR compensation was conducted by observing the resistance versus the open circuit potential. All electrochemical measurements utilized a three-electrode configuration employing a Pt wire counter electrode and an Ag/AgCl (3 M KCl) reference electrode. Linear sweep voltammetry

(LSV) curves were derived at a scan rate of 10 mV/s before and after saturating the electrolyte with CO_2 . For the determination of the product selectivity each catalyst was tested at various potentials for 20 min, with fresh electrolyte used for every catalyst. The tests were repeated three times for each catalyst. Subsequently, all potentials were converted to the reversible hydrogen electrode (RHE) using the Nernst equation. The electrochemically active surface area (ECSA) was calculated from the double-layer capacitance (C_{DL}) which was extracted from cyclic voltammetry (CV) scans performed in the non-faradaic region of -0.20 to -0.35 V vs. RHE with scan rates of 50 – 250 mV/s. The C_{DL} was determined by calculating the linear fit of the difference between the cathodic and anodic current density at -0.275 V vs. RHE as a function of the scan rate. The roughness factor (r_f) was calculated by dividing the C_{DL} value obtained for the Ag-C catalysts by that of the Ag reference. Finally, the ECSA was determined by multiplying the r_f with the geometric surface area of the catalyst. Gaseous reaction products were quantified using a Shimadzu-GC-2010 PLUS gas chromatograph (GC), featuring a ShinCarbonST column and a dielectric-barrier discharge ionization detector (BID). The gas was sampled every 20 min through an on-line configuration. The setup used for gas analysis has been reported previously [12].

3. Results and discussion

The surface morphology of the films as imaged by SEM can be seen in Fig. 1a-c. The pristine Ag film displays large grains with an average size of ~ 150 nm. However, when C is co-deposited with Ag, the particle size shrinks significantly, resulting in an average size of ~ 35 and ~ 25 nm

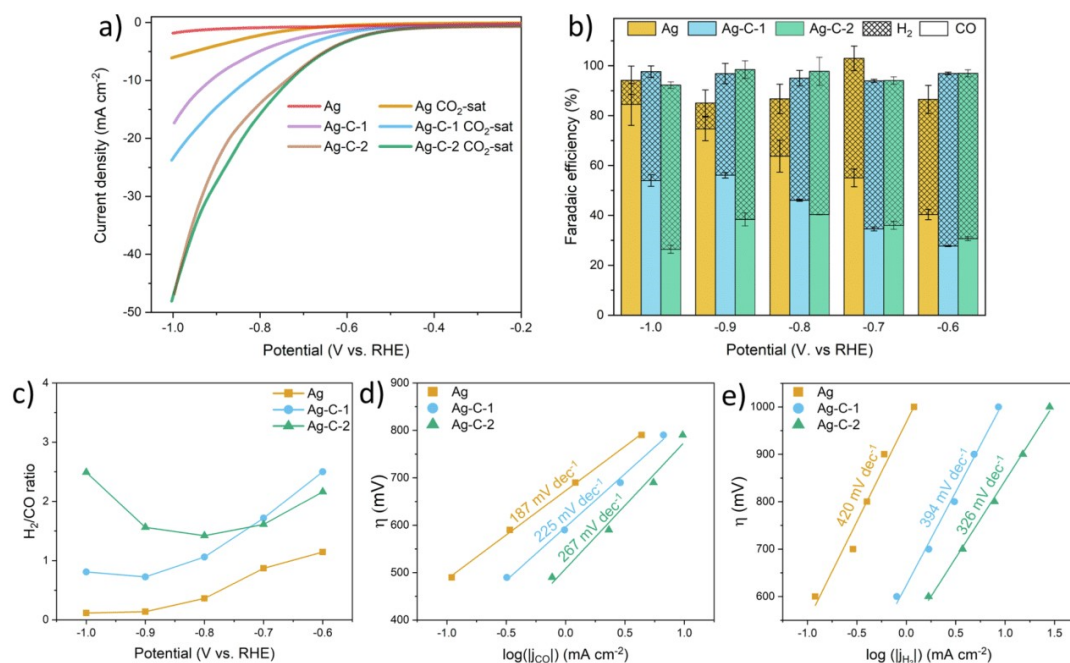


Fig. 2. Electrochemical characterization of the catalysts. a) LSV of the Ag and Ag-C catalysts, b) their product selectivity as a function of potential, c) the ratio of H₂/CO, the Tafel slope for d) CO formation and e) HER.

for the Ag-C-1 and Ag-C-2 films, respectively. Although the morphology for the Ag-C films is similar, the Ag-C-2 film consists of slightly smaller particles. EDX shows an increase in the C concentration from 2.3 at% for Ag to 7.6 and 13.4 at% for the Ag-C-1 and Ag-C-2 films, respectively. The small amount of C found in the pristine Ag film is likely due to C on the surface, but the EDX data provides an obvious trend in the C concentration with increasing RF sputtering power of the C target. The EDX spectrum obtained for the Ag-C-2 film can be seen in Fig. 1d inset. Next, the crystal structure of the films was investigated by XRD. The XRD pattern (Fig. 1d) of the sputtered Ag film displays a polycrystalline structure, with a high intensity Ag (111) peak. When C is co-sputtered with Ag, the Ag (111) peak intensity is reduced, and a broadening of the peaks can be observed, which results in a small bridge forming between the Ag (111) and Ag (200) peaks for the Ag-C-1 and Ag-C-2 films. The Debye-Scherrer equation was utilized to calculate the average crystallite size of the films by using the full-width half maximum (FWHM) of the Ag (111) peak. A crystallite size of 18.8 nm is calculated for pristine Ag, which is reduced to 14.0 nm for Ag-C-1, and further reduced to 9.5 nm for the Ag-C-2 film. Thus, the crystallite size is halved for the Ag-C-2 film relative to pristine Ag. The simultaneous reduction in particle size, crystallite size, and Ag (111) peak intensity suggests a disruption of the growth kinetics when co-sputtering with C due to the competitive growth of Ag and C during deposition. More precisely, an increase in the nucleation rate and suppressed growth of Ag leads to a reduction in particle and crystallite size. No shift in the diffraction angle of the Ag peaks that could indicate the placement of C in the Ag lattice was detected. Furthermore, no peaks associated with any C phase was detected, which could be due to the low concentrations relative to Ag, but more likely due to C exhibiting an amorphous structure.

Next, the catalytic performance of the films was determined by performing electrochemical CO₂ reduction in 0.5 M KHCO₃ with all potentials referenced to RHE. LSV scans reveal a substantial increase in current density for the Ag-C films that becomes larger when the C concentration is increased (Fig. 2a). Furthermore, when the electrolyte is saturated with CO₂, Ag and Ag-C-1 display enhanced current densities,

whereas the difference before and after saturation is minor for Ag-C-2. For all the catalysts, CO and H₂ were the only gaseous reaction products detected, with a total faradaic efficiency (FE) close to 100%. The FE obtained for CO and H₂ in the potential range of -0.6 to -1.0 V can be seen in Fig. 2b. Pristine Ag shows a steady increase in FE(CO) as the applied potential becomes more negative, reaching a peak FE(CO) of 84.5% at -1.0 V. In comparison Ag-C-1 exhibits an overall lower FE(CO), with a peak of 56.1% at -0.9 V, whereby a reduction in FE(CO) is observed when increasing the potential to -1.0 V. A further reduction in FE(CO) is seen for Ag-C-2, with a peak FE(CO) of 40.4% at -0.8 V. Thus, Ag-C shows a significant decrease in the selectivity towards CO₂ reduction in favor of HER, which becomes more pronounced at more negative potentials. The strong preference of the Ag-C-2 catalyst for HER could explain why saturating the electrolyte with CO₂ only resulted in minor variation in current density during LSV. Overall, the current densities are vastly increased for the Ag-C films, resulting in a larger partial current density of CO (J_{CO}) for the Ag-C catalysts at all potentials. It should be noted that the effect is more subtle at -1.0 V due to the high selectivity of Ag towards CO at this potential compared to the Ag-C catalysts. The activity towards HER was substantially higher for Ag-C, with a partial current density of H₂ (J_{H_2}) that was 28-fold larger for Ag-C-2 than for Ag at -1.0 V. The H₂/CO ratio of the Ag and Ag-C films obtained within the applied potential range can be seen in Fig. 2c. It is observed that the Ag-C-1 display a slightly larger H₂/CO ratio than Ag-C-2 at -0.6 V and -0.7 V, but the ratio declines at more negative potentials in a similar fashion to the Ag reference. On the other hand, Ag-C-2 show a parabolic curve for the H₂/CO ratio as a function of the applied potential, with start- and end points offering a H₂/CO ratio close to 2, which is ideal for the Fischer Tropsch and direct methanol synthesis. In comparison, the Ag reference catalyst obtains a H₂/CO ratio of 1.14 at -0.6 V that rapidly decreases to 0.12 at -1.0 V. These results show that the H₂/CO ratio appears to be tunable by first controlling the C concentration introduced into the films during co-deposition, and secondly by controlling the applied potential. From the Tafel slopes for the CO₂ reduction plotted in Fig. 2d, Ag exhibits a slope of 187 mV/dec, which

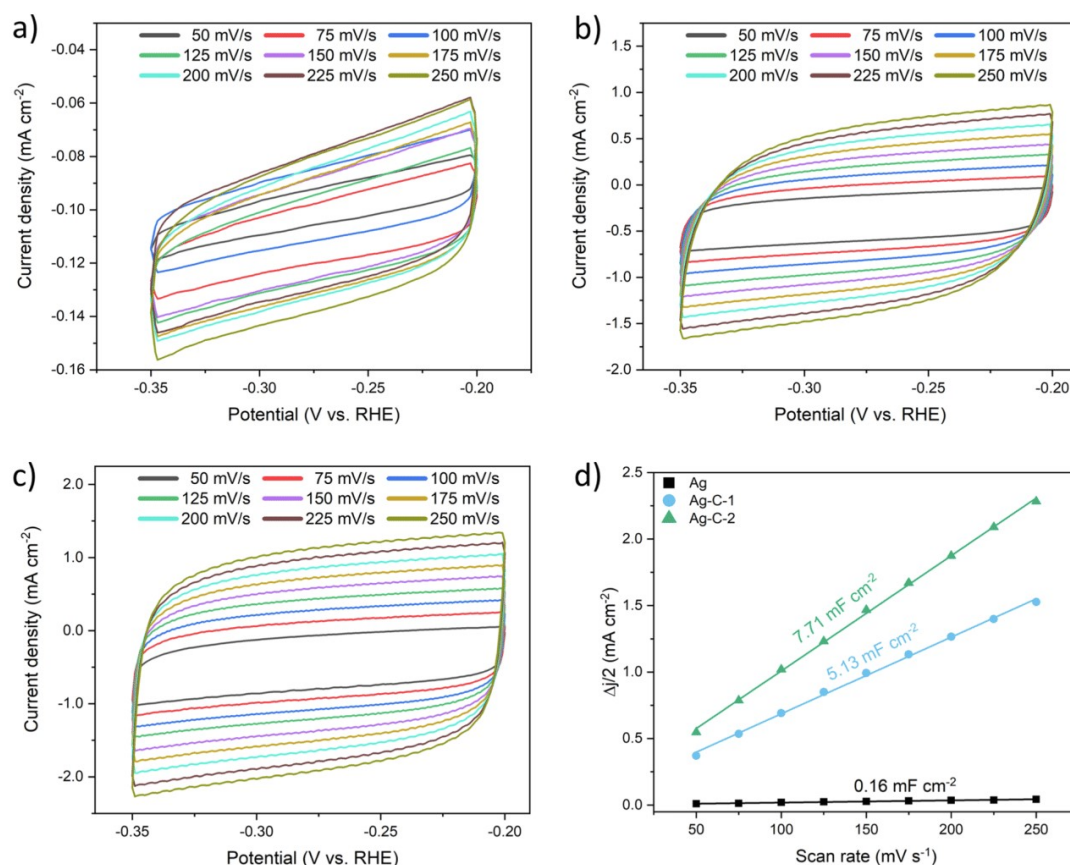


Fig. 3. CV scans performed at various scan rates for a) Ag, b) Ag-C-1, and c) Ag-C-2. d) C_{DL} slopes obtained from the CV scans in a)-c).

increases to 225 mV/dec for Ag-C-1 and 266 mV/dec for the Ag-C-2 catalyst. On the other hand, the Tafel slope for HER was reduced by ~ 100 mV/dec for the Ag-C-2 catalyst relative to Ag (Fig. 2e). Thus, the electrochemical CO₂ reduction becomes more sluggish while HER shows improved kinetics with increasing concentrations of C. It is well known that C does not contribute towards the CO₂RR but have a proven capability of HER in a KHCO₃ electrolyte [13]. Therefore, an increase in C relative to Ag would favor HER over CO₂ reduction. Other factors that could enhance the selectivity towards HER is the reduction in Ag particle size, which in transition-metals have shown to increase both current densities and HER selectivity due to exhibiting a larger amount of edge and corner sites [5,14,15]. However, these particle size effects have been reported primarily for nanoparticles which are significantly smaller than the ones observed for the Ag-C films (<10 nm). Thus, the contribution of these morphological effects on the selectivity is considered minor in comparison to C. As the increase in J_{CO} could not be attributed to improved kinetics for the CO₂ reduction, it was believed that an increase in the surface area due to the porosity introduced by C could be responsible. Thus, a set of CV scans were performed at various scan rates in the range -0.2 to -0.35 V as seen in Fig. 3a-c to extract the C_{DL} , which was used to determine the ECSA. A significant increase is seen in the C_{DL} , from 0.16 mF/cm² for Ag, to 5.13 mF/cm² for Ag-C-1 and 7.71 mF/cm² for Ag-C-2 (Fig. 3d). The r_f relative to the pristine Ag film was 32 and 48 for Ag-C-1 and Ag-C-2, respectively. This corresponded to an ECSA of 0.75 cm² (Ag), 27 cm² (Ag-C-1), and 36 cm² (Ag-C-2), making the ECSA vastly larger for the Ag-C films, which explains the substantial increase in current density. The increase in ECSA results in a reaction rate that is significantly larger compared to the Ag

nanowires at C sheets reported by Cho et.al [16], which achieved a similar H₂/CO ratio of syngas by varying the Ag nanowire loading. In terms of reaction rate and ability to tune the syngas ratio the performance of the Ag-C thin films is more comparable to the nanostructured Ag mesh reported by Lim et. al. [17]. However, from a cost-perspective the Ag-C thin films are more attractive since the overall material consumption can be reduced.

4. Conclusion

Ag-C composite catalysts were synthesized through a co-sputtering process using an Ag and C sputtering target. The co-deposition of C with Ag reduced the particle size from ~ 150 nm to < 40 nm while also reducing the crystallite size due to an increase in the nucleation rate that suppresses Ag growth. The Ag-C films display a significant increase in reaction rate relative to Ag, where the overall selectivity for CO is reduced in favor of HER. The increase in the ECSA for the Ag-C films due to the smaller particle size and porous nature of C make the Ag-C films capable of achieving large current densities due to an abundance of active sites, where the H₂/CO ratio can be tuned by adjusting the C concentration of the film. The combined ability to control the H₂/CO ratio while allowing for large geometric current densities makes the Ag-C an attractive syngas catalyst.

CRedit authorship contribution statement

Kim Robert Gustavsen: Conceptualization, Methodology, Investigation, Visualization, Writing – original draft. Erik Andrew

Johannessen: Supervision, Writing – review & editing. **Kaiying Wang:** Supervision, Funding acquisition, Writing – review & editing.

Declaration of Competing Interest

The authors declare that they have no known competing financial interests or personal relationships that could have appeared to influence the work reported in this paper.

Data availability

Data will be made available on request.

Acknowledgements

The authors K.R.G. and K.W. acknowledge the research grants from EEA (European Economic Area)-Norway-Romania project #Graftid, RO-NO-2019-0616 and EEA-Poland-NOR/POLNORCCS/ PhotoRed/0007/2019-00. K.R.G. acknowledge support from the Norwegian Micro- and Nano- Fabrication Facility (NorFab, No. 245963/F50) and the strategic research plan of the University of South-Eastern Norway.

References

- [1] D.B. Pal, R. Chand, S.N. Upadhyay, P.K. Mishra, Performance of water gas shift reaction catalysts: A review, *Renew. Sustain. Energy Rev.* 93 (2018) 549–565.
- [2] B.M. Tackett, J.H. Lee, J.G. Chen, Electrochemical Conversion of CO₂ to Syngas with Palladium-Based Electrocatalysts, *Acc. Chem. Res.* 53 (2020) 1535–1544.
- [3] Y. Hori, H. Wakebe, T. Tsukamoto, O. Koga, Electrocatalytic process of CO selectivity in electrochemical reduction of CO₂ at metal electrodes in aqueous media, *Electrochim. Acta* 39 (1994) 1833–1839.
- [4] J.H. Lee, S. Kattel, Z. Jiang, Z. Xie, S. Yao, B.M. Tackett, W. Xu, N.S. Marinkovic, J. G. Chen, Tuning the activity and selectivity of electroreduction of CO₂ to synthesis gas using bimetallic catalysts, *Nat. Commun.* 10 (2019) 3724.
- [5] H. Mistry, R. Reske, Z. Zeng, Z.-J. Zhao, J. Greeley, P. Strasser, B.R. Cuenya, Exceptional Size-Dependent Activity Enhancement in the Electroreduction of CO₂ over Au Nanoparticles, *J. Am. Chem. Soc.* 136 (2014) 16473–16476.
- [6] W. Xi, R. Ma, H. Wang, Z. Gao, W. Zhang, Y. Zhao, Ultrathin Ag Nanowires Electrode for Electrochemical Syngas Production from Carbon Dioxide, *ACS Sustain. Chem. Eng.* 6 (2018) 7687–7694.
- [7] M.A. Parkhondehfar, S. Hernández, M. Rattalino, M. Makkee, A. Lamberti, A. Chiodoni, K. Bejtka, A. Sacco, F.C. Pirri, N. Russo, Syngas production by electrocatalytic reduction of CO₂ using Ag-decorated TiO₂ nanotubes, *Int. J. Hydrogen Energy* 45 (2020) 26458–26471.
- [8] Y.E. Kim, B. Kim, W. Lee, Y.N. Ko, M.H. Youn, S.K. Jeong, K.T. Park, J. Oh, Highly tunable syngas production by electrocatalytic reduction of CO₂ using Ag/TiO₂ catalysts, *Chem. Eng. J.* 413 (2021), 127448.
- [9] L. Zeng, J. Shi, H. Chen, C. Lin, Ag Nanowires/C as a Selective and Efficient Catalyst for CO₂ Electroreduction, *Energies* 14 (2021) 2840.
- [10] J. Hong, K.T. Park, Y.E. Kim, D. Tan, Y.E. Jeon, J.E. Park, M.H. Youn, S.K. Jeong, J. Park, Y.N. Ko, W. Lee, Ag/C composite catalysts derived from spray pyrolysis for efficient electrochemical CO₂ reduction, *Chem. Eng. J.* 431 (2022), 133384.
- [11] F. Sastre, M.J. Muñoz-Batista, A. Kubacka, M. Fernández-García, W.A. Smith, F. Kapteijn, M. Makkee, J. Gascon, Efficient Electrochemical Production of Syngas from CO₂ and H₂O by using a Nanostructured Ag/g-C₃N₄ Catalyst, *ChemElectroChem* 3 (2016) 1497–1502.
- [12] K.R. Gustavsen, E.A. Johannessen, K. Wang, Sodium Persulfate Pre-treatment of Copper Foils Enabling Homogenous Growth of Cu(OH)₂ Nanoneedle Films for Electrochemical CO₂ Reduction, *ChemistryOpen* 11 (2022) e202200133.
- [13] M. Azuma, K. Hashimoto, M. Hiramoto, M. Watanabe, T. Sakata, Electrochemical Reduction of Carbon Dioxide on Various Metal Electrodes in Low-Temperature Aqueous KHCO₃ Media, *J. Electrochem. Soc.* 137 (1990) 1772.
- [14] X. Deng, D. Alfonso, T.-D. Nguyen-Phan, D.R. Kauffman, Resolving the Size-Dependent Transition between CO₂ Reduction Reaction and H₂ Evolution Reaction Selectivity in Sub-5 nm Silver Nanoparticle Electrocatalysts, *ACS Catal.* 12 (2022) 5921–5929.
- [15] R. Reske, H. Mistry, F. Behafarid, B. Roldan Cuenya, P. Strasser, Particle Size Effects in the Catalytic Electroreduction of CO₂ on Cu Nanoparticles, *J. Am. Chem. Soc.* 136 (2014) 6978–6986.
- [16] M. Cho, J.-W. Seo, J.T. Song, J.-Y. Lee, J. Oh, Silver Nanowire/Carbon Sheet Composites for Electrochemical Syngas Generation with Tunable H₂/CO Ratios, *ACS Omega* 2 (2017) 3441–3446.
- [17] J. Lim, H. Lim, B. Kim, S.M. Kim, J.-B. Lee, K.R. Cho, H. Choi, S. Sultan, W. Choi, W. Kim, Y. Kwon, Local pH induced electrochemical CO₂ reduction on nanostructured Ag for adjustable syngas composition, *Electrochim. Acta* 395 (2021), 139190.

Article 4

Gustavsen, K.R, Hao, H, Johannessen E.A, and Wang, K. (2023). Boron-induced growth of highly textured Ag (111) films with nano-tentacle structures for the electrochemical reduction of CO₂ to CO. *Electrochemistry Communications*, 156, 107600. doi: 10.1016/j.elecom.2023.107600.



Boron-induced growth of highly textured Ag (1 1 1) films with nano-tentacle structures for the electrochemical reduction of CO₂ to CO

Kim Robert Gustavsen, Hao Huang, Erik Andrew Johannessen, Kaiying Wang*

Department of Microsystems, University of South-Eastern Norway, Horten 3184, Norway

ARTICLE INFO

Keywords:

AgB
Boron doped silver
Electrochemical CO₂ reduction
Nano-tentacles
Silver catalyst

ABSTRACT

Ag is a cost-effective alternative to Au as a catalyst for the electrochemical reduction of CO₂ into CO, but a reduction in the accompanying overpotential is required to make Ag viable. In this study we use B to modulate the catalytic performance of Ag towards the electrochemical reduction of CO₂ to CO. Initial DFT simulations disclose a deviation from the linear scaling relations with the inclusion of B that stabilizes the *COOH intermediate while weakening the binding strength of *CO. A magnetron co-sputtering process is used to develop a catalyst based on B-induced crystal growth of highly textured Ag (1 1 1) films. Incorporation of B facilitates the formation of Ag (1 1 1) coherent twin boundaries, which gives rise to unique nano-tentacle structures. The Ag-B catalyst achieves a faradaic efficiency of CO production of 97.9% at -0.9 V vs RHE with a partial current density that is four times higher compared to pristine Ag. Thus, the inclusion of B into Ag offers a facile approach for circumventing the linear scaling relations, allowing for the design of electrocatalysts with high faradaic efficiencies and current densities.

1. Introduction

The ever-increasing atmospheric concentrations of carbon dioxide (CO₂) poses a formidable threat to modern society due to the severe effects on the climate. Development and utilization of carbon neutral renewable energy technologies is necessary to reduce our dependency on fossil fuels. One such technology is the electrochemical reduction of CO₂, which can directly tackle the CO₂ emission while acting as a potent energy storage method when combined with intermittent renewable energy sources based on e.g., wind and solar power. However, the electrochemical reduction of CO₂ requires the use of stable catalysts that offer high selectivity for a given reaction product. Achieving such a high selectivity while maintaining good reaction rates and low overpotentials remains a challenge due to the slow kinetics of the CO₂ reduction reaction at standard conditions as well as the presence of the competing hydrogen evolution reaction (HER).

One desirable reaction product of CO₂ reduction is carbon monoxide (CO), which is attractive because CO can be used as a feedstock in the Fischer-Tropsch process to produce hydrocarbons. Both Au and Ag catalysts offer high faradaic efficiencies (FE) in the generation of CO due to low inherent binding strength of *CO, which permits an efficient desorption of the molecule from the catalyst surface [1]. While Ag would

be the preferred choice due to its significantly lower cost, it requires considerably higher overpotentials than Au to reach high FE(CO). Theoretical studies have indicated that the overpotential is directly linked to the binding energy of the *COOH intermediate, and that increasing the binding energy effectively reduces the overpotential [2]. However, the linear scaling relations of the chemisorption energies between *CO and *COOH makes it difficult to individually tune their binding energies. Meaning that increasing the binding strength of *COOH also increases that of *CO, which may impair its desorption and lead to a reduction in FE. To circumvent these linear scaling relations there needs to be a decoupling between the d-band center and the binding energies of the *COOH and *CO intermediates [3]. Implantation of p-block elements into Ag has emerged as a viable strategy to achieve this decoupling effect [4–6]. Of the p-block elements, Boron (B) has been widely utilized as a dopant in transition metals to produce stable catalysts with enhanced performance toward CO₂ reduction [7,8]. Recent work has also achieved a high uptake of B in Ag [9], with concentrations of 15 at%, showing good compatibility between the materials.

In this study, B was evaluated as a p-block element modifier in Ag through a combination of simulations and experiments. The simulations suggested that B could enhance the formation of CO by lowering the activation barrier of *COOH formation while weakening the binding

* Corresponding author.

E-mail address: kaiying.wang@usn.no (K. Wang).

<https://doi.org/10.1016/j.elecom.2023.107600>

Received 18 September 2023; Received in revised form 12 October 2023; Accepted 13 October 2023

Available online 14 October 2023

1388-2481/© 2023 The Authors. Published by Elsevier B.V. This is an open access article under the CC BY license (<http://creativecommons.org/licenses/by/4.0/>).

strength of *CO to facilitate rapid desorption from the Ag surface. The methodology developed for synthesizing Ag-B catalysts in this study shows that the incorporation of B in Ag through a magnetron co-sputtering process induces growth of highly textured Ag (1 1 1) films that exhibit 97.9% FE for the electrochemical reduction of CO₂ to CO. This is accompanied by a four-fold increase in the partial current density compared to pristine Ag. The unique nature of the co-sputtering process enables good control of the B content within the Ag films. Structural characterization reveals that the introduction of B into the crystal lattice of Ag induces twin boundary growth and gives rise to unique nanotentacle structures. The significant improvement in catalytic activity is attributed to a combined contribution of Ag (1 1 1) twin boundaries and incorporation of B, which lowers the activation barrier for *COOH formation.

2. Methods

2.1. DFT simulations

To investigate the effect of B heteroatoms and twin boundaries on the electrochemical CO₂ reduction mechanisms of Ag, an Ag (1 1 1), Ag-B (1 1 1) and TB-Ag slabs were built. DFT calculations of these slabs were computed by using a generalized gradient approximation (GGA) of exchange-correlation functional in the Perdew, Burke, and Ernzerhof (PBE). A plane-wave energy cut off of 400 eV was used together with norm-conserving pseudopotentials, and the Brillouin zone was sampled with a $2 \times 2 \times 1$ Monkhorst–Pack grid. The structure was fully optimized until the force on each atom was less than 10^{-3} eV/Å. To avoid periodic interaction, a vacuum layer of 30 Å was incorporated into the slabs. The free energy (ΔG) was computed from:

$$\Delta G = \Delta E + ZPE - T\Delta S \quad (1)$$

where ΔE was the total energy, ZPE was the zero-point energy, the entropy (ΔS) of each adsorbed state were yielded from DFT calculation, and ΔU was applied potential, whereas the thermodynamic corrections for gas molecules were taken from standard tables.

2.2. Catalyst synthesis

4" wafers of soda-lime glass were diced into 2.5×0.5 cm² pieces using a dicing saw (Disco DAD 3220). These samples were cleaned ultrasonically for 10 min in acetone using an ultrasonic cleaner before being rinsed in isopropanol. Next, the samples were loaded into a plasma cleaner, where they were subjected to 10 min of oxygen plasma at a power of 300 W with an Ar flow rate of 50 sccm and an O₂ flow rate of 100 sccm at 58 Pa. The samples were then loaded into the sputtering chamber that also contained an e-beam evaporation unit. First a 15 nm Cr layer was deposited using e-beam (current of 10–15 mA). Then, Ag was deposited using a DC power of 100 W while simultaneously depositing B with an RF power of 0–150 W at room temperature. The resulting films were approximately 1.7 μm thick.

2.3. Material characterization

Low angle XRD (Thermo Fisher Equinox 1000) equipped with a Cu-K α radiation source with a wavelength of 1.54 Å were used to obtain the XRD spectra. The surface morphology of the samples was investigated by FE-SEM (Hitachi SU 8230). XPS measurements and ion beam milling were performed using a Thermo Fisher ESCALAB 250Xi using a monochromatic Al X-ray source. Ion milling was performed using Ar ion energies of 0.5 and 2 keV. The TEM and STEM images were obtained at 200 kV using a FEI Titan Themis 200 TEM. The AFM measurements were conducted with a Park Systems XE-200 AFM in non-contact mode using an ACTA-200Si probe with a tip radius of <10 nm.

2.4. Electrochemical measurements

The electrochemical measurements were conducted with a CHI660E electrochemical workstation in a custom-made H-cell made of glass (Adams and Schittenden). A Nafion 117 proton exchange membrane separated the anodic and cathodic compartment, which were both filled with 75 mL of 0.5 M KHCO₃ electrolyte saturated with CO₂ (pH of 7.4). iR compensation was performed before each measurement by monitoring the resistance vs. the open circuit potential. All electrochemical measurements were performed in a three-electrode configuration using a Pt wire counter electrode and an Ag/AgCl (3 M KCl) reference electrode. The catalysts were tested at each potential for 20 min and fresh electrolyte was used for every catalyst. All catalysts were tested three times. Subsequently, all potentials were converted to the RHE scale using the Nernst equation:

$$E \text{ vs RHE} = E \text{ vs Ag/AgCl(3MKCl)} + 0.209V + 0.05916 \times pH \quad (2)$$

2.5. Product analysis and quantification

The gaseous reaction products were quantified using a Shimadzu-GC-2010 PLUS gas chromatograph (GC) equipped with a ShinCarbonST column and a dielectric-barrier discharge ionization detector (BID). The gas was sampled every 20 min with the setup connected in an on-line configuration [10]. The Faradaic efficiency (FE) was calculated using the formula in equation (3), where m is the number of moles of product derived from the GC measurement, n_x is the number of electrons required for reduction to product \times , F is Faraday's constant (96500C/mol), and Q is charge (C). In our case the charge was calculated as the time it takes to fill the sample loop multiplied by the current.

$$FE = \frac{m \cdot n_x \cdot F}{Q} \cdot 100 \quad (3)$$

3. Results and discussion

DFT simulations were performed to determine the effect of B on the catalytic performance of Ag. The Ag (1 1 1) surface was used in the simulations, with B placed interstitially into the lattice according to figure S1. An upshift in the d-band center (ϵ_d) towards the fermi level (E_f) of 0.24 eV is observed for the partial density of states (PDOS) with the addition of B (Fig. 1a-c). According to the d-band center theory, the bonding strength of an adsorbate to a transition metal surface is dictated by the filling of the bonding and antibonding states. Shifting of the d-band towards the fermi level (E_f) is accompanied by emptying of the antibonding states as they are forced above E_f . Therefore, the d-band center can rather accurately predict the bonding strength and interaction of an adsorbate at a transition metal surface, where a ϵ_d that is close to the E_f exhibits a stronger reactivity. Therefore, in the case of Ag, where the antibonding states are always filled, a stronger chemisorption can occur by reducing the filling of the antibonding states. Thus, the observed upshift should cause a stronger reactivity for Ag-B relative to the pristine Ag (1 1 1) surface. Next, we calculated the free energy profile for the two surfaces (Fig. 1d). In both slabs, the formation of *COOH is the rate determining step (RDS), but the B-doped Ag surface exhibits an activation barrier (E_a) of 1.33 eV, that is 0.25 eV lower than the pristine Ag (1 1 1) surface due to strengthening the *COOH binding. Thus, the stronger binding of *COOH to the Ag-B surface is in line with the observed shift in ϵ_d . Interestingly, *CO binds weaker to the Ag-B surface than the pristine Ag (1 1 1) by \sim 0.15 eV. A more rapid desorption of *CO is thus expected for the Ag-B catalyst. The destabilization of the *CO intermediate is interesting as it cannot be explained by the shift in the d-band center. However, the preferential stabilization of *COOH over *CO is consistent with the trend observed in high-throughput screening of p-block dopants in Ag [6]. The phenomenon has been attributed to a covalency-aided electrochemical reaction (CAER) mechanism, which

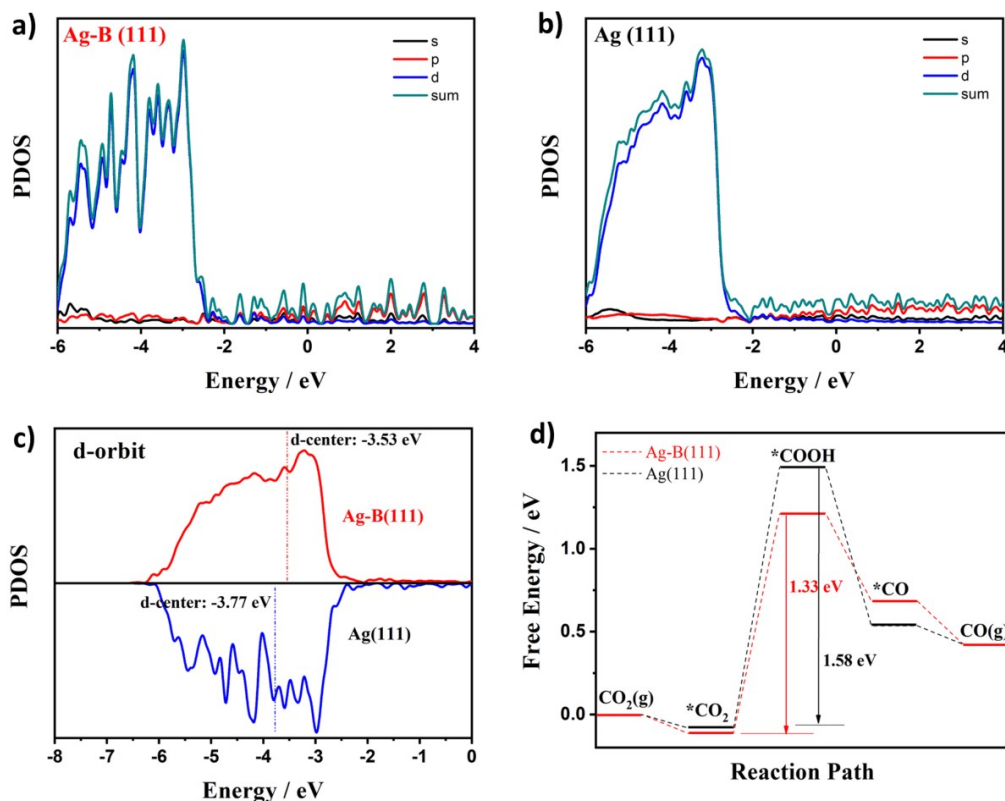


Fig. 1. Theoretical simulations for the B-doped Ag (111). PDOS for (a) Ag-B and (b) Ag (111), and (c) comparison of the d-band of the two structures. (d) Free energy diagram for Ag-B and Ag (111).

arise due to a difference in the σ -binding mechanisms between the COOH and CO intermediates. More precisely, the CO intermediate requires additional energy to form a covalent bond since it first needs to empty the p_z orbital of the dopant site. Based on the DFT simulations we determined that B was promising candidate for enhancing the electrocatalytic performance of Ag, and therefore proceeded to synthesize B-modified Ag catalysts.

Thin film catalysts ($\sim 1.7 \mu\text{m}$ film thickness) were synthesized through a co-deposition of Ag and B by magnetron sputtering as depicted in Fig. 2a. The B concentration was controlled by adjusting the RF power of the B target while keeping the DC power of the Ag target constant. Films with three different concentrations of B were made. These were labeled based on the RF power used for the B deposition as Ag (0 W), Ag-B-1 (100 W), and Ag-B-2 (150 W). The structural properties of the films were investigated by X-ray diffraction (XRD), with the respective patterns seen in Fig. 2b. The pristine Ag film displayed a polycrystalline FCC crystal structure, commonly obtained through magnetron sputtering deposition of metal films. However, the co-sputtering of B induced a significant increase in Ag (111) peak intensity while simultaneously reducing the intensity of other peaks. The Ag (111) peak intensified with increased B concentration and becomes totally dominant for the Ag-B-2 film. There were no peaks associated with the AgB_2 phase, which tend to be prevalent at $\sim 28^\circ$ [11]. Furthermore, it was observed that the Ag (111) peak shifts to lower angles (Fig. 2c) with increasing concentrations of B, suggesting that B causes an expansion of the lattice. To understand the transformation in crystal structure, a set of scanning transmission electron microscopies (STEM) and high-resolution transmission microscopy (HRTEM) were performed on the Ag-B-2 film (Fig. 2d). The cross-sectional images show densely stacked columnar

grains aligned in the growth direction. HRTEM performed on these columns reveals a high density of 5–10 nm wide Ag (111) coherent twin boundaries (TB) aligned perpendicular to the growth direction. The lattice spacing is measured to be 2.385 Å, which is larger than the expected value for Ag (111) of ~ 2.360 Å. The selected area electron diffraction (SAED) shows a spotted pattern, which is indicative of a single crystal structure. Additionally, the pattern consists of duplicate points, which is a characteristic of twinned crystals [12]. Thus, the co-deposition of B facilitates Ag (111) TB growth, whose numbers increase with increasing B concentration, and is visible by a dominant Ag (111) peak in the XRD spectra. Growth of TB's is highly related to the stacking fault energy (SFE) [13], where metals exhibiting a low SFE tend to form TBs more easily. While Ag is one of the FCC metals with the lowest SFE, the formation of TBs through sputter deposition is usually only observed for epitaxially grown Ag [14]. In contrast, by adding metals and in some cases non-metals to Ag in low concentrations [15], a further reduction in the SFE can be achieved. It is therefore likely that B reduced the SFE of Ag, which favored the observed formation of TB's.

The surface morphology of the films can be seen in Fig. 2e. A granular structure, with ~ 100 nm wide grains is observed for the pristine Ag film. Introduction of boron gives rise to tentacle structures, with each tentacle being approximately 30–50 nm wide and 100–200 nm long. A mixture of tentacles and grains is attained for the Ag-B-1 film, whereby a full transition into tentacle structures is observed for the Ag-B-2 film. Atomic force microscopy (AFM) was used to gain information about the surface topography. The AFM images display a film morphology that is identical to the SEM images (figure S2) and shows an increase in roughness when B is introduced into the films, from ~ 7.2 nm for the Ag film to 12.0 nm for Ag-B-2 film. However, there is only a minor

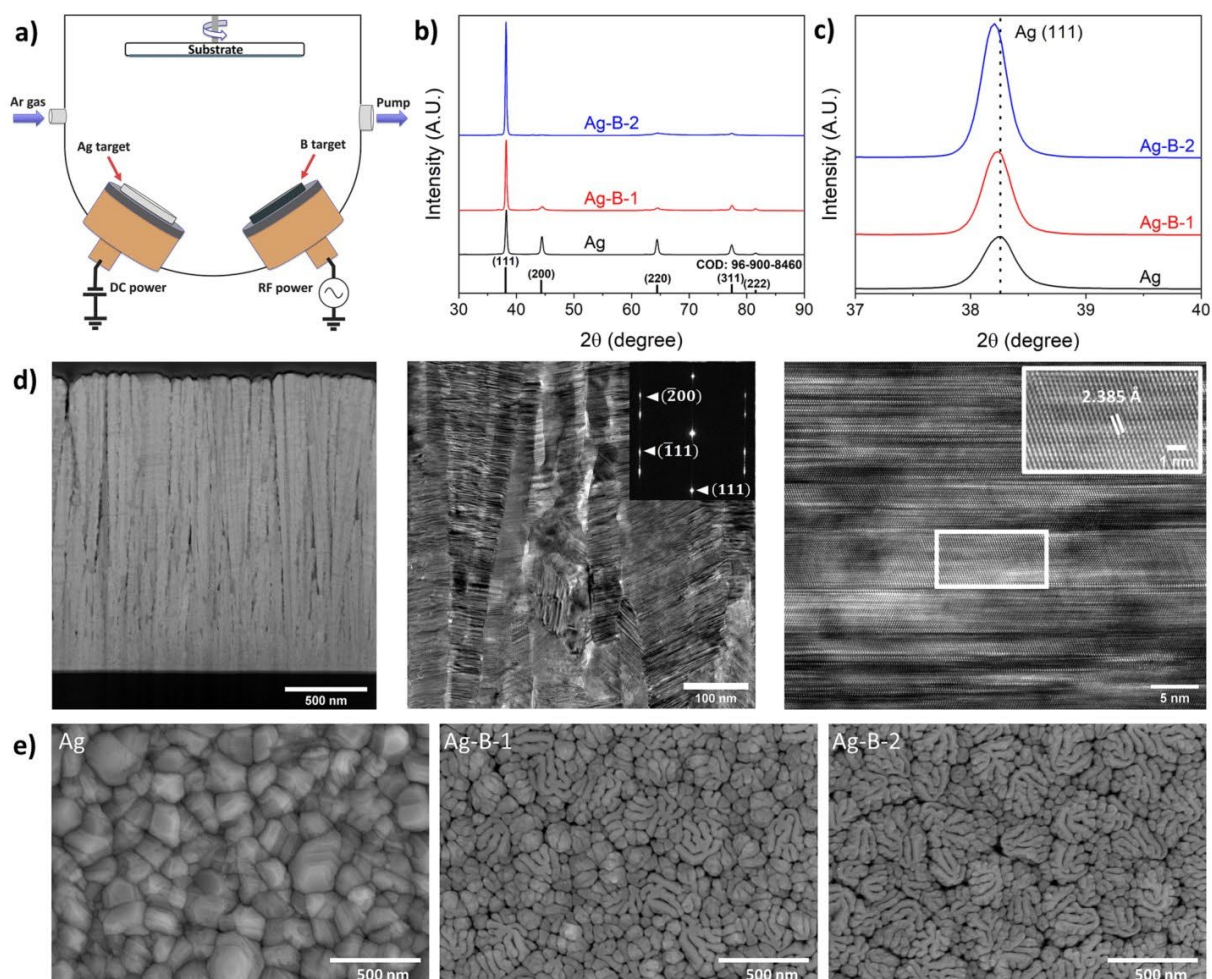


Fig. 2. Synthesis and structural characterization of the Ag-B films. (a) Schematic of the sputtering setup. (b)-(c) XRD spectra of the films. (d) STEM and HRTEM of the Ag-B-2 sample. (e) SEM images of the films.

difference in roughness between the Ag-B-1 and Ag-B-2 films (<1 nm).

X-ray photoelectron spectroscopy (XPS) and Auger electron spectroscopy (AES) were performed to gain insight into the chemical structure of the films. The XPS spectra display strong peaks for Ag3d (Fig. 3a), and the B1s peak is found at ~ 188 eV for Ag-B-1 and Ag-B-2 (Fig. 3b). According to the XPS data, the atomic ratio of B/Ag was 7 at% for Ag-B-1 and 19 at% for Ag-B-2. While a positive peak shift of ~ 0.2 eV is detected for the Ag-B films relative to the pristine Ag film (Fig. 3c), the shift correlates with the difference in oxygen concentration at the surface, which was found to be 38.3, 14.6, and 25.2 at% for the Ag, Ag-B-1, and Ag-B-2 samples, respectively. Attempts at removing approximately 200 nm of the top surface layers by ion milling prior to the XPS measurements yielded no B1s peak for any of the samples. AES performed on two different points of the Ag-B-2 film gave a B to Ag concentration of 28 and 25 at% (Fig. 3d), which is higher than that obtained from the XPS. These values were reduced to 12 and 0 at% respectively following ion milling of the samples for 6 s and 18 s prior to the measurement (figure S3). Due to the nature of the co-sputtering process used to synthesize the films, it is expected that B is evenly distributed throughout the material. Thus, it is highly unlikely that the B is primarily located near the top surface, which could be interpreted from the XPS and AES measurements following the ion milling. Instead, a difference in the sputtering yield for

the elements could explain the disappearance of B after ion milling. This could further be exacerbated due to the existence of TB's, which can strengthen the mechanical properties of Ag, and potentially reduce its sputtering yield further. In fact, the preferential removal of B from ion milling has previously been observed for various transition metal borides, where increasing the Ar⁺ energy was shown to promote this effect [16]. However, reducing the Ar⁺ energy of the ion beam from 2 keV to 0.5 eV did not make any noticeable changes, and the B1s peak remained undetectable.

The catalytic performance of the catalysts towards the electrochemical CO₂ reduction was evaluated in an H-cell, with all potentials referenced to a reversible hydrogen electrode (RHE). The tests were conducted in the potential range from -0.6 to -1.0 V, where the analysis of the gaseous reaction products showed that the catalysts mainly produced CO and H₂. The FE(CO) obtained at each potential can be seen in Fig. 4a. The pristine Ag catalyst displays a gradual increase in FE(CO) as the potential increases, reaching a peak FE(CO) of 86.5% at -1.0 V. In the potential range of -0.6 V to -0.7 V the FE(CO) is below 30% for Ag, but nearly doubles as the potential reaches -0.8 V. The Ag-B-1 catalyst show a similar behavior, but generally exhibit higher FE(CO) than Ag. On the other hand, the Ag-B-2 catalyst shows much higher selectivity towards CO at lower overpotentials, with four times the FE

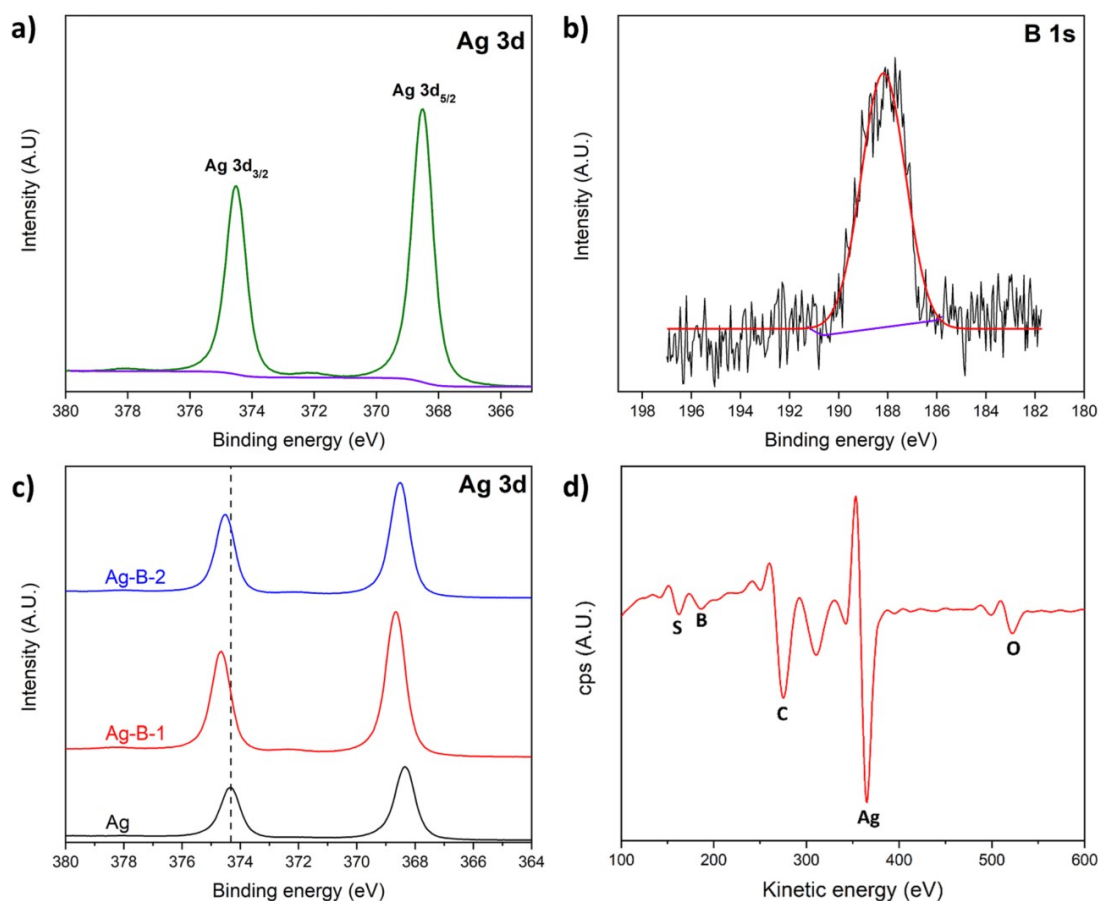


Fig. 3. Characterization of the chemical properties of the films. XPS spectra obtained from the Ag-B-2 sample with (a) Ag3d and (b) B1s. (c) Ag3d XPS spectra of the films. (d) AES spectrum of the Ag-2-B sample.

(CO) of Ag at -0.6 V, while achieving a $FE(CO)$ of $\sim 79\%$ at -0.7 V. Moreover, the $FE(CO)$ reaches 97.9% at -0.9 V, considerably higher compared to Ag, which attains 79% at the same potential. Fig. 4b shows the CO partial current density (J_{CO}) for the catalysts, where an increase in J_{CO} can be seen the Ag-B catalysts. A substantial increase in J_{CO} is seen for Ag-B-2 at all potentials compared to the Ag catalyst. At -0.9 V the Ag-B-2 catalyst exhibits a J_{CO} of -5.6 mA/cm², more than 4 times that of the Ag catalyst (-1.3 mA/cm²). Next, we tested the stability of the Ag-B-2 catalyst by extending the reaction period to ten hours at a potential of -0.9 V. The $FE(CO)$ and current density were plotted as a function of time (Fig. 4c), showing a $FE(CO)$ close to 98% for the first six hours, whereas a slight decline and instability is observed, but the $FE(CO)$ remains above 90% for the entirety of the test. Similarly, a slight decrease in current density is observed over time, but this can be explained by water evaporation due to the continuous flow of CO₂, which reduced the liquid level in the glass cell and hence the effective surface area of the catalyst that was in contact with the solution.

Since the increase in B concentration is accompanied by a change in morphology and crystal structure, it makes it hard to pinpoint the main contributing factor to the observed enhancement in catalytic activity. However, based on previous studies on single crystals, Ag (111) should exhibit the largest activation barrier (E_a) for *COOH formation compared to Ag (100) and Ag (110) [17]. Therefore, we reason that the presence of Ag (111) is not responsible for the observed improvement. However, the Ag-B-2 catalyst show a significant number of coherent

twin boundaries, which have been identified as important active sites for CO₂ reduction for both Cu and Ag [12,18]. We therefore employed DFT simulations to determine the effect of these TB's using a model consisting of a single coherent Ag (111) TB (figure S4). The free energy profile (Fig. S4b) shows that the formation of *COOH remains the RDS, but the E_a is decreased from 1.58 eV to 1.37 eV for TB-Ag. While *COOH exhibits a stronger binding on TB-Ag (1.094 eV) than Ag-B (1.216 eV), the E_a for *COOH formation is slightly higher on TB-Ag by 0.04 eV due to strengthening the binding of *CO₂. Furthermore, the desorption of *CO does not readily occur for TB-Ag as *CO binds stronger on TB-Ag than on the pristine Ag (111) surface by ~ 0.27 eV, making the desorption of *CO have a barrier of 0.16 eV. In general, all the intermediates bind stronger to the TB-Ag surface compared to the pristine Ag (111), displaying dependence of the linear scaling relations. From these findings the TBs should be beneficial for the electrochemical CO₂ reduction to CO. Therefore, considering the collective contribution of B and TB's, it is reasonable to assume that the activation barrier for *COOH formation will be reduced for the Ag-B-2 catalyst, since both the TB's and the incorporation of B strengthens the binding of *COOH. On the other hand, *CO binds stronger on TB-Ag and weaker on Ag-B relative to the pristine Ag (111), which could suggest that their combined contribution could leave the binding strength of *CO relatively unaffected. Additionally, the catalyst benefits from the enhanced adsorption of CO₂ observed on the TB's. Thus, introduction of B into the Ag effectively allows for strengthening the binding energy of the *COOH

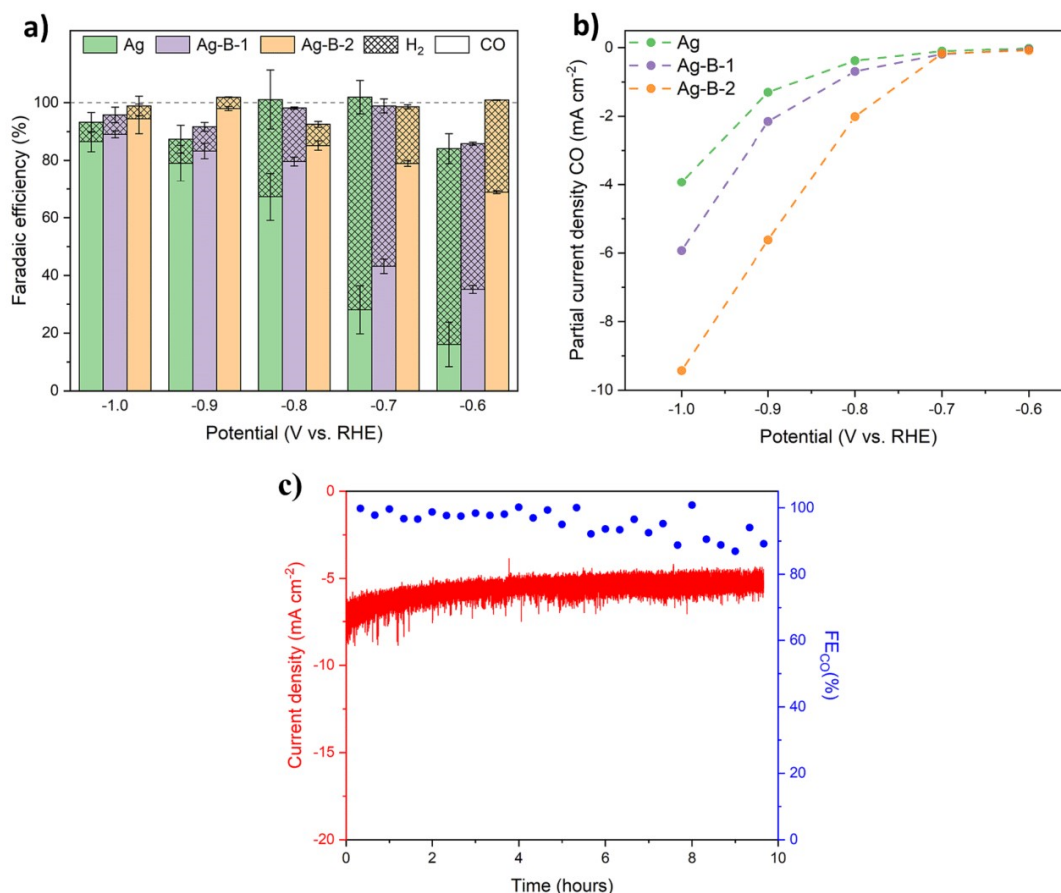


Fig. 4. Electrochemical characterization of the Ag-B catalysts. (a) Faradaic efficiency as a function of applied potential. (b) CO partial current density, and (c) stability test conducted at -0.9 V vs. RHE for the Ag-B-2 catalyst.

intermediate independent of *CO and thereby circumventing the scaling relations.

4. Conclusion

In summary, we have investigated the use of B as a modifier in Ag for the purpose of enhancing the electrochemical reduction of CO₂ to CO. Theoretical simulations show that the introduction of B into the Ag lattice can lower the activation barrier for *COOH formation while simultaneously reducing the binding strength of *CO to allow for rapid desorption. Thin film Ag-B catalysts were synthesized through a magnetron co-sputtering process, where the incorporation of B facilitated the growth of coherent Ag (111) twin boundaries due to lowering the SFE, leading to highly textured Ag (111) films. The surface morphology, as revealed by SEM, undergoes drastic changes when increasing the B concentration, from granular to unique nano-tentacles structures. These Ag-B catalysts exhibit considerably improved catalytic properties for electrochemical CO₂ reduction, with a faradaic efficiency of 97.9% for CO at -0.9 V vs. RHE. The unique ability to increase the binding strength of *COOH while destabilizing *CO offers a potent strategy for the development of highly selective catalysts for the electrochemical reduction of CO₂.

CRedit authorship contribution statement

Kim Robert Gustavsen: Conceptualization, Methodology,

Investigation, Visualization, Writing – original draft. Hao Huang: Methodology, Software, Visualization. Erik Andrew Johannessen: Supervision, Writing – review & editing. Kaiying Wang: Supervision, Funding acquisition, Writing – review & editing.

Declaration of Competing Interest

The authors declare that they have no known competing financial interests or personal relationships that could have appeared to influence the work reported in this paper.

Data availability

Data will be made available on request.

Acknowledgements

The authors K.R.G. and K.W. acknowledge the research grants from EEA (European Economic Area)-Norway-Romania project #Graftid, RO-NO-2019-0616 and EEA-Poland-NOR/POLNORCCS/ PhotoRed/0007/2019-00. K.R.G. acknowledge support from the Norwegian Micro- and Nano- Fabrication Facility (NorFab, No. 245963/F50) and the strategic research plan of the University of South-Eastern Norway. The author H. H. acknowledges Marie Skłodowska-Curie Actions individual fellowship CarbonChem 101024758.

Appendix A. Supplementary data

Supplementary data to this article can be found online at <https://doi.org/10.1016/j.elecom.2023.107600>.

References

- [1] A. Bagger, W. Ju, A.S. Varela, P. Strasser, J. Rossmeisl, Electrochemical CO₂ Reduction: A Classification Problem, *ChemPhysChem* 18 (2017) 3266–3273.
- [2] Y. Zhang, L. Liu, L. Shi, T. Yang, D. Niu, S. Hu, X. Zhang, Enhancing CO₂ electroreduction on nanoporous silver electrode in the presence of halides, *Electrochim. Acta* 313 (2019) 561–569.
- [3] F. Calle-Vallejo, D. Loffreda, M.T.M. Koper, P. Sautet, Introducing structural sensitivity into adsorption–energy scaling relations by means of coordination numbers, *Nat. Chem.* 7 (2015) 403–410.
- [4] S. Liu, H. Tao, Q. Liu, Z. Xu, Q. Liu, J.-L. Luo, Rational Design of Silver Sulfide Nanowires for Efficient CO₂ Electroreduction in Ionic Liquid, *ACS Catal.* 8 (2018) 1469–1475.
- [5] J. Gao, C. Zhu, M. Zhu, Y. Fu, H. Huang, Y. Liu, Z. Kang, Highly Selective and Efficient Electroreduction of Carbon Dioxide to Carbon Monoxide with Phosphate Silver-Derived Coral-like Silver, *ACS Sustain. Chem. Eng.* 7 (2019) 3536–3543.
- [6] H.-K. Lim, H. Shin, W.A. Goddard, Y.J. Hwang, B.K. Min, H. Kim, Embedding Covalency into Metal Catalysts for Efficient Electrochemical Conversion of CO₂, *J. Am. Chem. Soc.* 136 (2014) 11355–11361.
- [7] Y. Zhou, F. Che, M. Liu, C. Zou, Z. Liang, P. De Luna, H. Yuan, J. Li, Z. Wang, H. Xie, H. Li, P. Chen, E. Bladt, R. Quintero-Bermudez, T.-K. Sham, S. Bals, J. Hofkens, D. Sinton, G. Chen, E.H. Sargent, Dopant-induced electron localization drives CO₂ reduction to C₂ hydrocarbons, *Nat. Chem.* 10 (2018) 974–980.
- [8] C. Chen, X. Sun, L. Lu, D. Yang, J. Ma, Q. Zhu, Q. Qian, B. Han, Efficient electroreduction of CO₂ to C₂ products over B-doped oxide-derived copper, *Green Chem.* 20 (2018) 4579–4583.
- [9] Y. Li, H. Yu, Z. Wang, S. Liu, Y. Xu, X. Li, L. Wang, H. Wang, Boron-doped silver nanosponges with enhanced performance towards electrocatalytic nitrogen reduction to ammonia, *Chem. Commun.* 55 (2019) 14745–14748.
- [10] K.R. Gustavsen, E.A. Johannessen, K. Wang, Sodium Persulfate Pre-treatment of Copper Foils Enabling Homogenous Growth of Cu(OH)₂ Nanoneedle Films for Electrochemical CO₂ Reduction, *ChemistryOpen* 11 (2022) e202200133.
- [11] J. Pelleg, M. Rotman, M. Sinder, Borides of Ag and Au prepared by magnetron sputtering, *Physica C* 466 (2007) 61–64.
- [12] C. Tang, P. Gong, T. Xiao, Z. Sun, Direct electrosynthesis of 52% concentrated CO on silver's twin boundary, *Nat. Commun.* 12 (2021) 2139.
- [13] D.C. Bufford, Y.M. Wang, Y. Liu, L. Lu, Synthesis and microstructure of electrodeposited and sputtered nanotwinned face-centered-cubic metals, *MRS Bull.* 41 (2016) 286–291.
- [14] D. Bufford, H. Wang, X. Zhang, High strength, epitaxial nanotwinned Ag films, *Acta Mater.* 59 (2011) 93–101.
- [15] L. Velasco, A.M. Hodge, The mobility of growth twins synthesized by sputtering: Tailoring the twin thickness, *Acta Mater.* 109 (2016) 142–150.
- [16] G. Greczynski, L. Hultman, Towards reliable X-ray photoelectron spectroscopy: Sputter-damage effects in transition metal borides, carbides, nitrides, and oxides, *Appl. Surf. Sci.* 542 (2021), 148599.
- [17] E.L. Clark, S. Ringe, M. Tang, A. Walton, C. Hahn, T.F. Jaramillo, K. Chan, A. T. Bell, Influence of Atomic Surface Structure on the Activity of Ag for the Electrochemical Reduction of CO₂ to CO, *ACS Catal.* 9 (2019) 4006–4014.
- [18] C. Tang, J. Shi, X. Bai, A. Hu, N. Xuan, Y. Yue, T. Ye, B. Liu, P. Li, P. Zhuang, J. Shen, Y. Liu, Z. Sun, CO₂ Reduction on Copper's Twin Boundary, *ACS Catal.* 10 (2020) 2026–2032.

Patent

Gustavsen, K.R, Wang, K. (2022). Process for producing single crystal films. Norwegian Industrial Property Office, Pat. No. 347559.



(12) PATENT

(11) 347559

(13) B1

NORWAY

(19) NO

(51) Int Cl.

C23C 14/06 (2006.01)

C23C 14/14 (2006.01)

C23C 14/16 (2006.01)

C23C 14/18 (2006.01)

C23C 14/20 (2006.01)

C23C 14/22 (2006.01)

C23C 14/34 (2006.01)

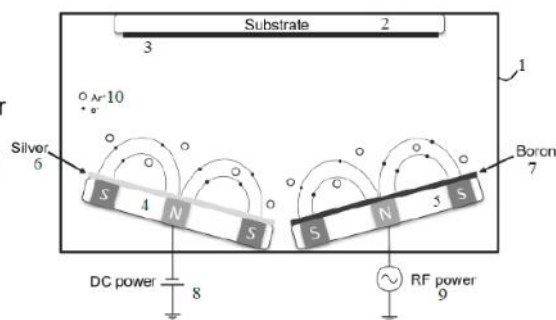
C23C 14/35 (2006.01)

Norwegian Industrial Property Office

(21)	Application nr.	20220708	(86)	International Filing Date and Application Number
(22)	Date of Filing	2022.06.21	(85)	Date of Entry into National Phase
(24)	Date of Effect	2022.06.21	(30)	Priority
(41)	Publicly Available	2023.12.22		
(45)	Granted	2024.01.15		
(73)	Proprietor	University of South-Eastern Norway, Postboks 4, 3199 BORRE, Norge		
(72)	Inventor	Kim Robert Gustavsen, c/o University of South-Eastern Norway Forskningsparken, Instituttet for mikrosystemer, Postboks 4, 3199 BORRE, Norge		
(74)	Agent or Attorney	Kaiying Wang, c/o University of South-Eastern Norway, Raveien 215, 3184 BORRE, Norge BRYN AARFLOT AS, Stortingsgata 8, 0161 OSLO, Norge		

(54)	Title	PROCESS FOR PRODUCING SINGLE CRYSTAL SILVER FILMS
(56)	References Cited:	JP H04116163 A Joshua Pelleg et al., Borides of Ag and Au prepared by magnetron sputtering, Physica C466 (2007) 61-64. Oren Metz et al., Ag-B Thin Films Prepared by Magnetron Sputtering, Mater. Res. Soc. Symp. Proc Vol. 848, 2005 Material Science Society. US 2006182883 A1, WO 2009145461 A3
(57)	Abstract	

This invention relates to a process and processing unit for deposition of single crystal silver thin films on a substrate, the process involving a sputtering method for depositing silver on a substrate using a DC sputtering method, wherein the process also includes a RF powered boron deposition, the RF and silver deposition being performed simultaneously.



PROCESS FOR PRODUCING SINGLE CRYSTAL SILVER FILMS

- 5 The present invention is related to the production of single crystal thin film, especially silver thin films using sputtering techniques.

Single crystal metal thin films are highly desirable for their unique material properties in microelectronics and for optical application due to the surface plasmonic resonance effect. Silver is considered to be the best plasmonic metal at optical and near infrared frequencies. However, the surface plasmonic resonance must be manipulated for the application in devices. Such manipulation is often accomplished by patterning the metal layer by a focused-ion-milling (FIB). Unfortunately, FIB is an anisotropic process where each crystal plane etches away at different rates, giving rise to increased roughness and large surface irregularities, significantly increasing loss due to surface plasmonic scattering. Therefore, to ensure precise patterning, single crystal silver thin films are ideal as it provides a uniform etch rate across the film surface.

20

The growth of single crystal silver thin films is challenging and requires stringent growth conditions, and often lacks thickness control, which is crucial for plasmonic devices. Usually, single crystal silver thin films are attained by epitaxial growth. Epitaxial growth is where a single crystal thin film is achieved by depositing the desired material onto a specific substrate or seed-layer of a certain crystal orientation. Typical deposition methods for epitaxial growth are molecular beam epitaxy (MBE), atomic layer deposition (ALD), and epitaxial chemical vapour deposition (CVD), where the deposition rates are very low, limiting the attainable film thickness. Successful single crystal silver thin film growth has been achieved by DC sputtering and high deposition rate e-beam, but similar to the forementioned techniques it uses epitaxial growth, where a

specified substrate or seed-layer is needed, and where substantial substrate temperature is required during growth or when post-annealing. Japanese patent application JPH04116163 describes an example of a method for producing a single crystal silver film by ion beam sputtering on a Si or Mg substrate.

5

In this invention, a process is described for deposition of single crystal silver thin films using magnetron sputtering at room temperature that differs from conventional epitaxial growth. Magnetron sputtering is a physical vapor deposition (PVD) technique that similar to regular sputtering utilizes plasma to deposit a material onto a substrate. It differs from traditional sputtering, by employing magnets which traps the electrons from the local electric field near the target surface, thereby significantly increasing the deposition rate. Sputtering is generally used for depositing polycrystalline metal thin films but can also deposit thin films of insulators or other compounds by RF power.

15

Magnetron sputtering is an industrial tool capable of large-scale fabrication and is not limited in terms of substrate size. It has relatively high deposition rate compared to the epitaxial growth methods and can be easily scaled up for large-scale production. Without the requirement of a specific substrate and with single crystal growth being attainable at room temperature, it makes it an ideal process for microfabrication, meaning that it is compatible with microelectronics for instance for optical devices. Another big advantage is that the single crystal films are continuous over the entire substrate, in our case over a 4" wafer, but the process should be easily scalable to 6" wafers.

25 It is also known that co-sputtering of different materials may be used to produce films of different compositions such as silver-boron-films, as is described in Oren Metz et al: "Ag-B Thin Films Prepared by Magnetron Sputtering", Mater. Res. Soc. Symp. Proc Vol. 848, 2005 Material Science Society. The article applies RF power to both the B and Ag target (we use DC for Ag). In addition, 30 the power applied to the silver target is very low (20W) combined with a very high power for the B target (300W). The resulting films therefore contains high concentration of B, giving the AgB₂ phase.

Another example of the prior art is discussed in Joshua Pelleg et al: Borides of Ag and Au prepared by magnetron sputtering", Physica C 466 (2007) 61-64. In this paper they apply DC power to Ag and RF power to B similarly to our
5 method. The DC power is in the range of 20-30W, and the RF power is set to 300W. The Boron concentration is very high compared to the silver (see table 1).

Single crystal silver thin films are highly attractive for optical, bio-catalytic,
10 biological, and plasmonic applications. However, growing single crystal silver thin films with a high degree of thickness control and with a high deposition rate remains a challenge. Sputtering technology is a method that can provide moderately high deposition rate relative to other methods used for growing single crystal silver films; however, depositing single crystal silver through
15 sputtering deposition, like other epitaxial deposition methods, has required a specific substrate material with a designated crystal orientation together with a high substrate temperature (>350°C). These requirements have limited the application of sputtered single crystal silver thin films, as the substrate material, crystal orientation, or substrate temperature during deposition might not be
20 compatible with the microfabrication process.

The present invention is aimed at providing catalyst materials for the electrochemical reduction of CO₂ into fuels, specifically the present invention is aimed at producing single crystal silver film on a substrate. The objectives of the
25 invention are achieved as specified in the accompanying claims.

The objectives of the invention are thus achieved by using magnetron sputtering to synthesize metal thin-films with controllable concentration of impurities through an RF-assisted DC sputtering process. The sputtering process may be
30 based on a confocal sputtering configuration as discussed in Hyon-Jong Kim, et al, "High-throughput analysis of thin-film stresses using arrays of micromachined cantilever beams", Review of Scientific Instruments 79, 045112

(2008). DOI:10.1063/1.2912826 In this way a process of depositing single crystal silver thin films has been provided that is not substrate-dependent, without thickness limitations, and can be synthesized at room temperature.

- 5 The invention will be described below with reference to the accompanying drawings, illustrating the invention by way of examples.

Fig. 1 illustrates the sputtering system producing according to the invention.

Figs 2a-2c shows the properties of the produced material.

10

As is schematically illustrated in figure 1 the system according to the invention and/or for performing the invention comprises a chamber 1 containing an Ar⁺/e⁻ atmosphere as is well known in the field. A substrate 2 is provided in the chamber. The substrate may be of any suitable material, especially Si (100), Si
15 (110), Si (111), ITO, soda-lime glass, chromium, or quartz.

As is shown the invention utilizes two source materials 6,7 in a confocal sputtering arrangement, being constituted by a silver target and a Boron target, respectively. According to the invention the silver sputtering unit 4 is connected
20 to a DC power source 8 driven at a predetermined voltage, while the boron sputtering unit 5 is driven by an RF source 9 driven at a chosen voltage and frequency. Using this, both silver and boron will be deposited at the substrate. . The distances from the targets 6,7 to the substrate 2 may depend on the chosen parameters in the range of 5 - 50 cm and the angle of the targets
25 relative to the substrate may be in the range of 15 – 75 degrees.

According to a first example, single crystal silver growth from room temperature to 400°C is accomplished at the following substrates: Si(100), Si(110), Si(111), Indium Tin Oxide (ITO) glass, soda-lime glass, and chromium. There are no
30 clear limitations on the film thickness, with single crystal growth observed in the range of 25 – 2000 nm. Furthermore, a deposition has been achieved at a rate

of ~17 nm/min, which is significantly higher than alternative methods for single crystal silver growth such as MBE and ALD. Thus, the method for single crystal growth of silver is independent of the substrate and deposition temperature.

- 5 The invention provides a method or process for depositing single crystal silver thin films by utilizing an RF-assisted DC sputtering process where silver is deposited using DC power and boron is introduced using an RF power source to facilitate single crystal growth of silver. The morphology and the ratio of crystal orientation can be controlled by adjusting deposition parameters such as
- 10 DC and RF power, chamber pressure, and substrate temperature.

According to a preferred embodiment of the invention the coating layers are

15 deposited using a magnetron sputtering system in a RF-assisted DC sputtering procedure where silver is deposited using DC power and boron is simultaneously introduced using an RF power source as illustrated in figure 1. Increasing the RF power of the boron target changes the crystal structure of the deposited silver thin film from polycrystalline to single crystal. The RF power

20 density of the boron target can be tuned in the range of 0-6.6 W/cm², where >3.3 W/cm² gives full conversion into a single crystal structure. The RF frequency will typically be 13.56 MHz. The DC power density applied to the silver target was 4.9 W/cm² for the fully converted thin films. During the growth, a sputtering gas is introduced at a controlled flow rate to achieve a chamber

25 pressure in the range of 0.52-0.65 Pa. Single crystal silver coating layers are attainable at room temperature and does not require the substrate to be heated during deposition. The process has been verified for deposition onto various substrates, such as Si(100), Si(110), Si(111), soda-lime glass, and indium-tin-oxide (ITO) glass, both with and without a Cr adhesion layer.

30

The resulting material has properties as illustrated in figures 2a-2c.

Figure 2a illustrates the X-ray diffraction (XRD) used to determine the crystal structure of the silver coating layers. The samples deposited using RF power density of 3.3 W/cm^2 yields single crystal structure with a dominant Ag (111) peak. The morphology of the samples was investigated using a field-effect scanning electron microscope (FE-SEM). A granular structure was observed for the pure Ag films, whereas a gradual change in the morphology was achieved when increasing the RF power, resulting in a 'nano-brain' or tentacle-like structure, as shown in figure 2b, at a RF power density of 3.3 W/cm^2 . The growth mechanism was investigated using high-resolution transmission electron microscope (HRTEM). Highly ordered growth of the silver film with a high density of twin boundaries was observed, one such twin boundary is shown in figure 2c. The lattice spacing is measured to be $\sim 2.385 \text{ \AA}$, slightly in the higher range of the expected value for silver (111), indicating a strained lattice. Twinned growth usually occurs for epitaxial growth using very high deposition rates in DC sputtering. However, twin boundaries tend to form when there is substantial amount of stress and strain in the lattice during or following the deposition process, which in our case could occur due to the incorporation of boron. Furthermore, the Fast Fourier Transform (FFT) image of one sidewall of the twin boundary (figure 2c inset) shows a pattern indicating existence of single crystal structure.

To summarize, the present invention relates to a process or processing method for deposition of single crystal silver thin films on a substrate. The process involves a sputtering method for depositing silver on a substrate using a DC sputtering method and simultaneously a RF powered boron deposition, where the sputtering depositions are preferably performed with per se known confocal magnetron sputtering arrangements.

According to a preferred embodiment of the invention the substrates are heated in the range of $20\text{-}400^\circ\text{C}$ during deposition. The DC power applied in the silver deposition may preferably be varied in the range of $2.45\text{-}7.35 \text{ W/cm}^2$, and the RF power in the boron deposition may preferably be varied in the range of $1.1\text{-}6.6 \text{ W/cm}^2$. The sputtering gas is preferably used to control the chamber

pressure in the range of 0.27 - 2.67 Pa and may be introduced with flow rates in the range of 5-30 cm³/s (standard conditions 0°C and 1.013 bar).

The parameters mentioned above, i.e. chamber pressure, DC and RF powers
5 may be adjusted to provide deposition rates of 1.2 – 20 nm/min.

The target to substrate distance may be varied in the range of 5 - 50 cm and the targets angle to the substrate is varied in the range of 15 – 75 degrees.

10 Preferably the single crystal silver films grown using the process on a substrate constituted by Si (100), Si (110), Si (111), ITO, soda-lime glass, chromium, or quartz.

Thus, the processing unit according to the invention preferably includes a
15 chamber containing an argon ion atmosphere and a substrate configured to receive the film, the unit also including a silver coated sputtering unit being driven by a DC power source and a boron sputtering unit driven by an RF power source. As stated above the processing unit is configured to heat the substrate during deposition to a temperature in the range of in the range of 20-400°C, the
20 DC power preferably in the range of 2.45-7.35 W/cm² and the RF power may be in the range of 1.1-6.6 W/cm². The pressure in the chamber being in the range of 0.267 - 2.666 Pa and may be introduced with flow rates in the range of 5-30 cm³/s. The target to substrate distance may be varied in the range of 5 - 50 cm and the targets angle to the substrate is varied in the range of 15 – 75 degrees.

25

Claims

1. A process for deposition of single crystal silver thin films on a substrate,
characterised in that the process involves a sputtering method for depositing
5 silver on a substrate using a DC sputtering method, and wherein the process
also includes a RF powered boron deposition, the RF and silver deposition
being performed simultaneously.
2. The process in claim 1 where the substrates in claim 1 are heated in the
range of 20-400°C during deposition.
- 10 3. The process in claim 1 where the DC power is varied in the range of
2.45-7.35 W/cm²
4. The process in claim 1 where RF power is varied in the range of 1.1-6.6
W/cm²
5. The process in claim 1 where the sputtering gas is used to control the
15 chamber pressure in the range of 0.267 - 2.666 Pa.
6. The process in claim 1 where the sputtering gas is introduced with flow
rates in the range of 5-30 cm³/s.
7. The process in according to the preceding claims 3, 4 and 5, where the
parameters in claims 3, 4 and 5 are varied to achieve deposition rates of 1.2 –
20 20 nm/min
8. The process in claim 1 where the target to substrate distance is varied in
the range of 5 - 50 cm.
9. The process in claim 1 where the targets angle to the substrate is varied
in the range of 15 – 75 degrees.
- 25 10. Processing unit for processing a single crystal silver thin film comprising
a chamber containing an argon ion atmosphere and a substrate configured to
receive the film,
characterised in that the unit also includes a silver sputtering target being
driven by a DC power source and a boron sputtering target driven by an RF
30 power source.

Patentkrav

1. En prosess for deponering av en en-krystall sølv-tynnfilm på et substrat,
karakterisert ved at prosessen involverer en sputtering-metode for deponering
5 av sølv på et substrat ved bruk av en DC sputtering-metode, og hvori prosessen
også inkluderer en RF-drevet bor-sputtering, der RF og sølv-deponeringen
utføres samtidig.
2. Prosessen ifølge krav 1, hvori substratet i krav 1 er er varmet opp til i
området 20-400°C under deponeringen.
- 10 3. Prosessen ifølge krav 1, hvori DC kraften varierer innen området 2,45-
7,35 W/cm²
4. Prosessen ifølge krav 1, der RF kraften varieres innen området 1,1-6,6
W/cm²
5. Prosessen ifølge krav 1, der sputtering-gassen brukes for å kontrollere
15 kammertrykket i området 0,267 – 2,666 Pa.
6. Prosessen ifølge krav 1, der sputtering-gassen introduseres med
strømningsrate i området 5-30 cm³/s.
7. Prosessen ifølge et av de foregående kravene 3, 4 og 5, der
parametrene i kravne 3, 4 og 5 varieres for å oppnå deponeringsrate på 1,2-
20 200nm/min
8. Prosessen ifølge krav 1, der mål til substrat-avstand varieres innen
området 5 - 50 cm.
9. Prosessen ifølge krav 1, der målets vinkel i forhold til substratet varieres
innen området 15 – 75 grader.
- 25 10. Prosesseringsenhet for prosessering av en enkelt-krystall sølv-film
omfatter et kammer inneholdende en argon-ione atmosfære og et substrat
konfigurert til å motta filmen,
karakterisert ved at enheten også omfatter et sølv-sputtering-mål drevet av en
DC kraftkilde og et bor-sputtering-mål drevet av en RF kraftkilde.

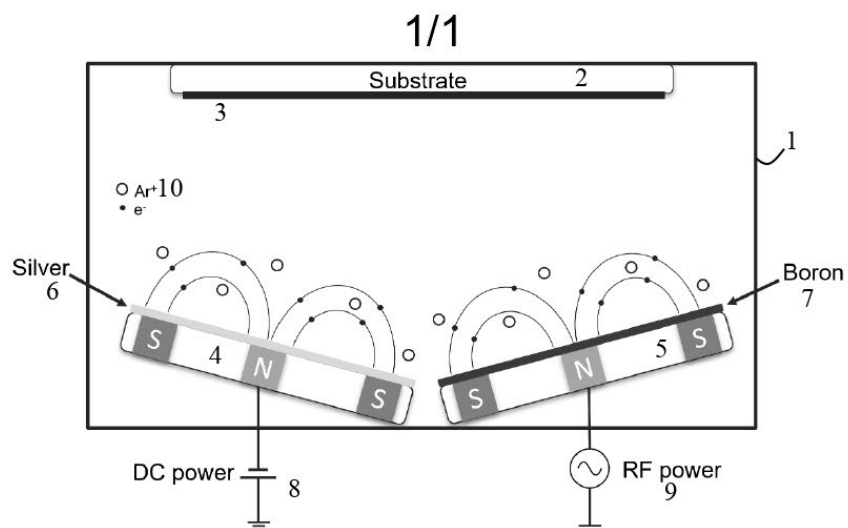


Figure 1: Schematic illustration of the deposition procedure used to synthesize the single crystal silver films.

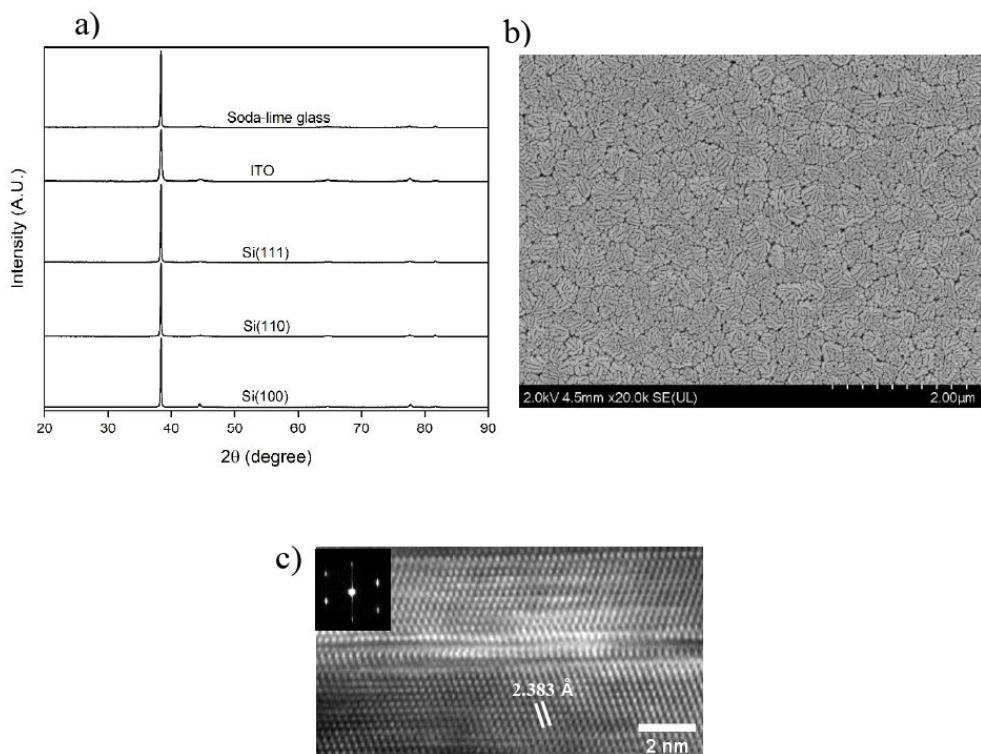


Figure 2: a) XRD spectra of the single crystal films deposited on various substrate. b) SEM image of the film deposited on soda-lime glass. c) TEM image showing a twin boundary with FFT of one side of the boundary

**Enhanced Electrochemical CO₂ Reduction through
Nanostructuring and Light Element Modification**

Kim Robert Gustavsen

**Doctoral dissertations at the
University of South-Eastern
Norway no. 184**

ISBN 978-82-7206-834-8 (print)
ISBN 978-82-7206-835-5 (online)

usn.no